Innovative Fiber-based Interferometers for Optical Signal Processing in Next-generation Communication Networks

DU, Jiangbing

A Thesis Submitted in Partial Fulfillment
of the Requirements for the Degree of
Doctor of Philosophy
in
Electronic Engineering

The Chinese University of Hong Kong
August 2011

ProQuest LLC.
789 East Eisenhower Parkway
P.O. Box 1346
Ann Arbor, MI 48106 - 1346

ABSTRACT OF THESIS ENTITLED:

Innovative Fiber-based Interferometers for Optical Signal Processing in Next-generation Communication Networks

Submitted by DU Jiangbing

For the degree of Doctor of Philosophy in Electronic Engineering

at The Chinese University of Hong Kong in August 2011

The continuously growing Internet traffic has resulted in a huge amount of data flow in the optical networks, particularly along with the recent developments of 3G/4G service, cloud computing, and Internet of things. High-data-rate optical transmission and interconnection are highly desirable in the near future, for next generation communication networks. Accompanied with the traffic growth is the requirement for faster signal processing technology. In this regard, all-optical processing plays a key role in eliminating optical-electrical-optical conversion, thus offering unmatched operation speed with reduced complexity and power consumption. This thesis focuses on high speed all-optical signal processing technologies based on innovative fiber-based interferometers, including Mach-Zehnder and loop mirror interferometers constructed by photonic crystal fiber (PCF), birefringent fiber and highly nonlinear fiber (HNLF).

Photonic crystal fiber based Mach-Zehnder interferometer (PCF-MZI) is constructed by a single line PCF, which is an in-line, all-fiber and coupler free device. As a delay interferometer (DI), PCF-MZI offers enhanced thermal stability in its operation. To date, applications of the in-fiber PCF-MZI are mainly focused on optical sensing instead of communications, which is a major objective in this thesis work. We have fabricated PCF-MZIs with different PCF lengths to introduce

desirable delays for optical signal processing, including differential phase shift keying (DPSK) demodulation, pulse format conversion, repetition rate multiplication and high speed optical time-division-multiplexing (OTDM) signal generation.

Orthogonol frequency division multiplexing (OFDM) has attracted quite a lot of interests due to its incomparable advantages in high spectral efficiency optical communication, which significantly enlarges the optical transmission capacity. Optical demultiplexing (DEMUX) of OFDM signals requires FFT processing, which can be efficiently achieved by using cascaded delay interferometers. We theoretically and experimentally studied the transmission properties of cascaded and multi-section Sagnac interferometers and demonstrated their application for the optical OFDM DEMUX. 4-channel OFDM DEMUX is experimentally demonstrated with open eye obtained.

Optical time-division-multiplexing is another promising solution for high-speed signal generation. Using the in-fiber PCF-MZI, we have also performed OTDM signal generation at different bit rates. The setup offers comparable performance to commercial multiplexers. We generated 160-Gb/s and 320-Gb/s OTDM signals based on PCF-MZIs.

Our study on optical processing of high speed OTDM signals continues with fiber-based techniques using third order nonlinear effects. Based on HNLF, we can construct active fiber interferometer, namely here as nonlinear optical loop mirrors (NOLM). We investigate dispersion asymmetric nonlinear optical loop mirror (DA-NOLM) based on cross phase modulation for simultaneous two-channel demultiplexing (DEMUX) using only a single baseband control pulse. Reconfigurable DEMUX has been achieved for 40-Gb/s OTDM signals. The

DEMUX are also switchable between two-channel and single-channel operations. Utilizing the tunable delay, DA-NOLM has also been applied to signal processing including pulse format conversions, and repetition rate multiplication.

With dispersion management inside the loop mirror interferometer, we have further proposed and demonstrated a modified DA-NOLM. The new device introduces a larger asymmetry in the propagation of the two interfering branches while maintaining a zero total dispersion in each of them. Consequently, pulse broadening is reduced and higher bit rate operation is supported. With the device, we have successfully achieved error-free two-channel DEMUX for 80-Gb/s OTDM signals.

We also investigated signal processing using nonlinear devices beyond those fiber interferometers. FWM is utilized for chirp magnification which was successfully applied to optical comb generation for obtaining optical OFDM signals. Optical comb generation with extinction ratio enhancement and flatness improvement is demonstrated utilizing a stimulated Brillouin scattering (SBS) based optical loop mirror. Clock recovery of OTDM-OOK signals has been successfully demonstrated over a wide range of bit rates using the SBS loop mirror.

摘要

近年來，伴隨著壹些諸如 3G/4G、雲計算和物聯網等新技術的發展，網絡帶寬持續高速增長，光網絡的數據流量也隨之不斷升高，高速的光傳輸和數據連接以及相應的高速信號處理在下壹代光通信系統中越發顯得重要。其中，全光信號處理以其超快的處理速度、較小的操作難度和能量消耗，受到了極大關注。本論文將致力於服務於下壹代光通信系統的全光纖高速信號處理的研究，特別是基於新型光纖幹涉儀的全光信號處理。

基於光子晶體光纖的馬赫曾德爾幹涉儀(PCF-MZI)是壹種緊湊穩定的光纖幹涉儀器件，其原理是基於纖心模式和包層模式的幹涉，本質上來說是壹種延遲幹涉儀，利用不同的光子晶體光纖長度可以得到不同 FSR 的延遲幹涉，從而應用於各種光信號處理中。我們自制了不同長度的 PCF-MZI，成功用於差分相位鍵控(DPSK)信號的解調，脈沖格式轉換，脈沖重複頻率的倍增以及高速時分複用信號(OTDM)的產生。

正交頻分複用(OFDM)的超高光譜效率特性有利於進壹步增加通信容量，對於 OFDM 光信號的接受，解複用是壹個不可缺少的過程，比如利用全光器件的光學解複用。其中，作爲級聯的和多段的 Sagnac 幹涉儀就可以用於 OFDM 的全光解調，在理論和實驗分析的基礎上，我們得到了四載波的 OFDM 全光解複用。

非線性光纖環鏡是區別於被動光纖幹涉儀的另壹類主動的和非線性的光纖幹涉儀，在高速全光信號處理中有許多應用。其中，色散不對稱的非線性光纖環鏡(DA-NOLM)利用了光纖環鏡中的不對稱的色散分布，從而產生不同的飛非線性過程。基於 DA-NOLM 以及其改進版的 MDA-NOLM，特別是

其延遲可調的特性，我們實現了諸多光信號處理應用，其中包括可配置的雙通道 OTDM 解複用和插分複用，脈沖重複頻率倍增以及脈沖格式轉換。

另外，基於非線性光纖中的四波混頻(FWM)，我們研究了全光的啁啾放大，並將該效應成功應用於光梳狀譜的產生，得到了多載波的 OFDM 光信號。而且，利用受激布裏淵散射(SBS)，我們還實現了對光梳狀譜的消光比的明顯提高，梳狀譜載波的平坦度也有提高。基於 SBS 效應，我們研究了全光的時鍾信號提取，成功實現了對 OTDM 信號的高速全光時鍾恢複。

Acknowledgements

I want to take this opportunity to thank everyone that has been helping me during my PhD study in the Chinese University of Hong Kong.

I want to express my deepest gratitude to my supervisor, Prof. Chester Shu, for his support and guidance in my study and research, the care and help in my work and living. It is my wisest decision to join Prof. Shu's group. He has been enlightening everywhere with his experience, knowledge, skills, patience, encouragement and professional insights, which are the most invaluable legacies to me for my PhD study.

I would like to thank Prof. K.T. Chan and Prof. H.K. Tsang, for their support and the running of the laboratory with well-equipped facility and harmonic atmosphere, which makes everything comfortable and smooth. I want to thank Ms. L.S. Ho. Our research would achieve nothing without her help and support.

I want express my gratitude to DAI Yongheng, Gordon K.P. LEI, WANG Liang, FU Xuelei, Alan CHENG, Mable FOK, GAO Ying, ZHOU Bin, and all the other members once worked in SHB318.

My special thanks are reserved for my dear friends, HE Hao, ZHANG Zhongxiang, CHEN Mengyu, YANG Tao, LI Baopu, FAN Yichen, CHEN Kejian, SUN Caiming, LIU Jingjing, MA Zili, CHEN Xia, XU Lin, Chris WANG, Christy FUNG, CHENG Zhengzhou, XU Ke, CHEN Yimin, GUO Jianping, QI Lin, CHEN Dongmei, ZHAO Qian, QIU Yang, XU Jing, ZHANG Yang, DU Xiaona, and everyone that once shook hands with me, online chatted with me, discussed optics and girls with me, talked dirty jokes to me, and played basketball with me. The 3-year living in Hong Kong is memorable and joyful because of your companion, to

Franklin for dinner; to Shenzhen for Karaoke; to somewhere for drinking, for barbeque, for sunshine, for swimming, for playing basketball, for bicycling and for getting older; and of course, to the destiny for a pleasant graduation. The messing up, the jokes, the laughing, the despising to the food, and the fantasies of beautiful things are full filled with joy and wisdom, and that was fun!

I want to thank my family. It has been a long time since I left them for college study from Sichuan to Tianjin, and then to Hong Kong. Things have been changing, but their love and support never change.

Lastly, I wish every beloved ones, live long and prosper.

Table of Content

List of Tables and Figures

List of Abbreviations

AWG	arbitrary waveform generator/arryed waveguide grating
BER	bit error rate
BF-SI	birefringent fiber based Sagnac interferometer
CR	clock recovery
DAC	digital to analog conversion
DEMUX	demultiplexing
DQPSK	differential quadrature phase shit keying
DSP	digital signal processing
EDFA	erbium-doped fiber amplifier
EOM	electro-optic modulator
ER	extinction ratio
ERGO	mode-locked Er:Yb:glass oscillator
FFT	fast Fourier transform
FTTH	fiber-to-the-home
FWM	four wave mixing
HNLF	highly nonlinear optical fibers
IFFT	inverse fast Fourier transform
MLLD	mode-locked laser diode
MZI	Mach-Zehnder interferometer
NOLM	nonlinear optical loop mirrors
NPR	nonlinear polarization rotation
OFDM	orthogonal frequency division multiplexing
OOK	on off keying
OPA	optical parametric amplification
OTDM	optical time division multiplexing
PCF	photonic crystal fiber
PCF-MZI	Photonic crystal fiber based Mach-Zehnder interferometer
PPLN	periodically poled lithium niobate
QAM	quadrature amplitude modulation
SBS	stimulated Brillouin scattering
SMF	single mode fiber
SNR	signal to noise ratio
SOA	semiconductor optical amplifiers
SPM	self phase modulation
WDM	wavelength division multiplexing
XPM	cross phase modulation

Chapter 1: Introduction

Telecommunication is the foundation of the information technology industry that has been drawing huge investment interests, which has been highlighted in Obama's first State of the Union Address speech for United States and also in the twelfth five-year-plan outline for national economic and social development of the People's Republic of China [1, 2]. For example, in the twelfth five-year-plan for China, the next generation information technology industry is exclusively mentioned as one of the seven strategic new industries. Included in the twelfth five-year-plan are the developments for advanced wideband networks, convergence of the three networks, applications of interconnecting of things and cloud computing, which are also emphasized in the Prime Minister Wen Jiabao's government report 2011. Accompanied with those attentions is the rapidly growing data traffic demand for telecommunications, including mainly the next-generation optical communication.

For next-generation optical communications, the main issue is to increase the bandwidth for the urgent demand of more data traffic [3-5]. China-Telecom, as the biggest fixed-network communication company in China, is trying to invest more than 150-billion RMB in the project of "optical networking city" within the next five years starting from 2011. The project will focus more on high-speed optical transmission for the backbone-network and wideband optical access for fiber-to-the-home (FTTH), which enables us to network the main cities by optical fibers and so called "optical networking city". The aim is to significantly increase the access bandwidth up to 10 times but continue to reduce the cost for customers. Shown in Fig. 1.1 is the Internet speed and costs around the world [6].

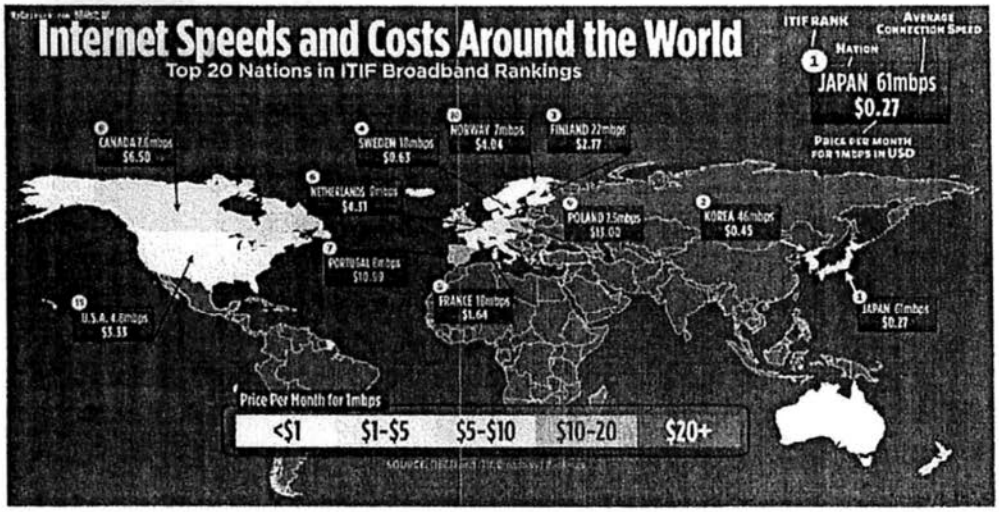

Fig. 1.1 The Internet speed and costs around the world by Organization for Economic Co-operation and Development (OECD) [6]

1.1 Introduction to Next-Generation Optical Communications

The history of optical communication can trace back to 1970s, right after the mature fabrication of low-loss optical fiber and the invention of laser. The first generation of optical communication was launched in late 1970s, when the transmitters, receivers and optical fibers were operated around 800-nm wavelength. At that time, 45 Mb/s data rate is allowed to transmit with 10-km repeater spacing [7].

With the operation wavelength moved to 1300-nm region, where the fiber loss is below 1 dB/km, the second generation optical communication systems with data rate up to 1.7 Gb/s and repeater spacing of 50 km, were commercially available, by the late 1980s [7].

The third generation optical communication systems operate at 1550-nm region, where the fiber loss was only 0.2 dB/km based on the fabrication technology in 1980s. However, due to the fiber dispersion at 1550-nm region, the launch of 1550-nm lasers for transmission was delayed [8]. Until 1990, 2.5 Gb/s optical

communication systems are commercially available with the capability of 10Gb/s operation, which is so called the third generation optical communication. At that time, the signal was regenerated periodically by using electrical repeaters spaced by 60-70 km, which had been significantly enlarged compared to the older generation systems [8]. Coherent detection, which was able to significantly increase receiver sensitivity, caught a lot of interest at that time.

The applications of fiber amplifiers and wavelength division multiplexing (WDM) are the core issues in the fourth generation of optical communication systems. The advent of WDM around 1992 started a revolution of the optical communication with the system capacity doubled every six months. 10-Tb/s system capacity was achieved by 2001. In one record experiment in 2005, 300 wavelengths were transmitted over 7380 km with a bandwidth-length (BL) product of 25,000 Tb/s-km. Commercial systems with 3.2 Tb/s capacity, 40 Gb/s for 80 wavelengths, together with the use of Raman amplification, were available by the end of 2003 [7, 8].

By examining the evolution history of optical communications in the last forty years, we can find that the data rate per wavelength has been increasing from tens of Mb/s to over 400 Gb/s for industry, along with the improvement of optical fiber fabrication, semiconductor and optoelectronics developments, and the use of advanced modulation formats and multiplexing technologies. Today, the rapidly growing data traffic leads to the demand in higher speed optical transmission and faster optical access, which are the main topics for next-generation, the fifth-generation optical communication networks [8].

Fiber-optics is the foundation of optical communication. Nowadays, the fabrication of high quality optical fiber is very mature. The loss can be maintained

at a very low level beneath 0.2-dB/km. This low loss transmission is the key feature of optical fiber, which is quoted as one thing that is impossible to be replaced within one hundred years, by Charles Kao (the 2009 Nobel Prize winner). Recently, researchers are looking into photonic crystal fiber (PCF) and plastic fiber for next-generation optical communications. For example, low-loss and large-mode-area single mode photonic crystal fibers (PCFs) have been demonstrated for high-speed WDM transmission [9].

In laboratory, there are demonstrations of high data rate over Tb/s utilizing multiplexing technologies such as wavelength division multiplexing (WDM), optical time division multiplexing (OTDM) and orthogonal frequency division multiplexing (OFDM) [10]. Presently, WDM is the major technology at hand that is capable to meet the high bandwidth in optical networking for next-generation optical communication. The single carrier speed is under the evolution from 10 Gb/s for present backbone and metro network to 40 Gb/s and 100 Gb/s for next-generation networks [11]. Now, the aim is 400 Gb/s.

To achieve such a high speed modulation data rate up to 100 Gb/s or 400 Gb/s over a single wavelength (channel), advanced modulation formats is needed. Among those are differential quadrature phase shit keying (DQPSK) and quadrature amplitude modulation (QAM), which are drawing a lot of interest for long haul transmission and metro networking. Dual polarization QPSK (DP-QPSK) has been chosen as the modulation format for 100 Gb/s system [11, 12].

The Optical Internetworking Forum (OIF), launched in 1998 as a non-profit organization, has been doing a lot of work for the standardization of 40Gb/s-100Gb/s architecture and framework [12]. It started in 2007 when the first rumors surfaced that the IEEE would be working on a 100-Gb/s project. Now, the progress

of 100-Gb/s has come to the commercial implementation period and telecommunication service providers are beginning to install the system or upgrade from the 40-Gb/s system to 100-Gb/s. In March 2011, the first 100-Gb/s long haul backbone network was successfully launched in Europe between Paris and Frankfurt by Verizon, an American telecommunication service provider [13, 14]. Telecoms like Huawei, Alcatel-Lucent and NSN have all announced their 100-Gb/s solutions. However, for 400-Gb/s system, the standardization of the architecture and networking is still under progress.

1.2 Overview of Optical Signal Processing

Signal processing is embodied in optical communication as a key role covering the whole system from transmitter to receiver, which appears to have growing importance along with the speeding up of the data rate to 40 Gb/s and 100 Gb/s. Currently, in optical communication systems, signal processing is performed mostly in the electric domain which usually needs optical-electrical-optical (OEO) conversions. This is acceptable when it is done at the ends (the transmitter or receivers) but becomes a burden of the system when it is done at the nodes. The limited speed of OEO conversion is also a bottleneck for all-optical networks in next-generation optical communications. Therefore, optical signal processing, which has ultrafast processing speed, will play a key role in building up the all-optical networks and improving system performance of optical communications.

Optical signal processing is particularly important for making the system more flexible and robust for high-speed and all-optical networks. Advanced optical systems need various kinds of signal processing at the nodes or the ends, such as wavelength conversion, optical regeneration, optical multiplexing and

demultiplexing, wavelength multicasting, optical demodulation, optical logic gating and so on [15]. Generally, the processing can be classified into passive optical signal processing and active optical signal processing, based on how the scheme functions. Passive optical signal processing is based on passive devices with various functions in optical systems, typically in passive optical networks (PON). Active optical signal processing usually has better reconfigurability and tunability compared to passive optical signal processing.

Usually, passive and active optical signal processing techniques are targeted in different areas and they are quite separated with each other. Passive devices are usually more preferred due to speed limitless operation and very little power consumption. Meanwhile, some functions that are usually processed by passive devices can also be achieved actively. As an example, DPSK signals can be demodulated by delay interferometers and also by nonlinear optical loop mirrors that offer key advantages to improve the system performance.

Due to the ultrafast response speed, the present active optical signal processing techniques are mostly focused on optical nonlinear effects in highly nonlinear optical fibers (HNLF), semiconductor optical amplifiers (SOA), nonlinear crystals like periodically poled lithium niobate (PPLN) and so on. Compared with HNLF, SOA and PPLN have better compactness. However, HNLF, especially specialty HNLFs such as PCF and bismuth fiber, also catches much interest due to their ultrahigh nonlinearity, tailorable dispersion, all-fiber operation and so on.

1.3 Interferometers in Optical Communications

Among different optical signal processing devices, interferometers are particularly important and they have been in use in a lot of systems configured as filter,

modulator, demodulator, multiplexer, demultiplexer, regenerator, format converter and so on. In optical sensing, interferometers are also very much useful. One of the most notable examples of interferometer is the gyroscope for navigation, which is actually one kind of angular velocity sensing. In this section, we will have a brief overview of widely used interferometer devices in optical communications.

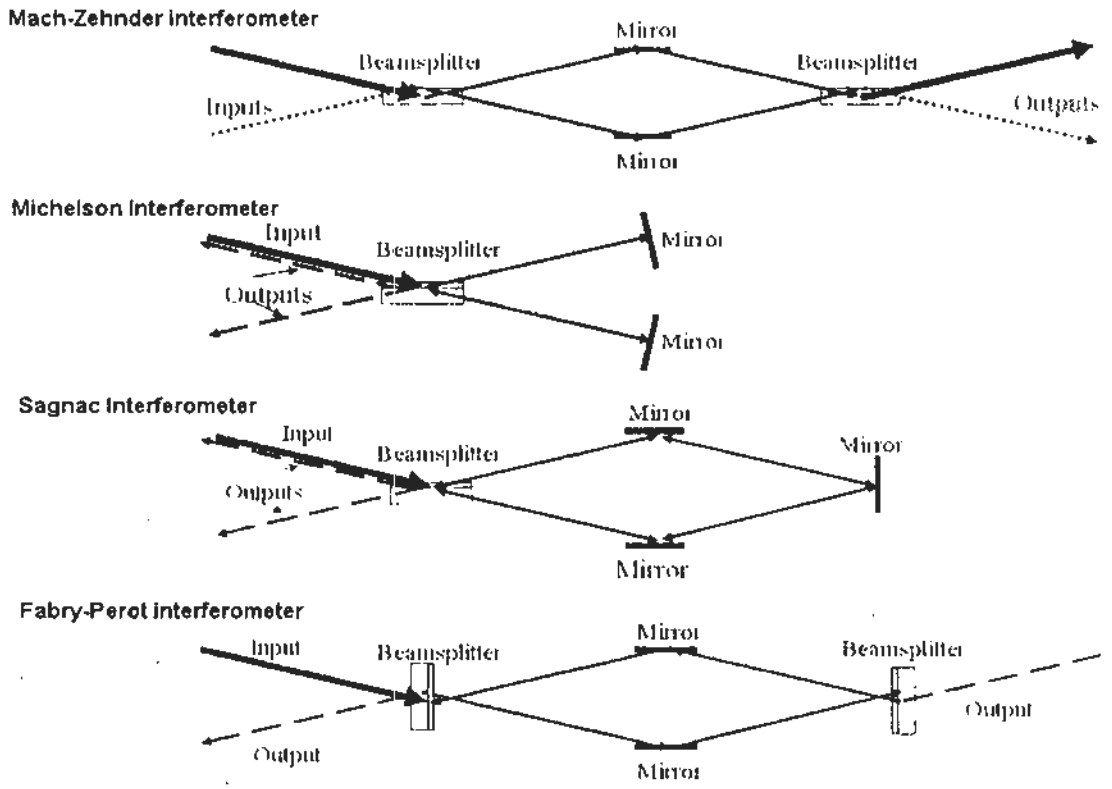

Fig. 1.2 Principle of the interferometers.

Fig. 1.2 shows the schematic illustrations of the four leading kinds of interferometers: Mach-Zehnder interferometer, Michelson interferometer, Sagnac interferometer, and Fabry-Perot interferometer.

Among those interferometers, Mach-Zehnder interferometer (MZI) has the simplest structure but the widest application. For example, the widely using Mach-Zehnder modulators are all constructed based on Mach-Zehnder configuration. The up-coming 100-Gb/s DP-DQPSK modulator is based on a dual parallel Mach-

Zehnder structure. The DPSK demodulators, fabricated by optical fibers or silicon waveguides, are also constructed based on MZI. Some other examples of MZI devices include wavelength interleavers, demultiplexer, pulse format converters and so on. One should notice that Mach-Zehnder modulators are actually active interferometers which are driven by electrical signals. The operation differs from passive interferometers such as DPSK demodulators.

Sagnac interferometer can be taken as a variant of Mach-Zehnder interferometer, which has the two arms replaced by the clockwise and counter clockwise operations. Michelson interferometer's application area is more likely in sensing, such as measurement and monitoring, rather than in communication. Fabry-Perot interferometer has been widely used both in optical communication and optical sensing. For example, lasers, particularly high power solid state lasers, are often based on Fabry-Perot structures.

Optical fiber based interferometers are particularly interesting due to their all-fiber structure, which has advantageous interface for compatible fiber interconnection in optical fiber systems. Fiber based interferometers also have the well performed compactness, stability and robustness. There have been demonstrations of realizations of interferometers based on optical fibers, including fiber coupler based Mach-Zehnder interferometer, birefringent fiber based Sagnac interferometer, in fiber micro-cavity as Fabry-Perot interferometer, and fiber grating based in-line Mach-Zehnder interferometer.

Usually, fiber interferometers are identified as passive devices. There are also many nonlinear optical signal processing devices constructed based on optical loop mirrors (NOLM), which can be considered as active interferometers. Generally, the optical switching of NOLMs is due to control of the interference between

clockwise branch and counter clockwise branch light waves. The optical control introduces an optical modulation and thus enables the relevant processing functions. Examples of optical signal processing in those active interferometers include all optical regeneration, pulse compression, clock recovery and DPSK demodulation.

One can notice that the signal processing applications originated from interferometers cover quite a large area in optical communications, especially from a comprehensive viewpoint including innovative devices like NOLMs as active and nonlinear interferometers. A systematic overview with focused study of recent innovative fiber interferometers will be desirable and useful to researchers in the field, which is going to be explored in this thesis.

1.4 Organization of the Thesis

Recently, along with the extended use of advanced modulation formats and multiplexing techniques in optical transmission and access, there are increasing interest in optical processing in which interferometers are playing an important role. This thesis focuses on a series of innovative fiber devices with emphasis on fiber interferometers for optical signal processing in next-generation optical communications.

The introduction of next-generation optical communications with a review of optical communication history, overviews of optical signal processing and interferometers for optical communications has been discussed in Chapter 1.

In Chapter 2, we describe the fabrication of photonic crystal fiber based Mach-Zehnder interferometers (PCF-MZIs). Their applications in optical signal processing are experimentally studied. Included are DPSK demodulation, pulse

format conversion, repetition rate multiplication as well as high speed OTDM signal generation.

OFDM is an attractive solution in next-generation communications for long haul transmission and optical access. Cascaded delay interferometers can be used in optical OFDM demultiplexing, which has been introduced in Chapter 3. Cascaded and multisection Sagnac interferometers are studied theoretically and experimentally in this chapter. Designs of optical OFDM demultiplexers are demonstrated based on cascaded and multisection Sagnac interferometers. Optical demultiplexing of OFDM signals has been experimentally investigated.

Optical nonlinearities have been utilized for all-optical signal processing offering advanced performances. In Chapter 4, we first introduces the nonlinear effects in optical fibers, including self-phase modulation, cross phase modulation, four wave mixing, and optical parametric amplification. Nonlinear optical loop mirrors (NOLM) as active and nonlinear interferometers are also introduced in this chapter.

Dispersion asymmetric NOLM, as a variant of NOLM, is investigated in Chapter 4. Reconfigurable OTDM demultiplexing is demonstrated based on the DA-NOLM. Two-channel optical DEMUX using a single baseband control pulse train is achieved for 40-Gb/s OTDM signals. A modified configuration of DA-MOLM is presented with dispersion management inside the loop mirror. Reconfigurable two-channel DEMUX of 80-Gb/s OTDM signals is demonstrated. Other applications of DA-NOLM for repetition rate multiplication and pulse format conversions are also discussed.

In Chapter 5, optical comb generation and clock recovery are studied based on nonlinear signal processing techniques. Degenerate four wave mixing (FWM) is

utilized for chirp magnification to generate an optical comb with improved number of sub-carriers. Based on stimulated Brillouin scattering (SBS) loop mirror, we demonstrate the generation of improved optical combs with enhanced extinction ratio and flatness. Bit-rate variable optical clock recovery of OTDM signals is experimentally studied.

Chapter 6 presents a summary of the thesis along with suggestions for the future work. The understanding and proposal of several cutting edge techniques in the area of high speed optical communications are discussed.

References

[1]. Barack Obama, State of the Union Address speech 2010, January 27, (2010) http://photos.state.gov/libraries/ukraine/164171/pdf/state_union10.pdf

[2]. The twelfth five-year-plan outline for national economic and social development of the People's Republic of China http://www.gov.cn/2011lh/content_1825838.htm

[3]. A. A. M. Saleh, "Transparent optical networking in backbone networks", in Proc. OFC, Baltimore, MD, ThD7 , pp. 62-64, Mar. 7-10 (2000)

[4]. Adel A. M. Saleh and Jane M. Simmons, "Evolution Toward the Next-Generation Core Optical Network," J. Lightwave Technol. 24, 3303 (2006)

[5]. V. Shukla, D. A. Brown, C. J. Hunt, T. Mueller, and E. Varma, " Next Generation Optical Network: Enabling Dynamic Bandwidth Services," in National Fiber Optic Engineers Conference, OSA Technical Digest Series (CD) (Optical Society of America, 2007), paper.NWB3 (2007)

[6]. "The Internet speed and costs around the world" by Organisation for Economic Co-operation and Development (OECD) http://www.oecd.org/document/54/0,3746,en_2649_33703_38690102_1_1_1_1,00.html

[7]. G. Keiser, "Optical Fiber Communications" (McGraw-Hill, 2000).

[8]. G. P. Agrawal, "Fiber-Optic Communication Systems", Furth edition (Wiley)

[9]. E. Tangdiongga, H. Yang, J. Lee, C. Okonkwo, H. van den Boom, S. Randel, and T. Koonen, "Low-Cost and High-Capacity Short-Range Optical Interconnects Using Graded-Index Plastic Optical Fiber," in Optical Fiber Communication Conference, OSA Technical Digest (CD) (Optical Society of America, 2010), paper JWA64 (2010)

[10]. R. Freund, M. Nolle, C. Schmidt-Langhorst, R. Ludwig, C. Schubert, G. Bosco, A. Carena, P. Poggiolini, L. Oxenlowe, M. Galili, H. C. Hansen Mulvad, M. Winter, D. Hillerkuss, R. Schmogrow, W. Freude, J. Leuthold, A. D. Ellis, F. C. Garcia Gunning, J. Zhao, P. Frascella, S. K. Ibrahim, and N. Mac Suibhne, "Single-and multi-carrier techniques to build up Tb/s per channel transmission systems," in International Conference on Transparent Optical Networks (ICTON) (2010), Tu.D1.4.

[11]. P. J. Winzer, "Beyond 100G ethernet," IEEE Commun. Mag. 48, 26-30 (2010)

[12]. Joe Berthold, "Progress and Challenges for 100 GbE," http://www.oiforum.com/

[13]. E. Bert Basch, "Deployment of High Capacity Transport Networks within Verizon," 15th OptoElectronics and Communications Conference (OECC2010) Technical Digest, July 2010, Sapporo Convention Center, Japan, paper. 9B4-1 (2010)

[14]. Glenn Wellbrock, "Preparing For the Future," 36th European Conference and Exhibition on Optical Communication (ECOC), Torino Italy, (2010)

[15]. K. E Stubkjaer, "Technologies for Optical Processing," in Tech. Dig. OFC/NFOEC, San Diego, CA, 2008, Invited tutorial OMV1 (2008)

Chapter 2: Optical Signal Processing based on PCF-MZI

Photonic crystal fibers (PCF) have been widely studied with increasing interest because of their wide range of improved optical properties and the ability of flexibly manipulating these properties [1]. Accordingly, many improved PCF devices have been demonstrated such as PCF gratings [2], PCF filters [3], and PCF couplers [4]. Based on their light guiding mechanism, PCF can be divided into index guiding PCF and bandgap guiding PCF [5, 6]. Presently, the leading PCF is index-guiding based on air-silica structure with air holes axially aligned in the fiber.

Interferometers built based on PCF have drawn a lot of interest among those PCF devices [7]. Variant of PCF interferometers have been introduced in Chapter 2, including Mach-Zehnder interferometer [8], Michelson interferometer [9], Sagnac interferometer [10], and Fabry-Perot interferometer [11-13]. Advanced properties such as in-line and compact structure, stable and tunable operation, all-fiber feature, and easy fabrication, can be obtain due to those unique characteristics of PCF.

Photonic crystal fibers based Mach-Zehnder interferometer (PCF-MZI) is constructed based on PCF, utilizing its core mode and cladding mode guidance for the interference [8, 14-20]. In this chapter, we investigate the in-line Mach-Zehnder interferometer which is constructed by PCF. The principle of the in-line PCF-MZI is discussed in Section 2.1. The fabrication of PCF-MZI is studied in Section 2.2, together with the experimental characterization of the fabricated PCF-MZIs. In Section 2.3, DPSK demodulation is demonstrated based on the PCF-MZI. The optical pulse format conversions including RZ-to-NRZ and NRZ-to-PRZ are

studied in Section 2.4. The repetition rate multiplication and high speed OTDM generation based on PCF-MZI are discussed in Section 2.5.

2.1 Photonic Crystal Fiber based Mach-Zehnder Interferometer

2.1.1 Operation Principle

Photonic crystal fiber based Mach-Zehnder interferometer (PCF-MZI) is known as an all-fiber in-line delay interferometer (DI), which has a relative delay introduced by the index difference between the core mode and the cladding mode of the PCF [8]. Due to the unique air-hole structure of PCF, the index difference between the core mode and the cladding mode can be quite large, which implies that a short PCF can be used to introduce a large delay while keeping optical attenuation of the cladding mode at a low level [21, 22]. The in-fiber PZF-MZI, as a DI with an in-line structure and enhanced thermal stability, has been demonstrated favorably in optical sensing [17-19, 23].

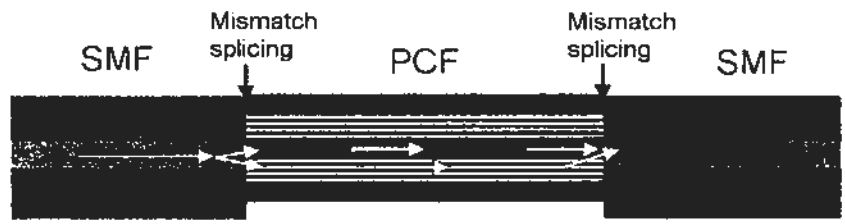

Fig. 2.1 Schematic illustration of the PCF-MZI principle in this work.

Fig. 2.1 shows the schematic illustration of a PCF-MZI, which is fabricated by mismatch splicing [8]. The mismatch between single-mode fiber (SMF) and PCF

allows the input light to be split into the core and the cladding of the PCF, resulting in light propagating as core mode and cladding mode, respectively. Therefore, we can take the core and the cladding as the two arms of a Mach-Zehnder interferometer. The core mode and cladding mode, which are characterized by different effective indices, n_{core} and $n_{cladding}$, have different light propagation speeds in the PCF. Consequently, a relative group delay is developed after the propagation. When the core-mode light and the cladding-mode light are recombined at the PCF output end that is mismatch-spliced with another SMF, interference will take place and result in a transmission spectrum described as follows [8, 14]:

$$T(\lambda) = I_{core}(\lambda) + I_{cladding}(\lambda) + 2\sqrt{I_{core}(\lambda) I_{cladding}(\lambda)}\cos(2\pi\Delta nL/\lambda) \qquad \text{(Eq.2.1)}$$

$$\Delta n = n_{core} - n_{cladding} = \frac{\lambda}{2\pi}(\beta_{core} - \beta_{cladding}) \qquad \text{(Eq.2.2)}$$

where β_{core} and $\beta_{cladding}$ are the propagation constants, and $I_{core}(\lambda)$ and $I_{cladding}(\lambda)$ are the light intensities of the core mode and the cladding mode at the PCF output, respectively. L is the physical length of the PCF and λ is the wavelength. The operation principle is based on Mach-Zehnder interference with the core and cladding modes taken as the two interference arms, as shown in Fig. 2.1. According to Eq.2.1, the transmission is periodic with respect to frequency and is usually represented by a comb-filtering spectrum. The spacing $\Delta\lambda$ between adjacent constructive peaks (destructive valleys) can be described as:

$$\Delta\lambda = \frac{\lambda^2}{(n_{core} - n_{cladding})L} = \frac{2\pi\lambda}{(\beta_{core} - \beta_{cladding})L} \qquad \text{(Eq.2.3)}$$

We define a delay coefficient D corresponding to the relative time delay between core mode and cladding mode in one-meter PCF. Thus, the relative delay Δt and the delay coefficient D are given by:

$$\Delta t = \frac{L}{c/n_{core}} - \frac{L}{c/n_{cladding}} = \frac{\lambda^2}{c\Delta\lambda}, \quad D = \frac{\Delta t}{L} = \frac{\Delta n}{c} = \frac{\lambda^2}{cL\Delta\lambda} \qquad \text{(Eq.2.4)}$$

Hence, the delay coefficient of the in-fiber PCF-MZI is solely determined by the effective index difference Δn between core-mode light and cladding-mode light, which is in turn governed by the splicing mismatch and the PCF structure.

2.1.2 Core mode and Cladding Modes in PCF

These unique features of PCF interferometers come from the fact that optical properties of the guided modes in the core can be easily manipulated by changing the air-hole structure in the cladding [24, 25]. While there has been significant attention has been paid to the study of core modes of PCFs, the importance of cladding modes should also be highly valued. Particularly for PCF-MZI which is based on core-mode cladding-mode coupling, the understanding of cladding mode is necessary [21]. The modal properties including the core mode and cladding mode in a PCF is going to be studied in this section.

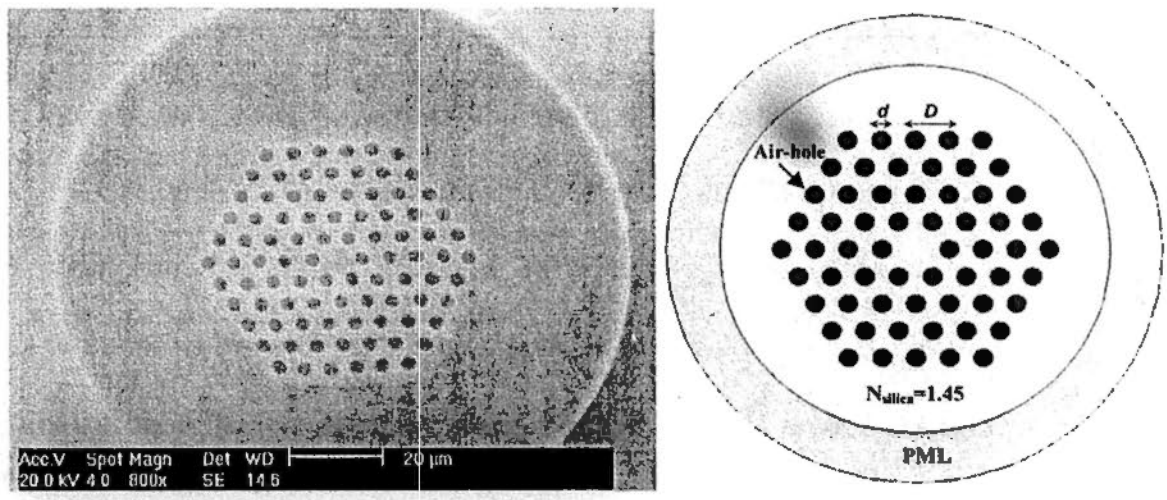

(a) (b)

Fig. 2.2 Sectional image of the PCF using in this work (a) and the calculation model with 4 rings of air holes in the cladding (b).

In this work, we are experimentally using a PCF with 5 rings of air holes in the cladding. The cross sectional structure of the PCF used in this work is depicted in Fig. 2.2(a). The pure silica PCF has a hole-to-hole spacing (adjacent hole-pitch) of D=5.8μm, a hole diameter of d=3.3μm in the cladding, and a ~7.8-μm core diameter. Due to the huge memory request of a 5-ring model, which is out of our computer calculation capability, we will use a 4-ring model instead as shown in Fig. 2.2(b). It can also give us reliable results of the cladding modes.

Fig. 2.2(b) shows the calculation structure of an index guiding PCF with 4 rings of air holes in the cladding. The background material is fused silica which has a refractive index of N_{silica}=1.45. The air holes are hexagonally distributed with a diameter of d and adjacent hole-pitch of D, 3.3 μm and 5.8 μm, respectively. The PCF is surrounded with a ring of perfectly matched layer (EML) for absorbing the leaked power and enables us to calculate the leak loss of the guiding modes [24]. By using means of full-vector finite element method (FEM, COMSOL [25]), Maxwell's equations could be solved and numerical calculations with complex propagation constants given as $M=\beta+i\alpha$ can be derived, [25] where β is the propagation constant and α is the attenuation constant. The leakage loss A with a decibel per meter scale has a relationship with α: $A = 20\times\log_{10}(e)\times\alpha = 8.686\times\alpha$.

Shown in Fig. 2.3 is the intensity profile of core mode LP01 at the wavelength of 1550 nm (the following mode profiles are all for 1550 nm). The well confined optical field in the silica core indicates a small confinement loss (2×10^{-7} dB/km). The arrows indicate the electric field directions. There is also another degenerated LP01 mode with orthogonal electric field directions with respect to the one in Fig. 2.3(a). So, the core mode LP01 includes the degenerated HE11 modes

with two orthogonal electric directions, the same as the conventional step index fibers. The effective modal index of core mode LP01 is calculated to be 1.44474.

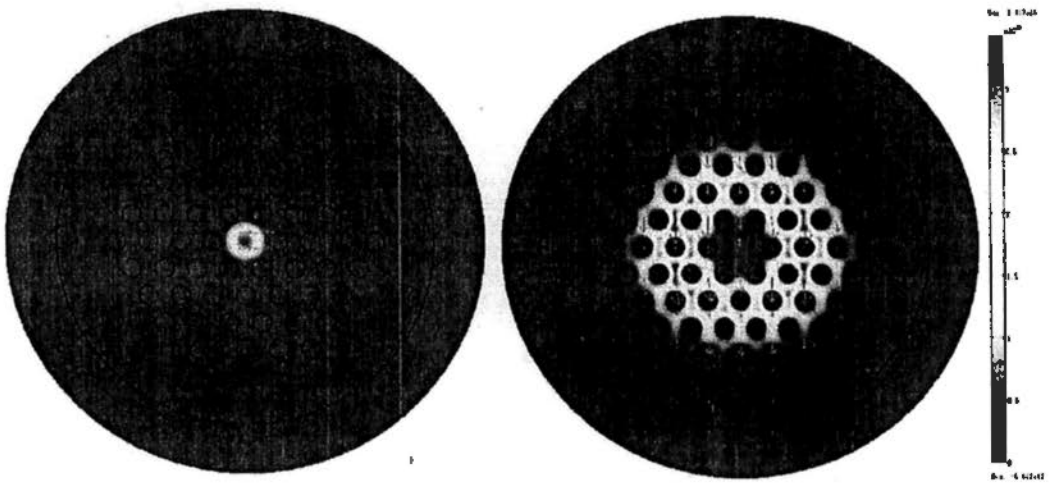

(a) (b)

Fig. 2.3 Mode intensity profiles of LP01 core mode and LP02 cladding mode.

Cladding modes LP02 is shown in Fig. 2.3(b), which correspond to two HE21 eigen modes in two polarization directions. The mode intensity profile is similar to the LP02 mode of the conventional step index fibers, only the most of the power e.g. 98.5% is within the cladding. LP11 modes are also calculated as the intensity profiles shown in Fig. 2.4, the TE01 mode, HE21-x mode, HE21-y mode and TM01 mode. It can be seen that most of the power of the cladding modes, including LP02 and LP11 modes, are well confined in the cladding, which results in the smaller effective modal indices as shown in Table 2.1.

The effective indices of cladding modes in Table 2.1 are around 1.434, which indicates a mode index difference of ~0.01, since the effective index of the core mode (the fundamental mode) is ~1.444. The simulation results correspond to a delay coefficient of ~33-ps/m according to Eq.2.4.

Table 2.1 Effective modal indices for LP02 and LP11 cladding modes

Cladding modes		n_{eff}
LP02	HE12-x	1.434462
	HE12-y	1.434461
LP11	TE01	1.434221
	HE21-x	1.434208
	HE21-y	1.434207
	TM01	1.434195

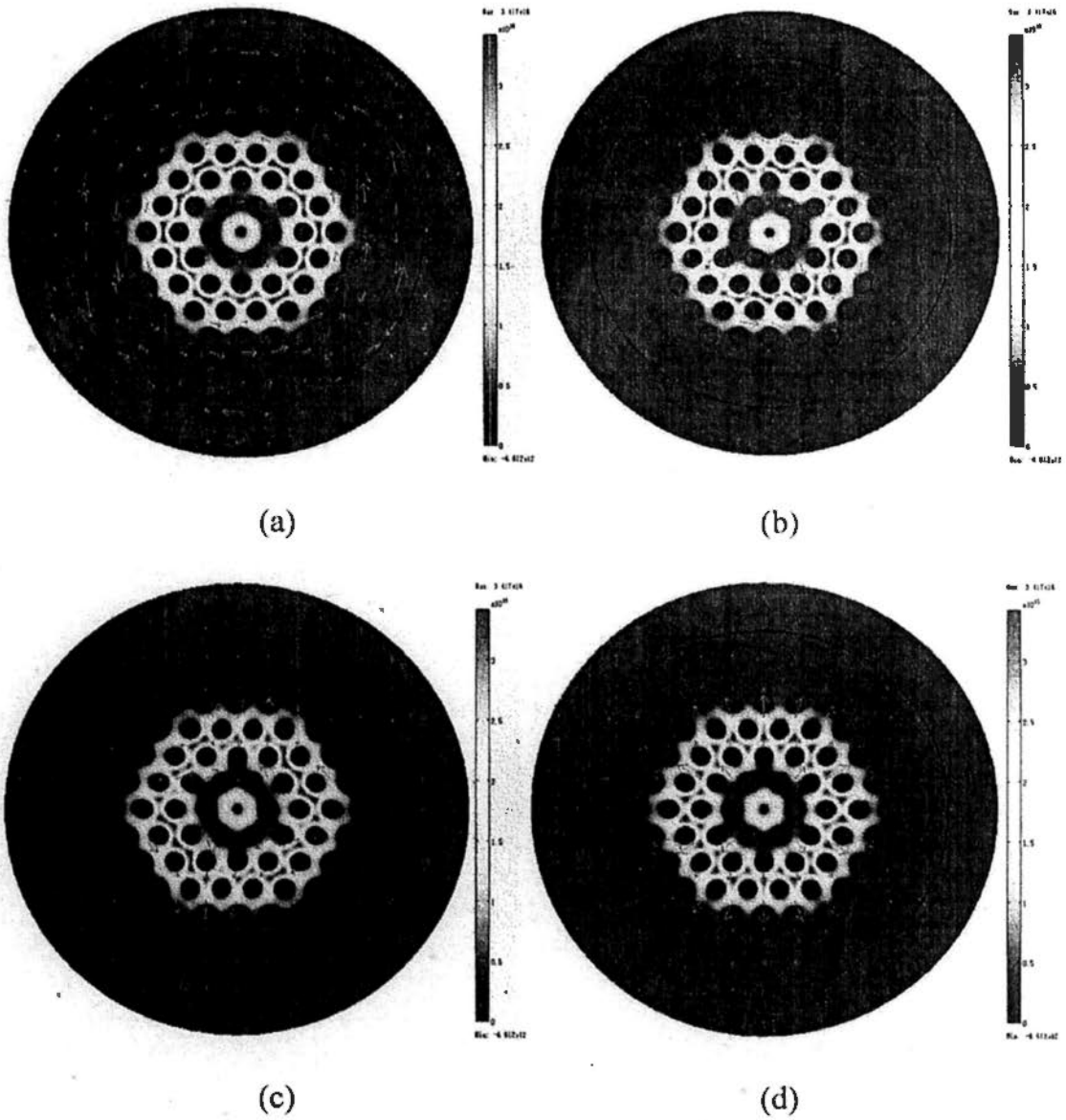

Fig. 2.4 Mode intensity profile of LP11 cladding modes: TE01 mode (a), HE21-x mode (b), HE21-y mode (c) and TM01 mode (d).

Higher order cladding modes are also supported by this PCF structure, such as LP21 and LP12 cladding modes. Since most the power will be coupled to the lower order cladding modes, which would be LP11 modes for the PCF we are using in this work [17], higher order cladding modes are not further investigated.

The leakage losses (confinement loss) for LP02 and LP11 modes are close to each other and it is calculated to be ~10 dB/km, which is much larger than that of the core mode (2×10^{-7} dB/km). It is difficult to utilize the cladding mode propagation for long distance transmission due to the large loss. However, in the study of PCF-MZI fabrication which usually needs only a short length of PCF like several meters, the loss contributed by the confinement of cladding mode is minimal.

2.2 PCF-MZI: Fabrication and Characterization

The fabrication of the PCF-MZI in this work is based on mismatch splicing between SMFs and PCF, which has been schematically illustrated in Fig. 2.1 [26]. In Fig. 2.5, the zoomed picture shows the splicing between SMF and PCF. The cladding diameters of SMF and PCF are both 125 μm. A small offset between SMF and PCF can be seen from the microscope picture in Fig. 2.5. The offset between the cores of SMF and PCF enables the power splitting and thus couples the input light into both the core mode and cladding mode in the PCF for propagation separately.

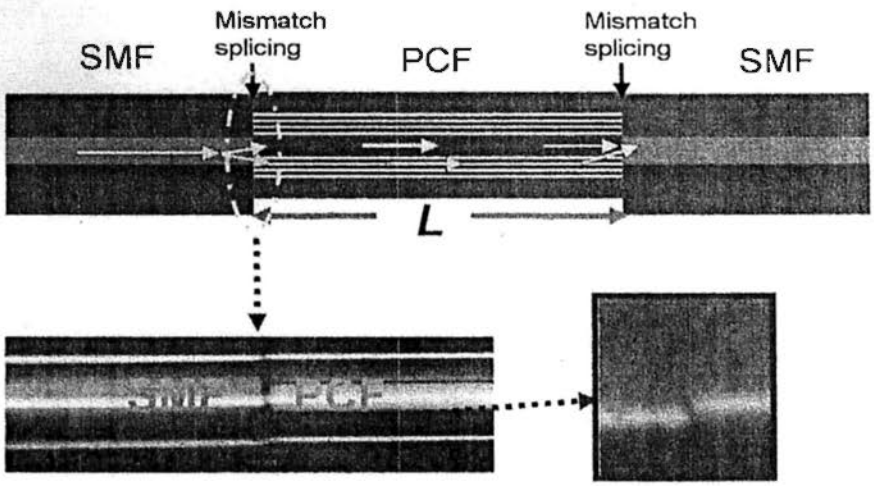

Fig. 2.5 Mismatch splicing between PCF and SMF for fabricating PCF-MZI.

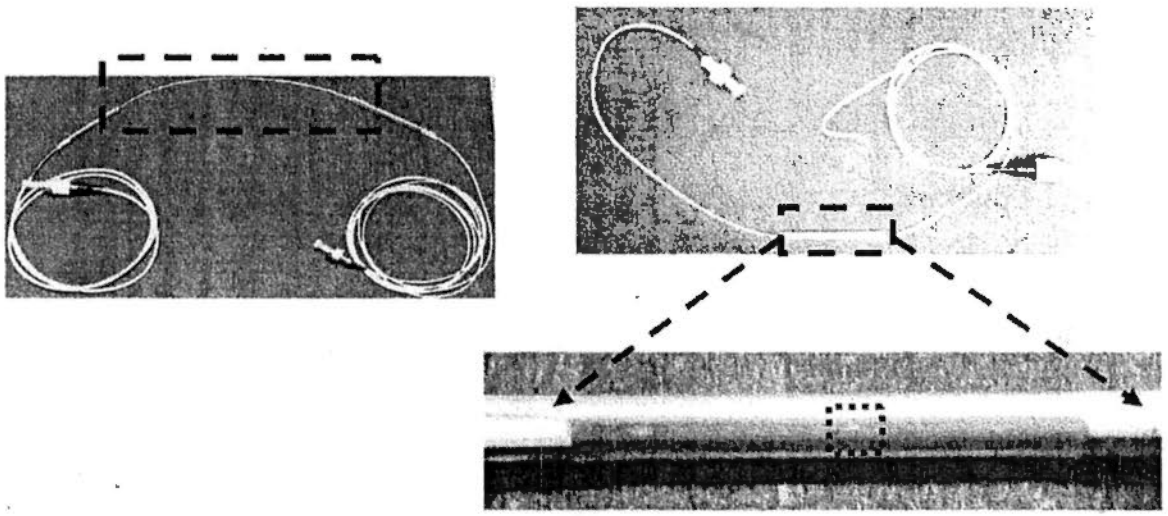

Fig. 2.6 PCF-MZIs with 20.4-cm PCF (left) and 1-mm PCF (right)

The pictures of two PCF-MZIs fabricated with 20.4-cm PCF and 1-mm PCF are shown in Fig. 2.6. The relative delay can be varied by changing the PCF fiber length, which makes the control of the delay more precise with respect to the conventional delay interferometers fabricated by using two couplers. One can even obtain a very small relative delay, such as ~0.03 ps by using 1-mm PCF as shown in Fig. 2.6. Therefore, it is possible to fabricate such a device with very short PCF and thus make it very compact.

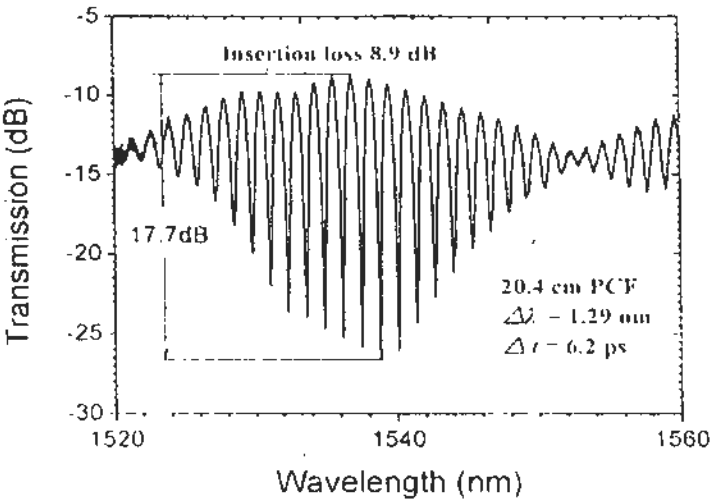

Fig. 2.7 Transmission spectrum for the PCF-MZI with 20.4-cm PCF

The transmission spectrum of a PCF-MZI is shown in Fig. 2.7. The plot shows a wavelength spacing $\Delta\lambda$ of 1.29 nm and a relative time delay Δt of 6.2 ps when the PCF length is 20.4 cm. The transmission spectrum is measured using an erbium-doped fiber amplifier (EDFA) as an amplified spontaneous emission (ASE) light source. From the experimental result, a delay coefficient of 30.4-ps/m is obtained which is quite close to the simulation result of ~33-ps/m. The value is consistent with the experimental results plotted in Fig. 2.8 showing about 50-ps and 25-ps relative delays (with 0.16-nm and 0.32-nm wavelength spacing) for two PCF-MZIs with 165-cm and 82.3-cm long PCFs, respectively. The delay coefficient of the in-fiber PCF-MZI is much larger than multimode fiber based MZI [27], birefringent fiber based loop mirror [28] and photonic bandgap fiber based delay interferometers [29], which have delay coefficients of 3.48 ps/m, 0.91 ps/m and 10 ps/m, respectively.

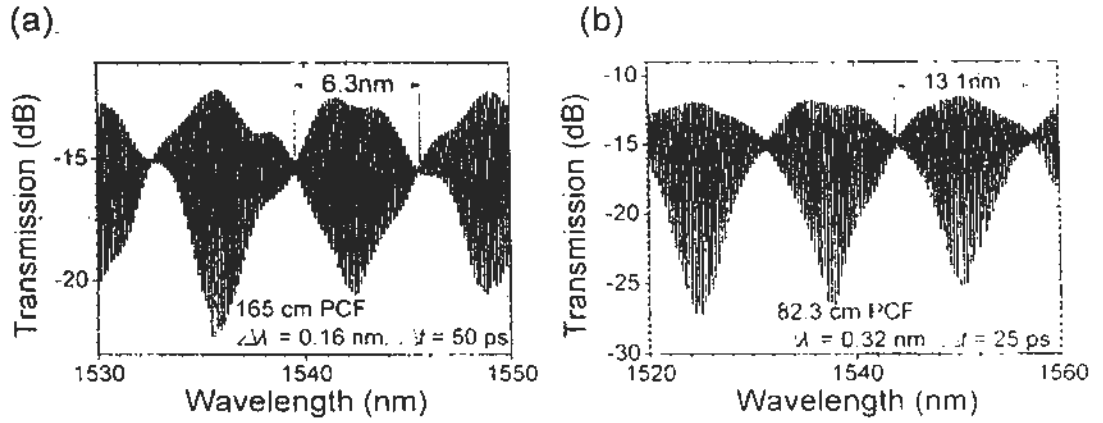

Fig. 2.8 Measured transmission spectra for PCF-MZIs with different PCF lengths: (a) 165.0 cm and (b) 82.3 cm.

The transmission spectra in Fig. 2.7 and Fig. 2.8 reveal the periodic nature on the variation of the interference extinction ratio. The extinction ratio $\eta(\lambda)$ is related to the power ratio of light ($\xi(\lambda)=I_{core}(\lambda)/I_{cladding}(\lambda)$) between the core mode and the cladding mode at the PCF output and is defined by

$$\eta(\lambda)=\left(\frac{1+\sqrt{\xi(\lambda)}}{1-\sqrt{\xi(\lambda)}}\right)^2 \qquad \text{(Eq. 2.5)}$$

A large extinction ratio is obtained when the value of $\xi(\lambda)$ is close to unity. In the in-fiber PCF-MZI, the cause of interference periodicity, i.e., the periodic spectral dependence of $\eta(\lambda)$ and $\xi(\lambda)$ in Eq. 2.5, is the high order cladding-mode beating and the coupling of power between the core mode and the cladding mode along the PCF. This coupling-beating phenomenon is similar to that in a dual-core fiber and can be characterized with a coupling length L_0 that represents the length for a single full coupling process [30]. It is worth noting that L_0 is wavelength dependent and polarization sensitive. Due to the variation of L_0 with wavelength, the power $I_{core}(\lambda)$ and $I_{cladding}(\lambda)$ are wavelength dependent when the light signal reaches the output end of the PCF. In theory, the spectral period should be inversely

proportional to the length of the PCF [30] which is in good agreement with our experimental result. As shown in Fig. 2.8, increasing the length of PCF from 165.0 to 82.3 cm leads to an increase of the spectral period of interference from to 6.3 to 13.1 nm.

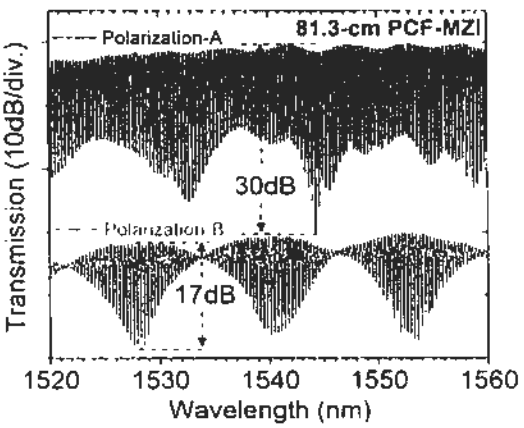

Fig. 2.9 Transmission spectra of the 82.3cm PCF-MZI measured by using swept laser source at two difference polarization states.

The transmission of the PCF-MZI usually has much larger ER when it is measured by laser source rather than ASE source, which has different optical coherence. As shown in Fig. 2.9, the largest ER is 30 dB rather than that of 15 dB in Fig. 2.8(b). The polarization sensitivity of the transmission is also shown in Fig. 2.9, indicating the tunability of the transmission by adjusting the polarization. The origin of the polarization sensitivity is mainly the mismatch splicing. Therefore, one can utilizing other types of PCF with different methods for exciting the cladding-modes, and thus reduces the polarization sensitivity.

2.3 PCF-MZI for DPSK Demodulation

In future high-speed optical communications, differential phase shift keying (DPSK) is an attractive modulation format as it offers improved receiver sensitivity with balanced detection, demonstrates robustness to nonlinear effects, and exhibits high tolerance to dispersion impairments [31, 32]. In DPSK communications, demodulation is needed to translate differential phase information into intensity information (for direct detection) using DPSK demodulators such as a MZI [32]. All-fiber MZI has been widely used in optical communications owing to its reliable performance in multiplexing, DPSK signal demodulation, and so on. The conventional all-fiber MZI uses two fiber couplers with a certain length difference between the two arms to introduce a fixed propagation delay. Similar functionalities can also be achieved by using a birefringent loop mirror, photonic bandgap fiber Lyot filter, or a delay-asymmetric nonlinear loop mirror [28, 29, 33].

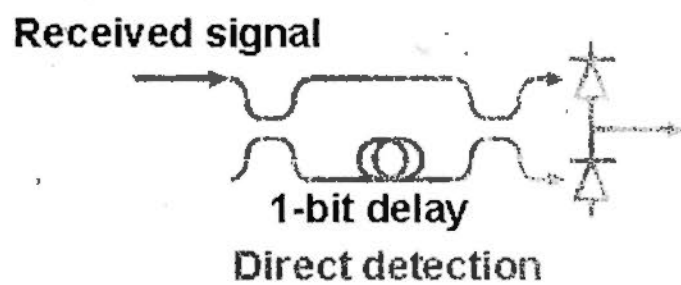

Fig. 2.10 Delay interferometer for DPSK demodulation for direct detection.

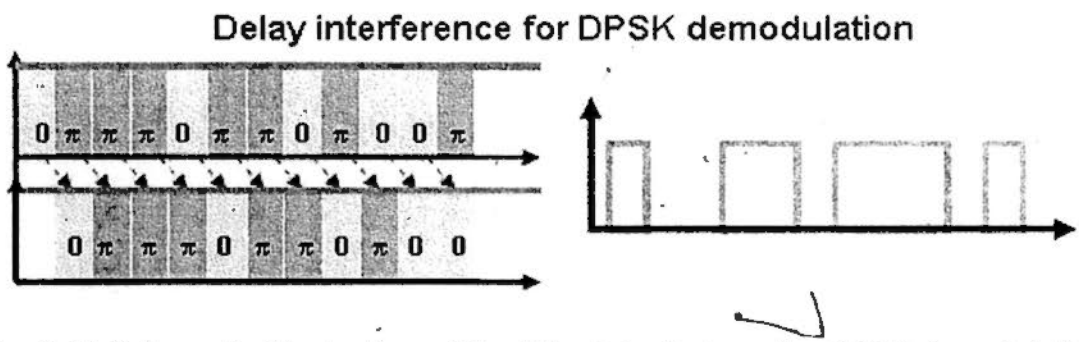

Fig. 2.11 Schematic illustration of the delay interference for DPSK demodulation.

Fig. 2.10 and Fig. 2.11 show the schematic illustrations of a DPSK demodulator for direct detection and the delay interference process in DPSK demodulation. Considering the in-fiber PCF-MZI as an in-line delay interferometer (DI), it can be directly used for demodulation of DPSK signals.

We fabricate a PCF-MZI with about 300-cm PCF that introduces 91-ps relative delay. The delay is suitable for the demodulation of 10-Gb/s DPSK signals. The transmission spectrum shown in Fig. 2.12 exhibits a maximum extinction ratio of 7.8 dB and a minimum extinction ratio of 1.1 dB (at around 1549.1 nm) for the interference transmission. The variation of the interference extinction ratio is caused by power coupling between the core mode and the cladding mode. The variation limits the PCF-MZI demodulator to operate only at periodic wavebands as the demodulation performance is degraded when the extinction ratio is small. The device is sensitive to bending and temperature. However, due to the compactness and the full silica material of PCF, the device is quite stable. The spectrum remains the same after hours, with very small temperature change and minimal vibration in our laboratory.

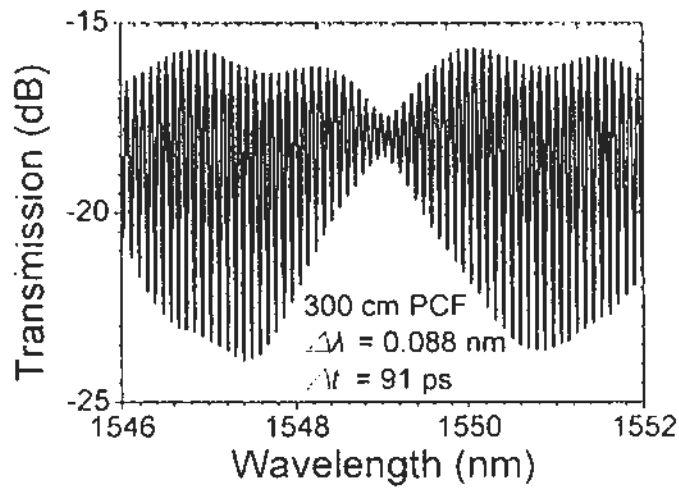

Fig. 2.12 Measured transmission spectrum of the 300-cm PCF-MZI.

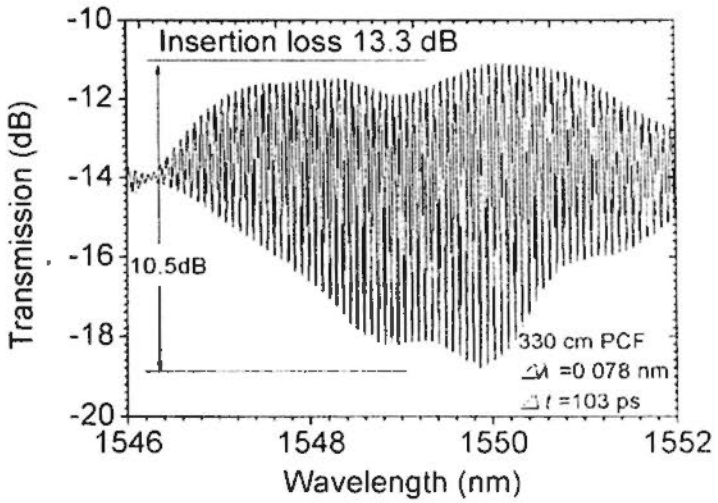

Fig. 2.13 Measured transmission spectrum of the 330-cm PCF-MZI.

Since the amount of splicing mismatch affects the splitting ratio of the input power, one can adjust the mismatch during the splicing to obtain an optimal transmission spectrum and therefore realize a large extinction ratio at the desired working waveband. Shown in Fig. 2.13 is the transmission spectrum for another PCF-MZI with 330-cm PCF, which has a largest ER of 10.5 dB.

Alternatively, the interference extinction ratio can be made tunable through polarization adjustment in the setup. Using the 300-cm PCF-MZI for 10-Gb/s DPSK demodulation, by adjusting the polarization controller (PC) before the demodulator, we have successfully realized DPSK demodulation over the whole waveband with respect to the transmission spectrum in Fig. 2.12.

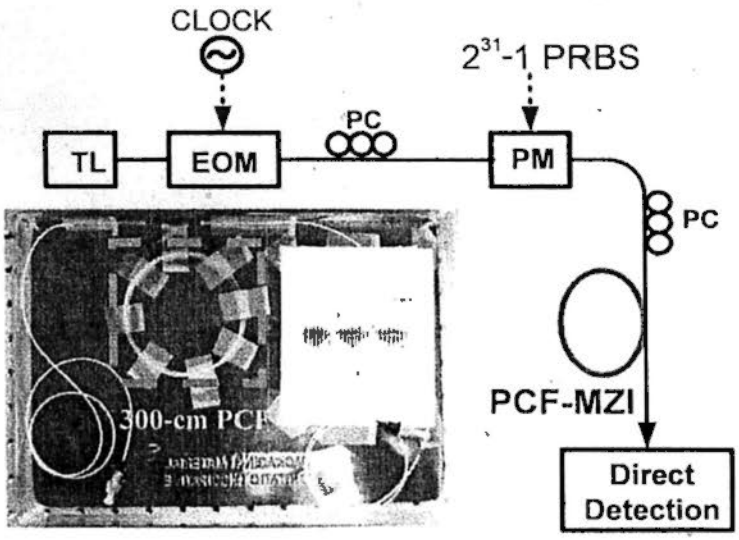

Fig. 2.14 Experimental setup for DPSK demodulation by in-fiber PCF-MZI. TL: tunable laser; PC: polarization controller; BPF: band pass filter. Inset: the picture of the 300-cm PCF-MZI.

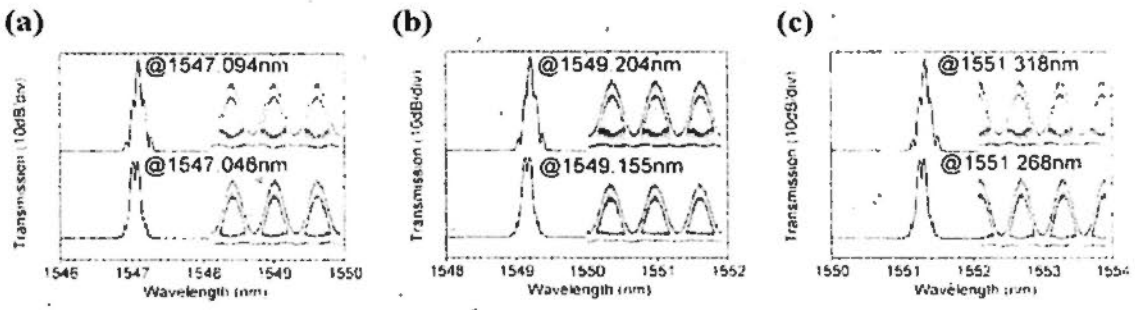

Fig. 2.15 Measured spectra and eye diagrams of the demodulated 10-Gb/s RZ-DPSK signals at (a) 1547.094 and 1547.046 nm; (b) 1549.204 and 1549.155 nm; (c) 1551.318 and 1551.268 nm. The upper and lower plots show constructive and destructive interferences, respectively.

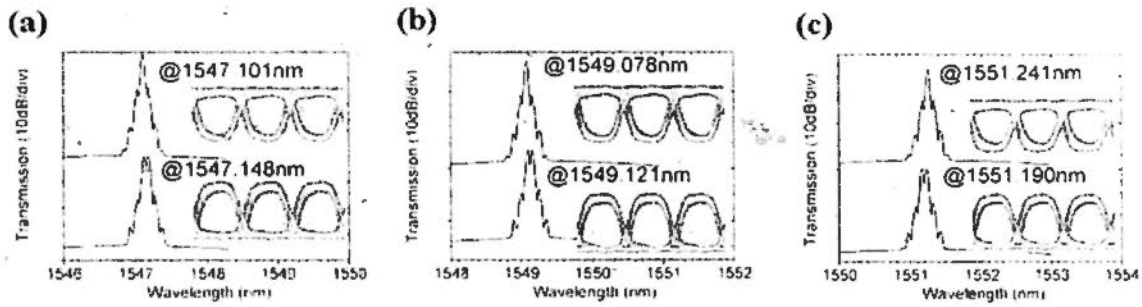

Fig. 2.16 Measured spectra and eye diagrams of the demodulated 10-Gb/s NRZ-DPSK signals at (a) 1547.101 and 1547.148 nm; (b) 1549.078 and 1549.121 nm (c)

1551.241 and 1551.190 nm. The upper and lower plots show constructive and destructive interferences, respectively.

Using the 300-cm PCF-MZI, we have realized error free demodulation of both RZ- and NRZ-DPSK signals [34]. The measured results are shown in Fig. 2.15 to Fig. 2.16. The 10 Gb/s RZ-DPSK signals, with 2^{31}-1 pseudo random binary sequence (PRBS), are generated at different wavelengths of 1547.094, 1549.204 and 1551.318 nm using a tunable laser and a phase modulator. After demodulation, clear and widely opened eye diagrams are obtained as shown in Fig. 2.15. It is worth mentioning that in Fig. 2.15(b), the demodulated eye diagrams at 1549.204 nm exhibit no degradation compared to those at 1547.094 and 1551.318 nm shown in Fig. 2.15(a) and (c), even though the interference extinction ratio at 1549.204 nm is only 1.1 dB and is much smaller than the values of 7.4 and 7.1 dB at the other two wavelengths. The reason is the polarization sensitivity of the PCF-MZI, which enables us to optimize the ER of the demodulation by adjusting the polarization.

Results of the bit error rate (BER) measurement are shown in Fig. 2.17. The BER performances at these three wavelengths are similar and the receiver sensitivity is even slightly better at 1549.204 nm. By tuning the polarization to optimize the demodulation performance during the BER measurement, we observe that the required power for error-free demodulation deviates within only 1.5 dB over the whole wavelength range from 1547 to 1552 nm, which covers one period of the variation in interference extinction ratio. Similar demodulation performance has also been achieved and measured for NRZ-DPSK signals using the same PCF-MZI, as shown in Fig. 2.16 and Fig. 2.17. These results indicate that the in-fiber PCF-MZI, as a DPSK demodulator, can operate over a wide band regardless of the

variation of interference extinction ratio that occurs at a fixed polarization. Compared to demodulation with a typical conventional DI built with fiber couplers, we obtain a 1.1-dB power penalty using our PCF-MZI [26].

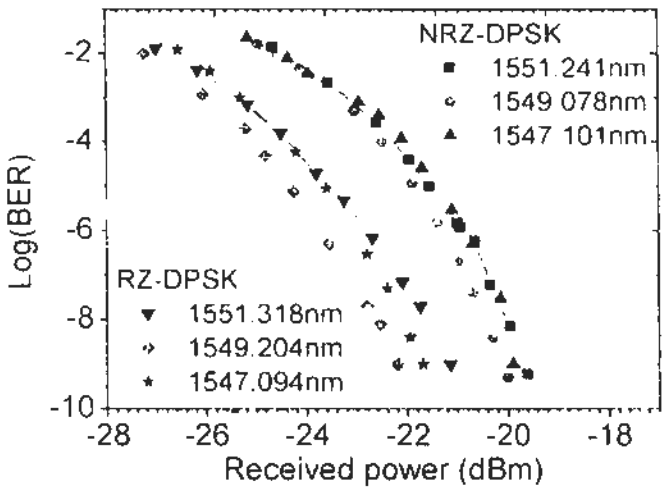

(a)

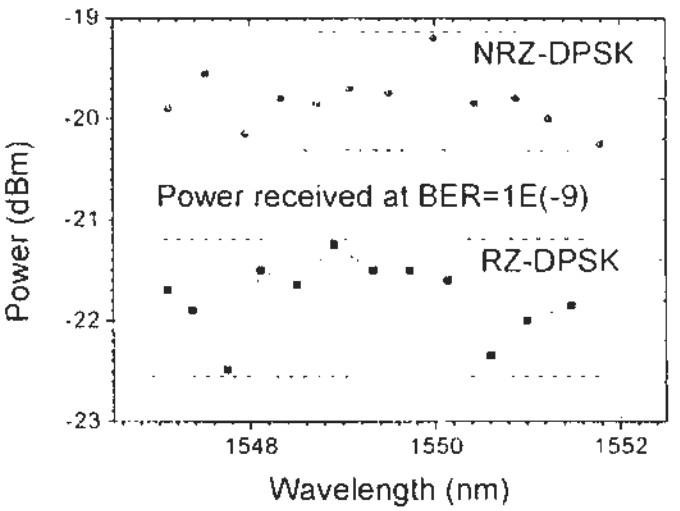

(b)

Fig. 2.17 Bit-error rate performance on the demodulation of 10 Gb/s RZ- and NRZ-DPSK signals.

It has been indicated that variable delays can be introduced for DPSK demodulation at different bit rates by using different PCF lengths. Such as 50-ps

delay for 20-Gb/s DPSK demodulation with 165-cm PCF-MZI. Shown in Fig. 2.18 are the 10-Gb/s NRZ-DPSK demodulation eye diagrams by using four kinds of PCF-MZIs with different PCF lengths: 300-cm for 91-ps delay, 165-cm for 50-ps delay, 82.3-cm for 25-ps delay and 41-cm for 12.5-ps delay. The widely opened eye diagrams with different pulse widths after the demodulation indicate the different relative delay, which can be used in DPSK demodulation at different bit rates.

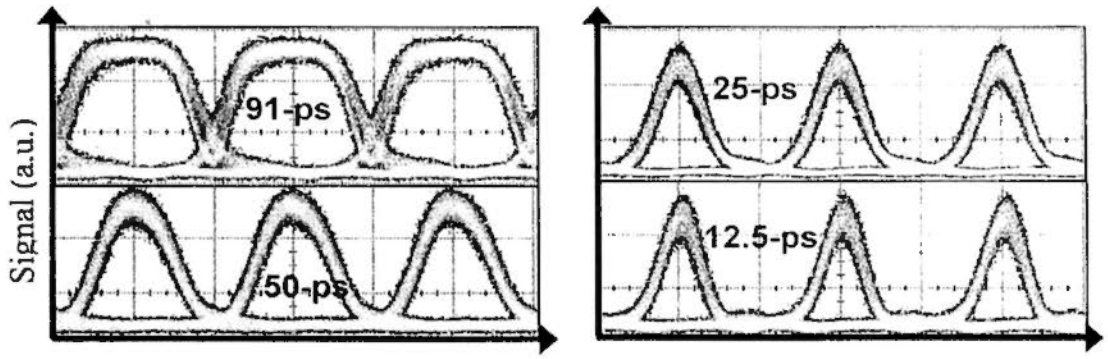

Fig. 2.18 10-Gb/s NRZ-DPSK demodulation using PCF-MZIs with different relative delays: 91-ps, 50-ps, 25-ps and 12.5-ps.

In this work, the in-fiber PCF-MZI has only one output port which limits the demodulator for use in balanced detection. This difficulty can be solved by splicing a dual-core fiber at the output end and detecting the demodulated signals in the two cores [30], while increasing the complexity of the device. There is also a tradeoff issue between polarization insensitivity and wideband demodulation. Using the cladding collapse method for fabrication can significantly reduce the polarization sensitivity [8]; however, the power coupling ratio will be wavelength dependent, thus limiting the wideband demodulation performance owing to the variation of the interference extinction ratio. By carefully controlling the collapse of cladding during fabrication, it is possible to tailor the transmission spectrum. Thus, wideband operation can still be optimized while maintaining reduced polarization sensitivity.

The improvements can also be achieved using hybrid dual core PCFs and dual-concentric PCFs. Hybrid dual core PCFs can introduce a larger delay coefficient with two cores respectively guided by total internal reflection and bandgap [35]. Dual-concentric PCFs have a symmetric structure and thus has reduced polarization sensitivity while reduced insertion loss can also be expected [36, 37].

2.4 PCF-MZI for Pulse Format Conversion

Format conversion is a highly desirable technology at the gateways between different systems owing to different characteristics of data formats and different requirements of the systems [38]. In particular, the NRZ (non return-to-zero) pulse format has a relatively high spectral efficiency and has been widely used in wavelength division multiplexing (WDM) systems, while RZ (return-to-zero) pulse format is required in optical time division multiplexing (OTDM) systems [39]. The high temporal efficiency obtained with ultra-short pulses enables the generation of ultra-high bite rate OTDM signals over one wavelength channel [40]. Therefore, the conversion between RZ and NRZ pulse formats [41, 42] is important in the gateway between the two systems [39, 43]. On the other hand, pseudo return-to-zero (PRZ) pulses can be obtained from NRZ pulses for clock tone generation even though they do not carry the original data from the NRZ signal. With NRZ-to-PRZ format conversion, all-optical clock recovery thus becomes readily available for NRZ data [44, 45].

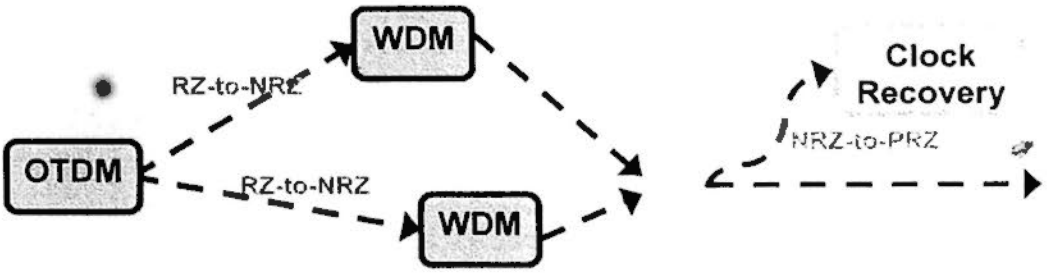

Fig. 2.19 Pulse format conversions requested in system gateways.

As previously demonstrated in Section 2.2, PCF-MZI, which is a promising solution for an all-fiber in-line delay interferometer, can have the relative delay between the two interfering branches introduced by the index difference between the core mode and the cladding mode of the PCF. Due to the unique air-hole structure of the PCF, the index difference can be quite large, implying that a short PCF can introduce a large delay while keeping attenuation of the cladding mode at a low level. The in-fiber PZF-MZI, as a delay interferometer with an in-line structure and enhanced thermal stability, has been demonstrated to perform favorably in optical sensing and in DPSK demodulation for optical communications as demonstrated in Section 2.3.

In this part of the thesis work, based on a PCF-MZI with ~165 cm PCF, we demonstrate both RZ-to-NRZ and NRZ-to-PRZ pulse format conversions for 10-Gb/s OOK signals [46]. The principles are illustrated in Fig. 2.20.

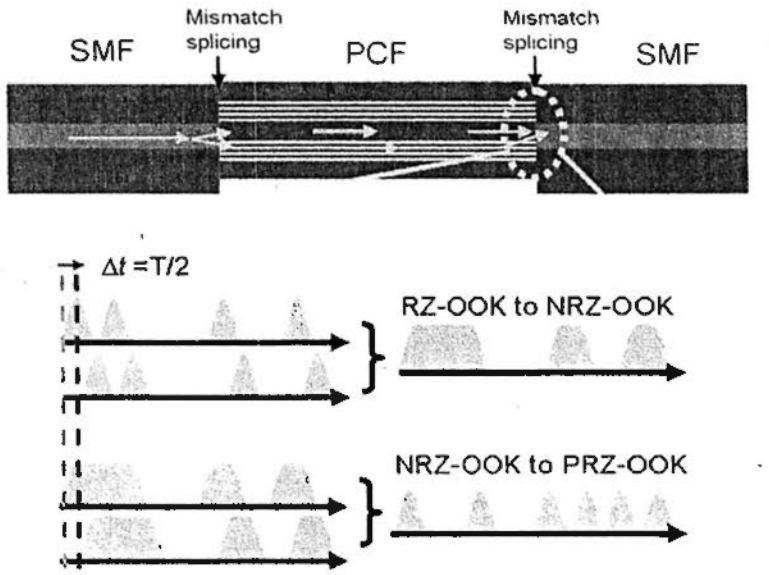

Fig 2.20 Schematic illustration of the in-fiber PCF-MZI device structure and the operation principle for the two types of pulse format conversions.

2.4.1 PCF-MZI for RZ-to-NRZ Pulse Format Conversion

With a suitable PCF to introduce an appropriate relative delay (Δt), like a half-bit delay (T/2), the in-fiber PCF-MZI can be used for RZ-to-NRZ and NRZ-to-PRZ pulse format conversions for OOK signals. The inset in Fig. 2.20 schematically shows the operation principles for the conversions in the time domain. The core-mode light and the cladding-mode light, with the same data (RZ or NRZ sequence: 1100101) but different delays (T/2 delay difference), are recombined at the splicing point at the output. With constructive interference, the RZ pulses will be shaped into NRZ pulses. Similarly, the NRZ pulses will be shaped into PRZ pulses with destructive interference.

Fig. 2.21 shows the experiment setup for RZ-to-NRZ pulse format conversion. A 10-Gb/s RZ-OOK signal is generated at 1549.8-nm using two electro-optic modulators (EOMs), one for intensity modulation and the other for pulse carving. The duty cycle is 50%. The signal undergoes RZ-to-NRZ format

conversion after its transmission in the in-fiber PCF-MZI, which is built with only ~165 cm PCF to introduce 50-ps relative delay for the interference. The delay results in a transmission spectrum with ~10 dB interference contrast ratio as shown in Fig. 2.22 (the red curve).

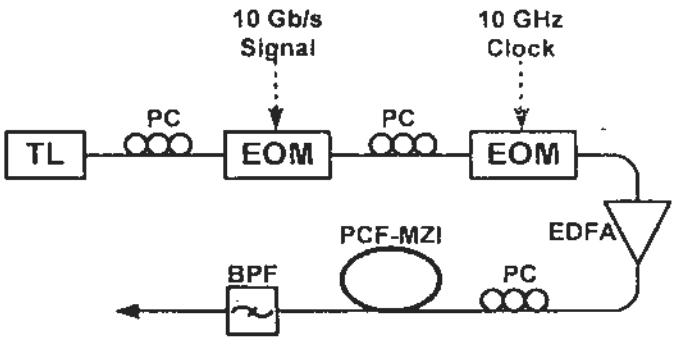

Fig. 2.21 Experimental setup for in-fiber PCF-MZI based pulse format conversion. TL: tunable laser; PC: polarization controller; BPF: band pass filter.

The DI transmission spectrum shows a destructive interference at the sidebands and a constructive interference at the center carrier frequency of the input 10-Gb/s RZ-OOK signal (pseudo random binary sequence, PRBS, 2^{31}-1). With the two sideband tones suppressed by destructive interference of the in-fiber PCF-MZI, the output signal has been converted to an NRZ-OOK signal by spectral shaping. The output spectrum obtained after 0.3-nm Gaussian filtering (3-dB bandwidth) is shown at the bottom of Fig. 2.22 (the blue curve). The filter is simply used for amplified spontaneous emission (ASE) noise filtering instead of for further suppression of the sideband tones.

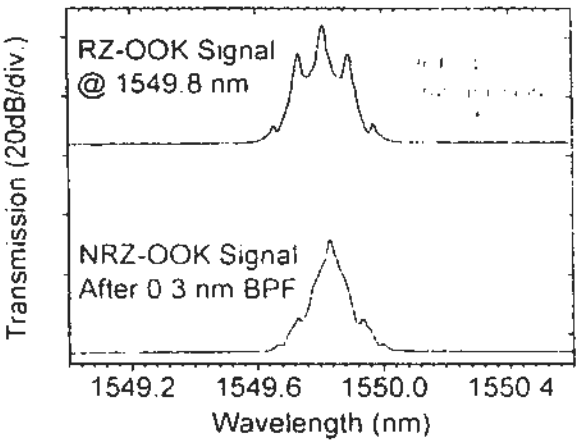

Fig. 2.22 Spectra of the input RZ signals (upper), PCF-MZI transmission (middle) and output NRZ signals (bottom). BPF: band pass filter.

The operation for an input waveform with a fixed pattern of "1100101" is investigated. The results are depicted in Fig. 2.23(a), clearly showing the pulse format conversion from RZ-OOK to NRZ-OOK. Next, with the PRBS data, we perform bit error rate (BER) measurement. The result is shown in Fig. 2.23(b). A power penalty of ~1 dB is observed at the error free detection level (BER=10^{-9}).

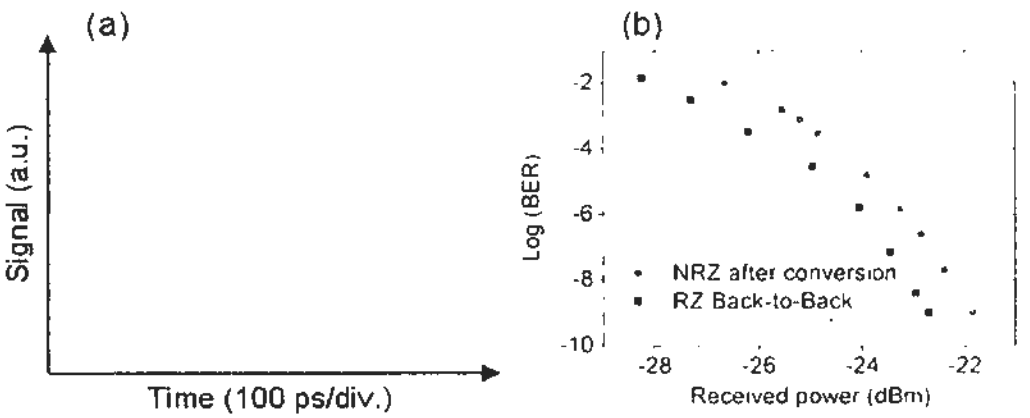

Fig. 2.23 RZ-to-NRZ format conversion for 10-Gb/s OOK signals with a duty cycle of 50%. (a) Input RZ (upper) and output NRZ (bottom) waveforms for a data sequence of 1100101; (b) BER measurement result showing a 1-dB power penalty after the conversion.

We also studied the effectiveness of our scheme for pulse format conversion of RZ input signals with different duty cycles. The input and output eye diagrams are shown Fig. 2.24. It is observed that the output extinction ratios for input duty cycles of 36%, 50%, and 63% are 14 dB, 11 dB, and 9 dB, respectively. The result indicates a more effective suppression of the side tones for input data pulses with a lower duty cycle within the range.

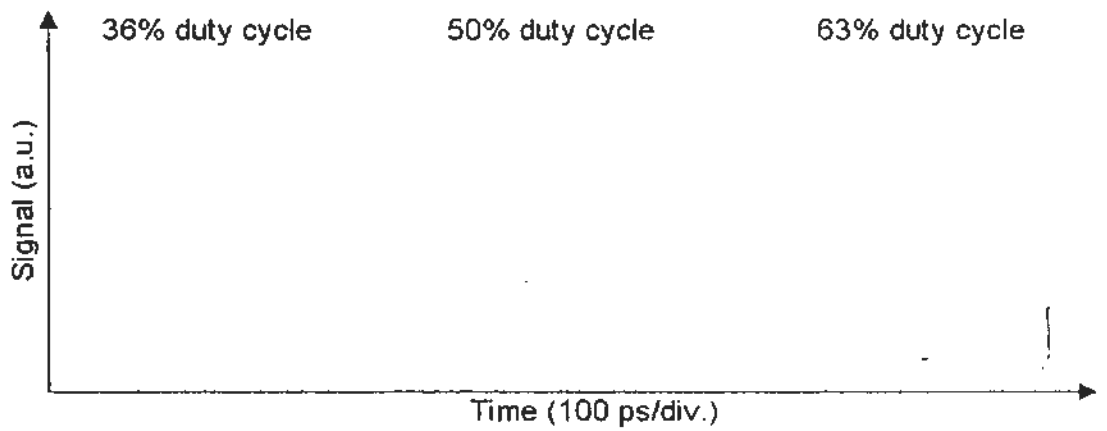

Fig. 2.24 Eye diagrams for RZ-to-NRZ format conversions for 10-Gb/s OOK signals with duty cycles of 36%, 50% and 63%. Upper: input RZ-OOK signals; Lower: output NRZ-OOK signals.

The interference contrast ratio of the in-fiber PCF-MZI varies periodically with the wavelength as indicated in Fig. 2.9. A period of 6.3-nm has been obtained for the 165-cm PCF-MZI. The variation of the interference contrast ratio is caused by directional coupling between the core and the cladding modes. As analyzed in Section 2.2, a wideband operation is still achievable regardless of the variation of the interference contrast ratio, simply by polarization adjustment. Fig. 2.25 shows the NRZ-OOK eye diagrams obtained from 50% duty cycle RZ-OOK input signal at three different wavelengths: 1550.8 nm, 1553.8 nm and 1557.3 nm, covering one

whole period (6.3 nm) of the interference contrast ratio variation. The widely opened NRZ eyes indicate successful wideband operation capability of RZ-to-NRZ pulse format conversion.

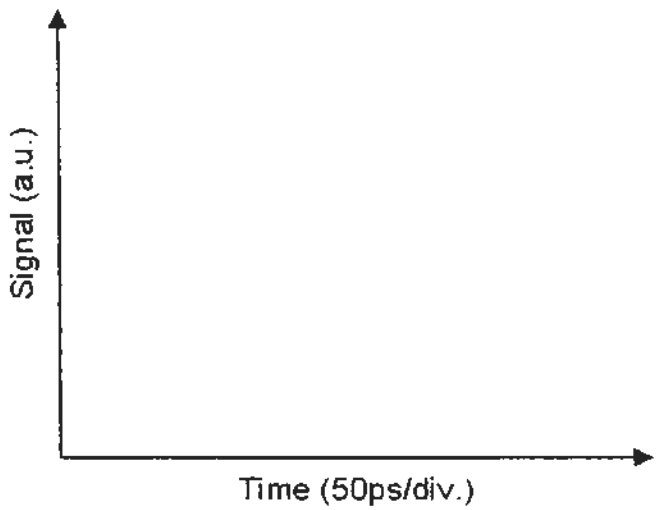

Fig. 2.25 NRZ eye diagrams obtained from 50% duty cycle RZ-OOK signal at 1550.8 nm (bottom), 1553.8 nm (middle), and 1557.3 nm (upper).

2.4.2 PCF-MZI for NRZ-to-PRZ Pulse Format Conversion

For NRZ-to-PRZ format conversion, we adopt nearly the same setup to generate 10-Gb/s NRZ-OOK signals, except that the second EOM for pulse curving has been removed. The pulse format conversion is achieved by destructive interference using the same in-fiber PCF-MZI. The input NRZ and the output PRZ spectra are shown in Fig. 2.26 (with PRBS input). The ~50 ps delay results in a destructive interference at the carrier frequency and changes the shape of the spectrum. A 0.3-nm filter is also used here for ASE noise suppression.

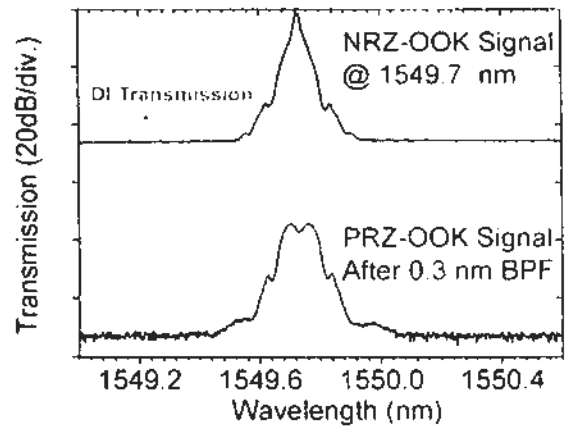

Fig. 2.26 Spectra of the input signals (upper), PCF-MZI transmission (middle), and output signals (lower).

In the time domain, the output signals show an RZ waveform for a fixed input pattern of "1100101" and an RZ eye diagram for PRBS input. The results are shown in Fig. 2.27 and Fig. 2.28. The converted RZ signal has a widely opened eye with an extinction ratio of 8 dB. It should be noted that the outputs do not carry the exact original data and are in fact PRZ signals, which is now readily for use in clock recovery of the NRZ-OOK signals. Meanwhile, the 165-cm in-fiber PCF-MZI can also be used in clock recovery of 10-Gb/s NRZ-DPSK signals since the demodulation of signals is achievable using a 50-ps relative delay between the interfering branches [26, 45, 47].

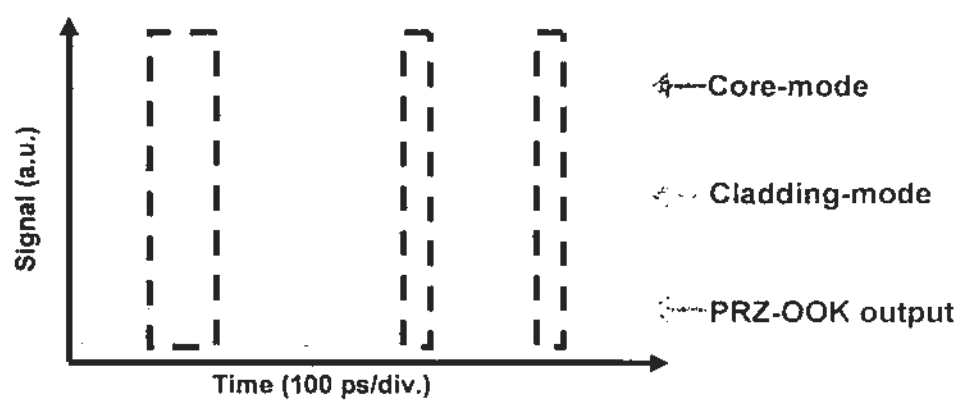

Fig. 2.27 The waveforms of the NRZ-to-PRZ pulse format conversion showing the destructive interference.

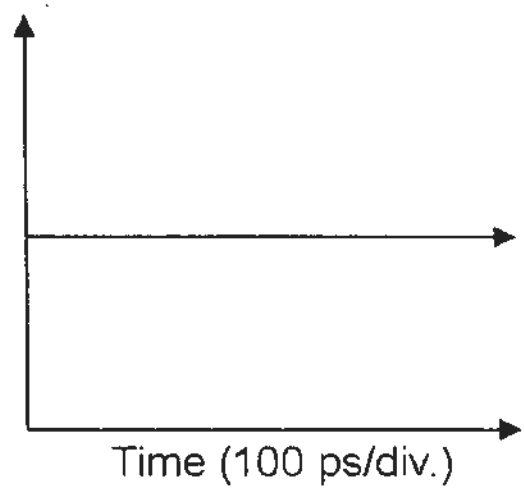

Fig. 2.28 The eye diagrams of the NRZ and PRZ pulses.

With a shorter length of PCF to introduce a smaller delay, the in-fiber PCF-MZI can be further developed for higher speed RZ-to-NRZ and NRZ-to-PRZ format conversions. Improvements can also be made by using PCFs with various kinds of specially designed structures to minimize the insertion loss or to further shorten the required fiber length, as we have discussed in Section 2.3.

2.5 PCF-MZI for Repetition Rate Multiplication and OTDM Signal Generation

Optical pulses are widely used in optical communication to carry digital data, or in optical nonlinear process to obtain a high peak power. The periodically varying optical field leads to an optical spectrum with multiple frequency carriers, as a result of the Fourier transform. Optical pulse source can be obtained by pulsed lasers as well as direct external electric-optic modulations.

In next generation optical communication systems, high repetition rate optical pulses are very much desirable for high speed optical signal generation. Limited by the speed of the electronic components, direct generation of a high speed pulse source is usually difficult. Therefore, the external multiplication of the repetition rate based on delay interferometers has drawn much attention for high repetition rate optical pulse source generation, as well as high bit rate OTDM signal generation [48-51].

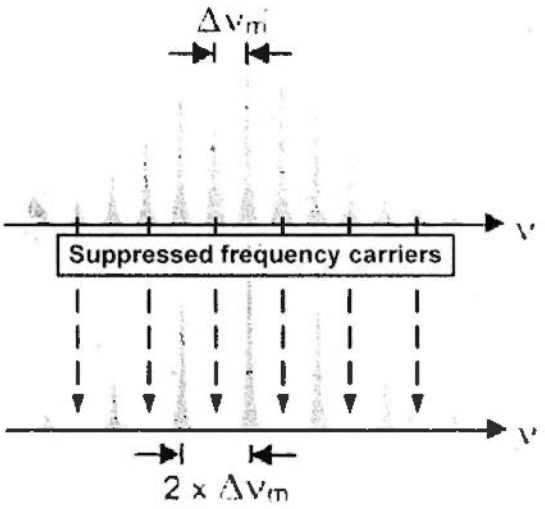

Fig. 2.29 Frequency domain illustration of repetition rate multiplication.

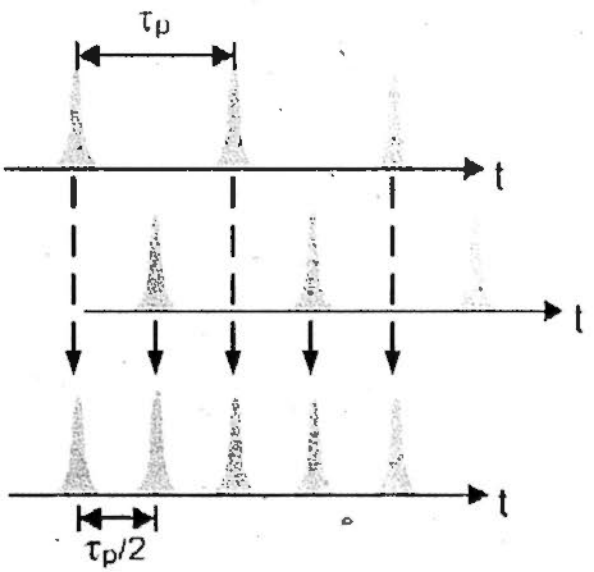

Fig. 2.30 Time domain illustration of repetition rate multiplication.

The principle of the repetition rate multiplication in frequency domain is shown in Fig. 2.29, in which Δv_m is the repetition rate and also the frequency spacing between the adjacent carriers in the spectrum of an optical pulse source. The multiplication will suppress the carriers alternatively and results in a spectrum with doubled frequency spacing of $2\times \Delta v_m$. In time domain, it is a recombining of two pulse trains with same repetition rate. A relative delay of half period ($\tau_p/2$) is introduced so that the recombined pulse train has a new period of $\tau_p/2$ and thus doubles the repetition rate, as shown in Fig. 2.30.

The comb filtering transmission of PCF-MZI can alternatively suppress the frequency carriers with a FSR equals to half of the repetition rate of a pulse source. In time domain, this process includes two processes. First, the low repetition rate pulses are split into core-mode and cladding-mode which are propagating with different speeds in the PCF. Second, with certain length of PCF to introduce a half period delay, the temporally interleaved core-mode and cladding-mode pulses are recombined together and forming a pulse train with multiplied repetition rate. Based on PCF-MZI, the variable pulse delay of a 10-GHz optical pulse train is obtained as shown in Fig. 2.31, with 50-ps, 25-ps and 12.5-ps introduced by 165-cm, 81-cm and 41-cm PCF, respectively.

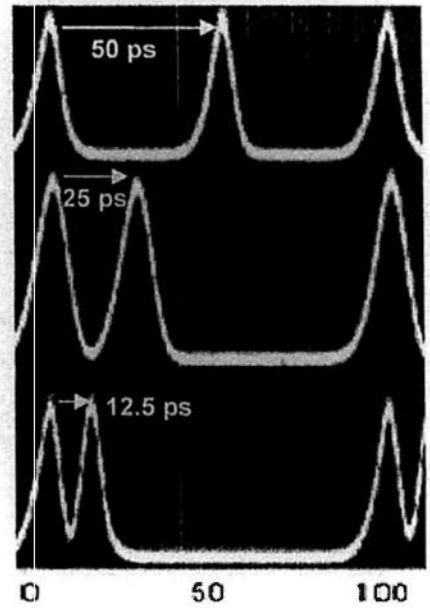

Fig. 2.31 Variable pulse delays after different PCF-MZI transmission.

The spectra of 10-to-20 GHz repetition rate multiplication is experimentally shown in Fig. 2.32. The multiplication is based on a 165-cm PCF-MZI which has a comb transmission as shown in Fig. 2.9. The output eye diagram of the 20-GHz pulse train is also obtained as shown in Fig. 2.33.

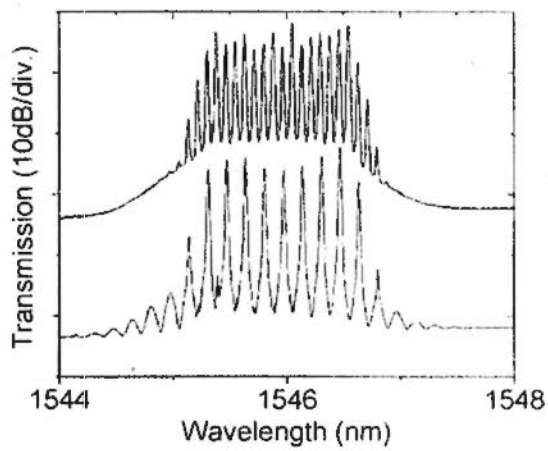

Fig. 2.32 Spectra of the repetition rate multiplication with alternatively suppressed frequency carriers after PCF-MZI transmission.

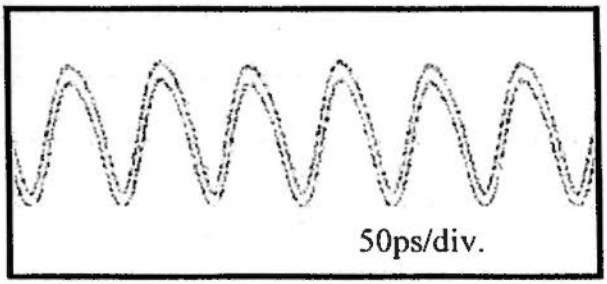

Fig. 2.33 Waveform of the 20-GHz pulse train obtained by repetition rate multiplication from a 10-GHz pulse.

Since it is simple to fabricate a PCF-MZI with a short length of PCF, such as several centimeters, it is expected to have less complexity of repetition rate multiplication up to hundreds of Gigahertz. Shown in Fig. 2.34 are the waveforms of using PCF-MZI for repetition rate multiplications, including 40-to-80 GHz multiplication and 80-to-160 GHz multiplication. In Fig. 2.34(a), 40-GHz input pulse (upper) is obtained by external modulation of a CW laser; In Fig. 2.34(b), 80-GHz input pulse (upper) is obtained by time division multiplexing of a 10-GHz mode-locked fiber laser source with a multiplexing factor of eight.

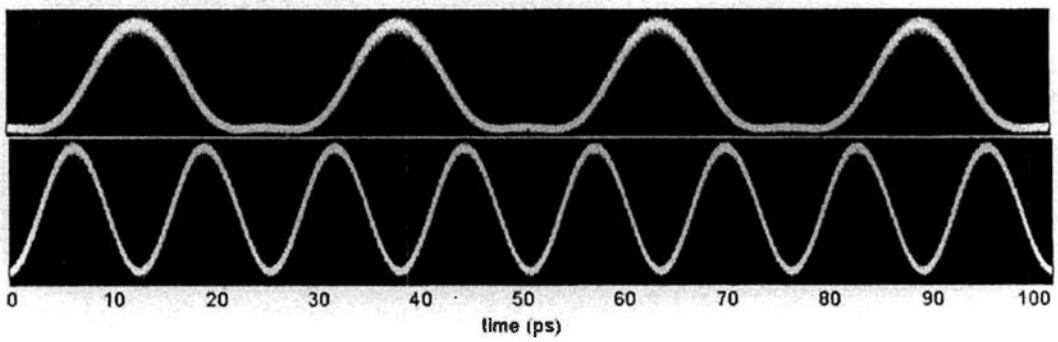

(a)

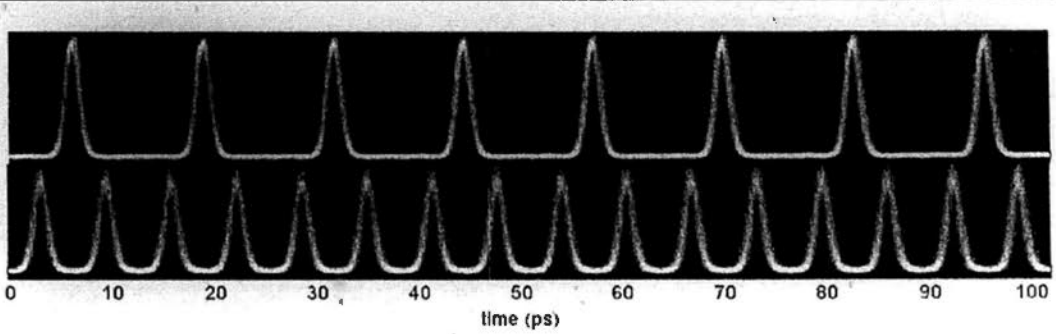

(b)

Fig. 2.34 Waveforms for 40-to-80 GHz and 80-to-160 GHz repetition rate multiplications.

PCF-MZI can also be used for time division multiplexing to generate high speed OTDM signals for signal processing and testing in subsystems. Fig. 2.35 shows the process of using PCF-MZI for 160-Gb/s OTDM signal generation. The 80-Gb/s OTDM signal is obtained by commercial OTDM multiplier which has three stages of 1X2 multiplexing, and thus enables us to multiplex the input 10-Gb/s OOK signal with a factor of eight. The PCF-MZI has 20.4-cm PCF which introduces 6.2-ps relative delay for the multiplexing. The obtained 160-Gb/s OTDM signal has a timing jitter of ~140-fs, which is almost the same compared with that obtained by commercial multiplier with the smallest jitter of ~130 fs, indicating the well performed stability of PCF-MZI.

Since the multiplexing is achieved with only half period delay without de-correlation, the output OTDM signal will not be PRBS even with PRBS input, which makes the multiplexed output as a Pseudo OTDM signal.

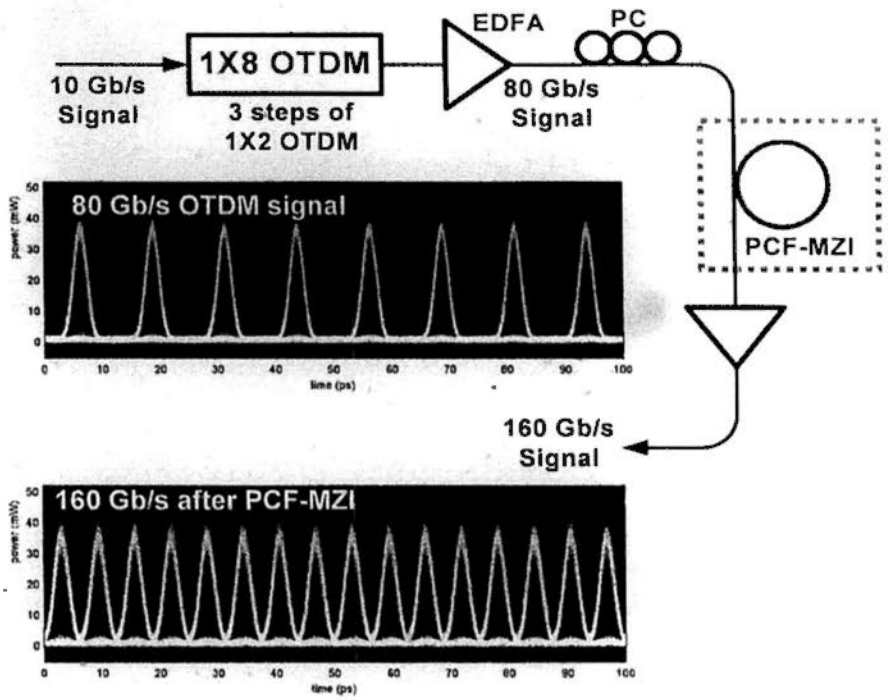

Fig. 2.35 160-Gb/s OTDM signal generation based on time division multiplexing using 20.4-cm PCF-MZI.

We have further investigated the time division multiplexing to obtain 320 Gb/s OTDM signal based on PCF-MZI. The 160-to-320 Gb/s multiplexing is based on the PCF-MZI with 10.4-cm PCF, which has the picture shown in Fig. 2.36. Its spectrum is shown in Fig. 2.37, which indicates a frequency spacing of 2.51 nm and thus a relative delay of 3.18 ps.

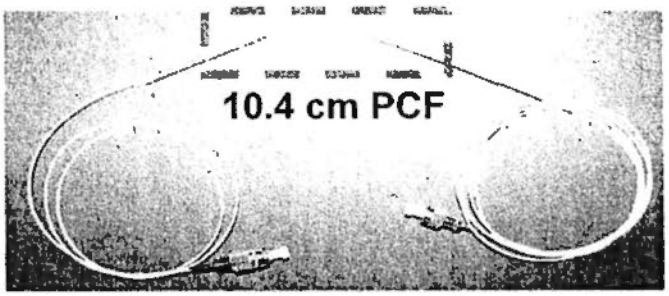

Fig. 2.36 PCF-MZI with 10.4-cm PCF.

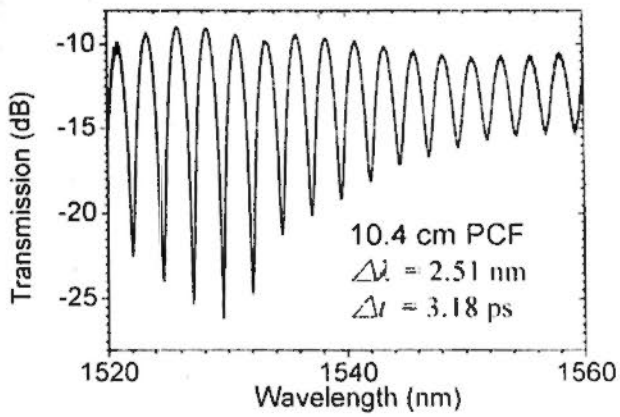

Fig. 2.37 Transmission spectrum of the 10.4-cm PCF-MZI.

The input 160-Gb/s OTDM signal has firstly been compressed by dispersion compensation and nonlinear processing [52]. The compressed 160-Gb/s OTDM signal has a pulse width of 1 ps and a timing jitter of ~150 fs. After the multiplexing by the PCF-MZI, 320-Gb/s OTDM is obtained with 1.1-ps pulse width and ~200-fs timing jitter, as shown in Fig. 2.38.

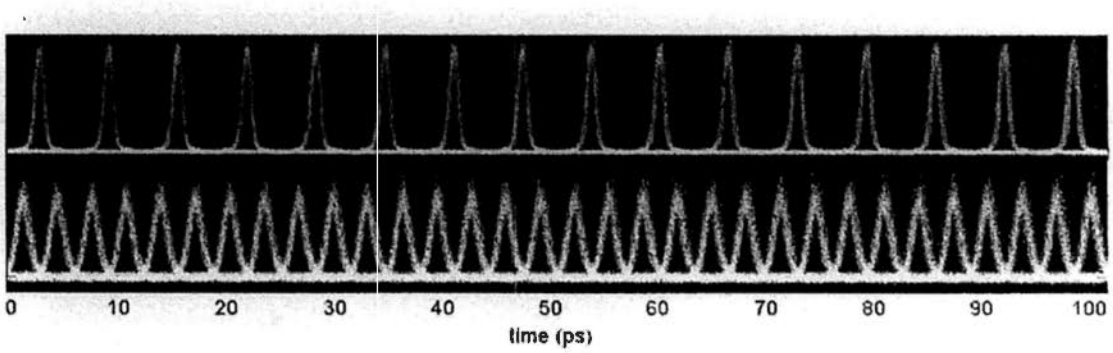

Fig. 2.38 320-Gb/s OTDM signal generation based on time division multiplexing using 10.4-cm PCF-MZI.

We can also fabricate PCF-MZI suits higher bit rate multiplexing, e.g. 640-Gb/s OTDM generation. To achieve that, further pulse compressing is required. Higher speed signal processing utilizing nonlinear effects can thus be activated.

References

[1]. T. A. Birks, J. C. Knight, and P. St.J. Russell, "Endlessly single-mode photonic crystal fiber," Opt. Lett. **22**, 961-963 (1997)

[2]. Cicero Martelli, John Canning, Nathaniel Groothoff, and Katja Lyytikainen, "Strain and temperature characterization of photonic crystal fiber Bragg gratings," Opt. Lett. **30**, 1785-1787 (2005)

[3]. Danny Noordegraaf, Lara Scolari, Jesper Lægsgaard, Lars Rindorf, and Thomas Tanggaard Alkeskjold, "Electrically and mechanically induced long period gratings in liquid crystal photonic bandgap fibers," Opt. Express **15**, 7901-7912 (2007)

[4]. Byeong Ha Lee, Joo Beom Eom, Jinchae Kim, Dae Seung Moon, Un-Chul Paek, and Gil-Ho Yang, "Photonic crystal fiber coupler," Opt. Lett. **27**, 812-814 (2002)

[5]. P. Roberts, F. Couny, H. Sabert, B. Mangan, D. Williams, L. Farr, M. Mason, A. Tomlinson, T. Birks, J. Knight, and P. St. J. Russell, "Ultimate low loss of hollow-core photonic crystal fibres," Opt. Express **13**, 236-244 (2005)

[6]. Thomas Larsen, Anders Bjarklev, David Hermann, and Jes Broeng, "Optical devices based on liquid crystal photonic bandgap fibres," Opt. Express **11**, 2589-2596 (2003)

[7]. Benjamin Eggleton, Charles Kerbage, Paul Westbrook, Robert Windeler, and Arturo Hale, "Microstructured optical fiber devices," Opt. Express **9**, 698-713 (2001)

[8]. H. Y. Choi, M. J. Kim, and B. H. Lee, "All-fiber Mach-Zehnder type interferometers formed in photonic crystal fiber," Opt. Express **15**, 5711-5720 (2007)

[9]. W. N. MacPherson et al. "Remotely addressed optical fibre curvature sensor using multicore photonic crystal fibre," Opt. Commun. **193**, 97-104 (2001).

[10]. Do-Hyun Kim and Jin Kang, "Sagnac loop interferometer based on polarization maintaining photonic crystal fiber with reduced temperature sensitivity," Opt. Express **12**, 4490-4495 (2004)

[11]. Tao Wei, Yukun Han, Yanjun Li, Hai-Lung Tsai, and Hai Xiao, "Temperature-insensitive miniaturized fiber inline Fabry-Perot interferometer for highly sensitive refractive index measurement," Opt. Express **16**, 5764-5769 (2008)

[12]. Yun-Jiang Rao, Ming Deng, De-Wen Duan, Xiao-Chen Yang, Tao Zhu, and Guang-Hua Cheng, "Micro Fabry-Perot interferometers in silica fibers machined by femtosecond laser," Opt. Express **15**, 14123-14128 (2007)

[13]. Q. Shi, Z. Wang, L. Jin, Y. Li, H. Zhang, F. Lu, G. Kai, and X. Dong, "A hollow-core photonic crystal fiber cavity based multiplexed Fabry-Pérot interferometric strain sensor system," IEEE Photon. Technol. Lett. **20**(15), 1329–1331 (2008)

[14]. J. Villatoro, V. P. Minkovich, V. Pruneri, and G. Badenes, "Simple all-microstructured-optical-fiber interferometer built via fusion splicing," Opt. Express **15**, 1491-1496 (2007).

[15]. J. H. Lim, H. S. Jang, K. S. Lee, J. C. Kim, and B. H. Lee, "Mach-Zehnder interferometer formed in a photonic crystal fiber based on a pair of long-period fiber gratings," Opt. Lett. **29**, 346-348 (2004).

[16]. Y. Jung, S. Lee, B. H. Lee, and K. Oh, "Ultracompact in-line broadband Mach-Zehnder interferometer using a composite leaky hollow-optical-fiber waveguide," Opt. Lett. **33**, 2934-2936 (2008)

[17]. J. Villatoro, V. Finazzi, V.P. Minkovich, V. Pruneri, G. Badenes, "Temperature-insensitive photonic crystal fiber interferometer for absolute strain sensing," Appl. Phys. Lett. **91**, 091109, (2007)

[18]. J. L. Villatoro, V. P. Minkovich, and D. Monzón-Hernández, "Compact modal interferometer built with tapered microstructured optical fiber," IEEE Photon. Technol. Lett. **18**(11), 1258–1260 (2006)

[19]. S. H. Aref, R. Amezcua-Correa, J. P. Carvalho, O. Frazão, P. Caldas, J. L. Santos, F. M. Araújo, H. Latifi, F. Farahi, L. A. Ferreira, and J. C. Knight, "Modal interferometer based on hollow-core photonic crystal fiber for strain and temperature measurement," Opt. Express **17**, 18669-18675 (2009)

[20]. W. Bock, T. Eftimov, P. Mikulic, and J. Chen, "An inline core-cladding intermodal interferometer using a photonic crystal fiber," J. Lightwave Technol. **27**(17), 3933–3939 (2009)

[21]. Hyun Chul Park, In Kag Hwang, Dong Il Yeom, and Byoung Yoon Kim, "Analyses of cladding modes in photonic crystal fiber," Opt. Express **15**, 15154-15160 (2007)

[22]. A. Diez, T. A. Birks, W. H. Reeves, B. J. Mangan, and P. St. J. Russell, "Excitation of cladding modes in photonic crystal fibers by flexural acoustic waves," Opt. Lett. **25**, 1499-1501 (2000)

[23]. Rodrigo M. Gerosa, Danilo H. Spadoti, Leonardo de S. Menezes, and Christiano J. S. de Matos, "In-fiber modal Mach-Zehnder interferometer

based on the locally post-processed core of a photonic crystal fiber," Opt. Express **19**, 3124-3129 (2011)

[24]. K. Saitoh and M. Koshiba, "Full-vectorial imaginary-distance beam propagation method based on finite element scheme: Application to photonic crystal fibers," IEEE J. Quantum Electron. **38**, 927-933, (2002)

[25]. Kunimasa Saitoh, M. Koshiba, T. Hasegawa, and E. Sasaoka, "Chromatic dispersion control in photonic crystal fibers: application to ultra-flattened dispersion," Opt. Express **11**, 843-852 (2003)

[26]. J. Du, Y. Dai, G. K.P. Lei, W. Tong, and C. Shu, "Demodulation of DPSK signals using in-line Mach-Zehnder interferometer based on photonic crystal fibers," p.FM6, in the 14th Opto-Electronics and Communications Conference, Hong Kong, July (2009)

[27]. Y. K. Lize, R. Gomma, and R. Kashyap, "Low-cost multimode fiber Mach Zehnder interferometer for differential phase demodulation," v.6314, p.63140R.1-7, in Photorefractive Fiber and Crystal Devices: Materials, Optical Properties, and Applications XII, San Diego, USA, August (2006)

[28]. C. W. Chow, and H. K. Tsang, "Polarization-independent DPSK demodulation using a birefringent fiber loop," IEEE Photon. Technol. Lett. **17**, 1313-1315 (2005)

[29]. C. Peucheret, Y. Geng, B. Zsigri, T. T. Alkeskjold, T. P. Hansen, and P. Jeppesen, "Demodulation of DPSK signals up to 40 Gb/s using a highly birefringent photonic bandgap fiber," IEEE Photon. Technol. Lett. **18**, 1392-1394 (2006)

[30]. K. Saitoh, Y. Sato, and M. Koshiba, "Coupling characteristics of dual-core photonic crystal fiber couplers," Opt. Express **11**, 3188-3195 (2003)

[31]. A. H. Gnauck and P. J. Winzer, "Optical phase-shift-keyed transmission," J. Lightwave Technol. **23**, 115-130 (2005)

[32]. Peter J. Winzer and Renè-Jean Essiambre, "Advanced Modulation Formats for High-Capacity Optical Transport Networks," J. Lightwave Technol. **24**, 4711-4728 (2006)

[33]. M. P. Fok and C. Shu, "Delay-asymmetric nonlinear loop mirror for DPSK demodulation," Opt. Lett. **33**, 2845-2847 (2008)

[34]. Jiangbing Du, Yongheng Dai, Gordon K. P. Lei, Weijun Tong, and Chester Shu, "Photonic crystal fiber based Mach-Zehnder interferometer for DPSK signal demodulation," Opt. Express **18**, 7917-7922 (2010)

[35]. Xiwen Sun, "Wavelength-selective coupling of dual-core photonic crystal fiber with a hybrid light-guiding mechanism," Opt. Lett. **32**, 2484-2486 (2007)

[36]. F. Gérôme, J.-L. Auguste, and J.-M. Blondy, "Design of dispersion-compensating fibers based on a dual-concentric-core photonic crystal fiber," Opt. Lett. **29**, 2725-2727 (2004)

[37]. Chin-ping Yu, Jia-hong Liou, Sheng-shuo Huang, and Hung-chun Chang, "Tunable dual-core liquid-filled photonic crystal fibers for dispersion compensation," Opt. Express **16**, 4443-4451 (2008)

[38]. J. Leuthold, J. Jaques, and S. Cabot, "All-optical wavelength conversion and regeneration," in Proceedings of the Optical Fiber Communication (OFC), 2004, WN1.

[39]. H. Sotobayashi, W. Chujo, and K. Kitayama, "Photonic gateway: TDM-to-WDM-to-TDM conversion and reconversion at 40 Gbit/s (4 channels x 10 Gbits/s)," J. Opt. Soc. Amer. B **19**, 2810–2816, (2002).

[40]. H. C. H. Mulvad, M. Galili, L. K. Oxenløwe, H. Hu, A. T. Clausen, J. B. Jensen, C. Peucheret, and P. Jeppesen, "Demonstration of 5.1 Tbit/s data capacity on a single-wavelength channel," Opt. Express **18**, 1438-1443 (2010)

[41]. S. H. Lee, K. K. Chow, and C. Shu, "Spectral filtering from a cross-phase modulated signal for RZ to NRZ format and wavelength conversion," Opt. Express **13**, 1710-1715 (2005)

[42]. Y. Yu, X. Zhang, D. Huang, L. Li, and W. Fu, "20Gb/s All-optical format conversion from RZ signals with different duty-cycles to NRZ signals," IEEE Photon. Technol. Lett. **19**, 1027-1029, (2007)

[43]. G. K. P. Lei, C. Shu, and M. P. Fok, "All-optical OTDM to WDM signal conversion using cross absorption modulation with time- and wavelength-interleaved short pulse," IEEE Photon. Technol. Lett. 22, 571-573, (2010).

[44]. L. Zhou, H. Chen and A. W. Poon, "On-Chip NRZ-to-PRZ format conversion using narrow-band silicon microring resonator-based notch filters," J. Lightwave Technol. **26**, 1950-1955, (2008)

[45]. S. W. Jeon, T. Y. Kim, W. B. Kwon and C. S. Park, "All-optical clock extraction from 10-Gbit/s NRZ-DPSK data using modal interference in a two-mode fiber," Opt. Comm. **283**, 522-527 (2010)

[46]. J. Du, Y. Dai, G. K. Lei, H. Wei, and C. Shu, "RZ-to-NRZ and NRZ-to-PRZ Format Conversions Using a Photonic Crystal Fiber Based Mach-Zehnder Interferometer," in Optical Fiber Communication Conference, OSA Technical Digest (CD) (Optical Society of America, 2010), paper OMO4.

[47]. Jiangbing Du, Yongheng Dai, Gordon K. P. Lei, Weijun Tong, and Chester Shu, "Photonic crystal fiber based Mach-Zehnder interferometer for DPSK signal demodulation," Opt. Express **18**, 7917-7922 (2010)

[48]. Miguel A. Preciado and Miguel A. Muriel, "All-pass optical structures for repetition rate multiplication," Opt. Express **16**, 11162-11168 (2008)

[49]. Ju Han Lee, You Chang, Young-Geun Han, Sang Kim, and Sang Lee, "2 - 5 times tunable repetition-rate multiplication of a 10 GHz pulse source using a linearly tunable, chirped fiber Bragg grating," Opt. Express **12**, 3900-3905 (2004)

[50]. M. P. Fok, W. W. Tang, and C. Shu, "Repetition rate multiplication of multi-wavelength pulses by spectral elimination with a birefringence loop mirror filter," Opt. Express **13**, 4752-4758 (2005)

[51]. C. Kouloumentas, C. Stamatiadis, P. Zakynthinos, and H. Avramopoulos, "Repetition Rate Multiplication of Pseudorandom Bit Sequences" IEEE Photon. Technol. Lett. **21**, 456 (2009).

[52]. A. J. Wiberg, C.-S. Brès, B. P. P. Kuo, J. X. Zhao, N. Alic, and S. Radic, "Pedestal-free pulse source for high data rate optical time-division multiplexing based on fiber-optical parametric processes," IEEE J. Quantum Electron. **45**(11), 1325-1330 (2009)

Chapter 3: Optical OFDM Generation and DEMUX

Orthogonal frequency division multiplexing (OFDM) is a well-known and widely used technology in wired and wireless electrical communication systems because of its improved performance to overcome the inter-symbol interference (ISI) caused by a dispersive channel [1]. OFDM has been used in the physical layer interface for wireless systems including WiFi, WiMax, DSL and the rapidly spreading LTE. Despite its advantages in electrical equalization and digital signal processing (DSP), OFDM have recently been significantly considered for optical communications [2]. Presently, wavelength division multiplexing (WDM), and time division multiplexing (TDM) are the leading multiplexing approaches for building up a high speed optical communication system up to hundreds or thousands of Gigabits/s over a single channel [3]. Differs from WDM and TDM which are based on single carrier modulation, OFDM offers a limit-approaching spectral efficiency and theoretically it can achieve the maximum capacity of a channel. OFDM also has the advantage of high resistance to linear dispersion.

Fig. 3.1 shows the comparison between WDM/FDM and OFDM [2]. As it is illustrated in the left spectrum, WDM/FDM has the sub-carriers separated by guard bands to prevent the spectrum overlapping between the adjacent sub-carriers (wavelengths) and thus to prevent the channel crosstalk. Compared to WDM/FDM, OFDM has multiple sub-carriers but no guard band between them.

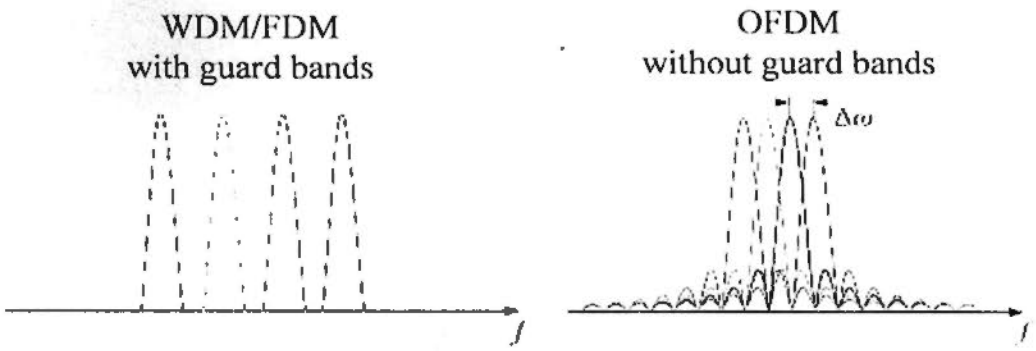

Fig. 3.1 Comparison of the spectrum between WDM/FDM and OFDM.

Consider a multi-carrier signal (super-channel) with N sub-carriers, the frequency spacing between adjacent sub-carriers will be $\Delta f=1/T$, in which T is the symbol duration. The illustration of OFDM signal in frequency and time domain are both shown in Fig. 3.2. One can notice that, at the frequency of one sub-carrier, the power of all other sub-carriers is zero. The temporal waveforms of the sub-carriers indicate a maintained frequency relationship which results in the orthogonality and thus allows the overlapping of their spectra after modulation.

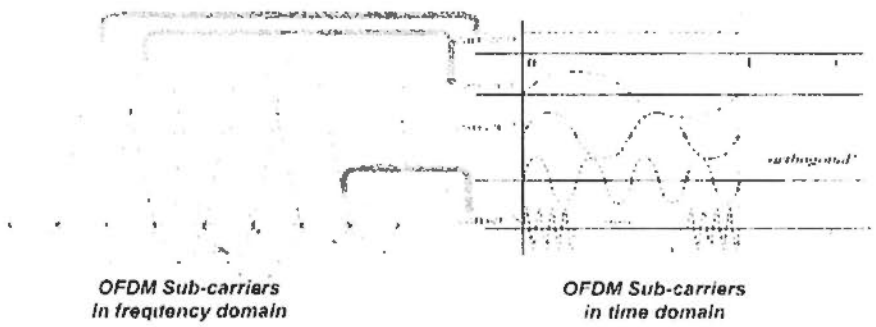

Fig. 3.2 Frequency and time domain illustrations of the multi-carrier OFDM [5].

The content of this chapter is organized as follows. In Section 3.1, optical OFDM will be introduced. In Section 3.2, we introduce the optical OFDM DEMUX.

Utilizing cascaded and multi-section Sagnac interferometers, the optical DEMUX of OFDM signals is studied and discussed in Section 3.3.

3.1 Optical OFDM

The speeds of the OFDM related DSP implementation techniques have been boost to Gigahertz, enabling the widely eye-catching applications of OFDM for long haul optical transmission and short distance optical access. However, those techniques themselves do not overcome the bottleneck of electronics which limits the speed when OFDM is applied for optical communication [6].

The up-to-date solutions of optical OFDM generation can be classified into the electrical approach based on DSP and optical approach based on optical comb [3], which is going to be introduced in Section 3.1.1 and Section 3.1.2.

3.1.1 DSP based Optical OFDM Generation

The electrical approach for OFDM generation has all mapping, inverse fast Fourier transform (IFFT) and digital to analog conversion (DAC) processed by electronics, which offers advantages of easily electrical equalization and flexibly digital signal processing (DSP) [7-9]. However, due to the electronic bottleneck, electrical OFDM signal usually has limited speed and it must be combined with advanced modulation and extra multiplexing techniques in order to increase the speed of optical OFDM signal [10-12]. And the system is usually comparably costly.

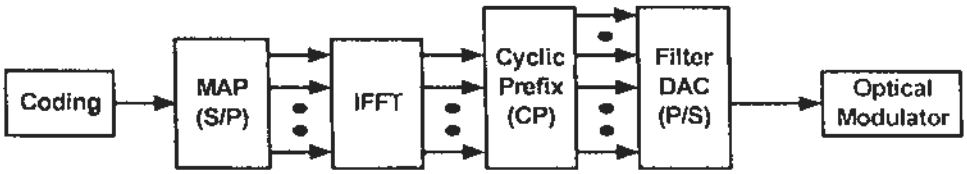

Fig. 3.3 Transmitter of the electrical approach for optical OFDM communication.

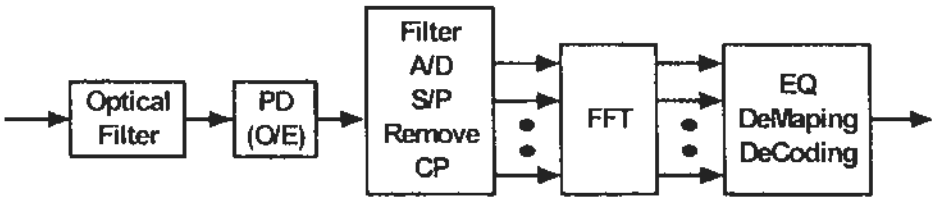

Fig. 3.4 Receiver of the electrical approach for optical OFDM communication

Fig. 3.3 and Fig. 3.4 illustrate the transmitter and receiver of the electrical approach for optical OFDM communication. All the processing stages before optical modulation are implemented electronically, as well as the reverse processing steps after the optical transmission. Therefore, the speed and capability of the off-line DSP are essentially important to the OFDM system performance. The off-line electrical processing limits the speed but also provide easier and more flexible DSP for equalization, compensation and error correction.

At the transmitter in Fig. 3.3, OFDM is realized by a digital signal processor (DSP) using serial-to-parallel conversion followed with inverse fast Fourier transformation (iFFT) and subsequent digital-to-analog conversion. Then the analog electrical OFDM signal is transferred onto an optical carrier by electric-optic modulation. The modulation format could be OOK, PSK, and QAM, depends on the request of direct detection or coherent detection.

At the receiver in Fig. 3.4, the optical signal after an optical filter will firstly has its optical field reconstructed by Optical-Electrical conversion, e.g., by coherent

detection. Then, the reverse signal processing is applied to recover the original data from the reconstructed electrical OFDM signal. Electrical equalization, compensation and error correction can be implemented accordingly.

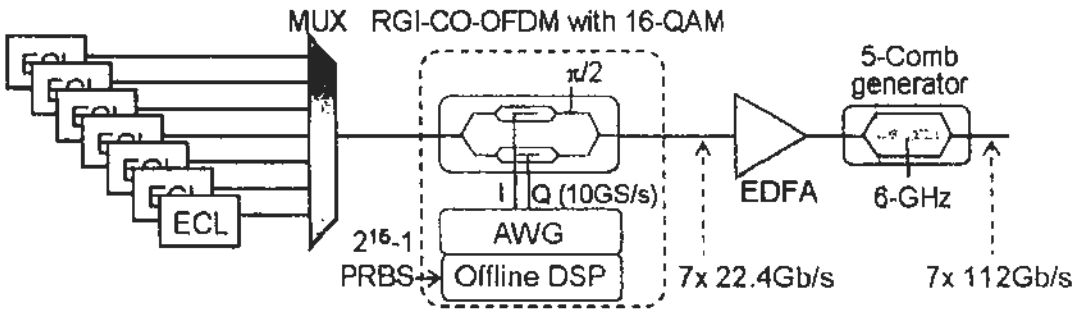

Fig. 3.5 Schematic illustration of a WDM-OFDM transmitter [13].

As previously mentioned, the limited speed of electronics for DSP only allows the generation of electrical OFDM signals up to several Gigabits. In order to increase the speed, one can combine WDM together with OFDM. A typical transmitter has been shown in Fig. 3.5, which has been applied to optical OFDM generation in several works by X. Liu *et. al.* [13-16]. At the transmitter, seven 50-GHz spaced external-cavity lasers (ECLs) each having 100-kHz linewidth serve as the WDM light source and they were combined by a wavelength-division multiplexer (MUX) before being modulated by an I/Q modulator to form seven 22.4-Gb/s CO-OFDM channels. The generation of the electrical OFDM is based on the offline DSP, a data stream consisting of a pseudo-random bit sequence (PRBS) is transformed to generate an OFDM waveform, which was then stored in an arbitrary waveform generator (AWG) equipped with two 10-GS/s digital-to-analog converters (DACs). The 5-Comb generator driving by a 6-GHz sinusoidal wave can further increase the data rates with a factor of five, and thus 112 Gb/s OFDM signal can be obtained for each channel. This 5-Comb generation process can be

understood as a 5-channel WDM process without guard intervals and thus their spectra also overlap with each other. The 7 X 112 Gb/s CO-OFDM signal is shown in Fig. 3.6 with the spectrum and the constellation diagram.

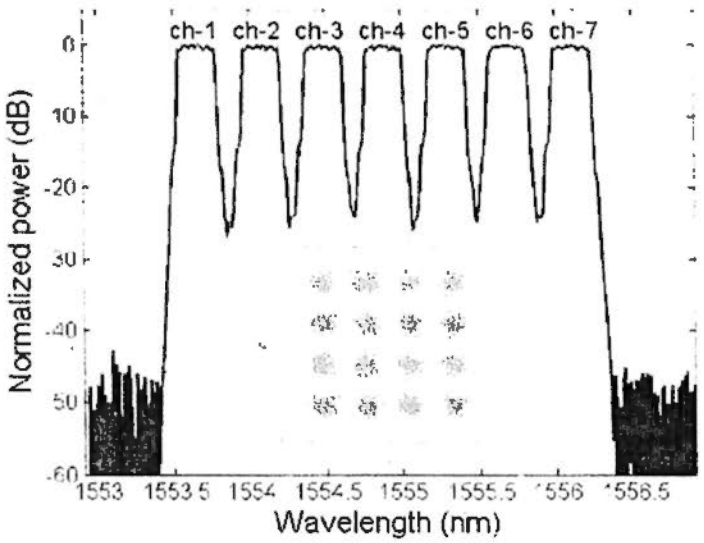

Fig. 3.6 Spectrum and constellation diagram of the 7X112 Gb/s CO-OFDM [15].

3.1.2 Optical Comb based Optical OFDM Generation

The optical approach of OFDM generation is based on multi-carrier modulation, in which a high quality optical comb source is requested [3]. The optical comb serves as the multi-carrier source with maintained orthogonality and coherence for the sub-carriers. Therefore, sometimes, it is also mentioned as coherent WDM (not necessarily using coherent detection), rather than optical OFDM [17, 18]. OFDM has the tightest spectrum because the spectra of the neighboring channels can overlap with each other due to the sub-carrier orthogonality, which results in a zero power for all the other sub-carriers at the center frequency of the N_{th} sub-carrier [5]. The interference effects due to spectral overlapping will be distributed in the same way from one bit slot to another, and that the relative optical phases can be aligned

to either increase or decrease the eye opening [17]. Thus, one can control the inter channel interference by individually control the phase of each carriers [17].

Since WDM has guard bands between each neighboring channels, wideband multiplexing can be achieved covering the whole C-band, S-band and L-band. Hundreds of densely multiplexed channels can be obtained by WDM [19-21]. However, it is difficult to achieve wideband multi-carrier modulation for OFDM. The difficulty comes from the request of optical comb and the processing. A wideband optical comb source is difficult to be obtained with high extinction ratio, high carrier power and good coherence, which are highly desired quality for OFDM. On the other hand, wideband multiplexing and DEMUX of optical OFDM signals are also difficult. The increase of the number of sub-carrier will lead to the increase of the complexity in the OFDM transmitter and receiver. Therefore, super-channel is desired as shown in Fig. 3.7 [22-24].

A super-channel based optical OFDM signal consists of a small number of sub-carriers, e.g. 10 carriers each carrying 100-Gb/s data and building up a 1-Tb/s OFDM super-channel as shown in Fig. 3.7. To further increase the data traffic while maintaining the complexity in the transmitter and receiver, one can use wavelength division multiplexing to combine multiple super-channels together.

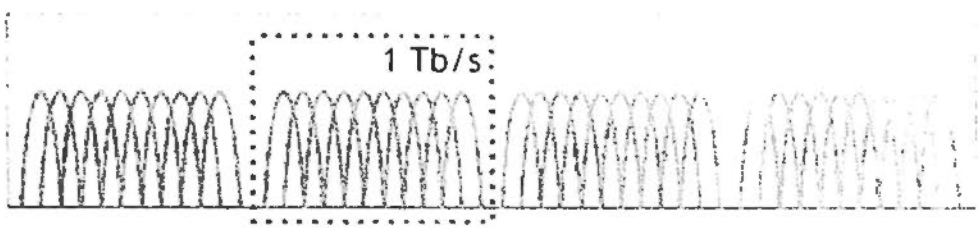

Fig. 3.7 Schematic illustration of the OFDM super-channel with channel multiplexing by WDM for terabit optical signal generation [23].

The generation of a super-channel OFDM signal can be achieved based on electrical approach by DSP and also optical approach by optical comb. Fig. 3.8 shows the schematic illustration of an optical approach utilized in Ref. 24, which indicates the idea of all-optical generation of OFDM based on optical comb. The difference between the electrical approach and optical approach is the multi-carrier modulation, whether it is based on DSP or optical comb.

In Fig. 3.8, a CW laser generates a carrier with narrow line width, which ensures the coherence and stability. A multi-carrier generator after the laser enables us to obtain an optical comb source with multiple sub-carriers, each of which has a dedicated frequency so that the frequency spacing is fixed, resulting in the orthogonality. A demultiplexer (DMUX) splits the carriers and each of carriers are directed into an I/Q modulator for optical modulation separately. Recombining the modulated carriers together forms the optical OFDM signal, the super-channel.

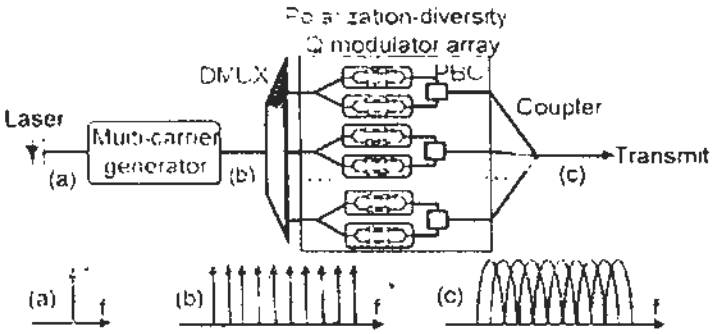

Fig. 3.8 All-optical OFDM generation based on optical comb for terabit optical OFDM super-channel [24].

Usually, a frequency interleaver will be utilized instead of DMUX. The interleaver splits the carriers into two branches, the even numbered carriers and the odd numbered carriers. The even and odd carriers are separately modulated in the

two branches and optical OFDM signal is obtained by recombining them together after the modulation [25].

3.2 Optical OFDM DEMUX

The optical comb based OFDM generation enables single-carrier modulation bit-rate operates at a very high speed, e.g. 54 Gb/s for each carrier [26], which requires the optical processing at the receiver. One of the unavoidable processing steps is the optical DEMUX for optical OFDM signals [26, 27]. Usually, it is called the optical FFT process.

Fig. 3.9 shows the optical implementation of the circuit for 4-channel optical OFDM DEMUX. Serial-to-parallel (S/P) conversion is the first stage, after which is the stage of sampling using optical gate for each channel. The FFT circuit is fundamentally based on optical interference and thus decodes the data for detection (coherent detection or direct detection).

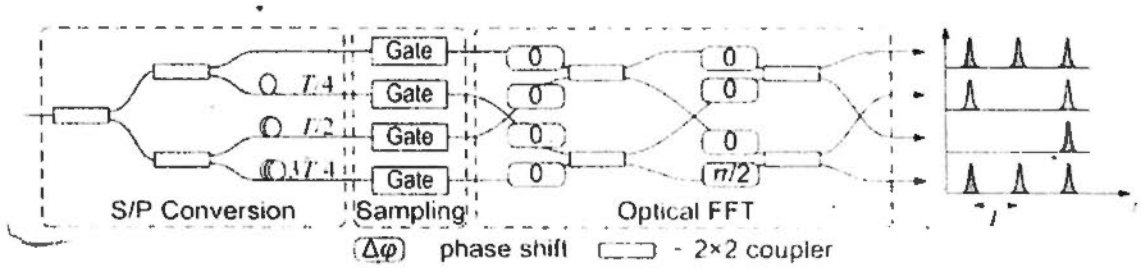

Fig. 3.9 Optical FFT configuration for OFDM DEMUX [27].

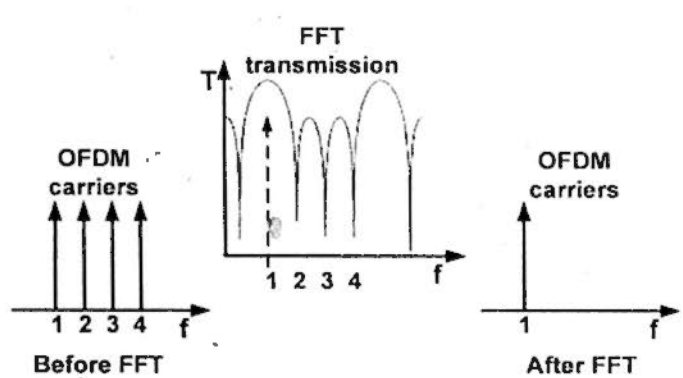

Fig. 3.10 Optical FFT transmission process with matched filtering by cascaded delay interference for OFDM sub-carrier DEMUX [27].

Variants of FFT circuits have been demonstrated, such as all-fiber configurations as presented in Ref. 27. The one that has been frequently used is cascaded delay interferometer configuration, which would have a typical transmission spectrum as shown in Fig. 3.10.

Compared with DSP for FFT, optical FFT has the overwhelming advantage of processing speed. The optical sampling window using EOM or EAM could be much shorter than electronic sampling windows of analog-to-digital converters (ADC) [28]. Particularly, by using nonlinear signal processing techniques in HNLF or SOA, shorter sampling window smaller than picoseconds can be achieved too. The power consumption of optical FFT is minimal. The optical FFT circuits themselves consume no power apart from the insertion loss [27].

3.3 Cascaded and Multi-section Sagnac Interferometers for Optical OFDM DEMUX

Sagnac interferometer is one of the most important interferometers, which has widely been used in a lot of areas, including optical fiber communication, optical sensing and navigation [29]. For navigation, one of the most notable examples of Sagnac interferometer is the configuration of gyroscope, which is actually one kind of angular velocity sensing. Among all the configurations of Sagnac interferometers, birefringent fiber based Sagnac interferometer (BF-SI) is the most famous and also the most widely using one, which is also called birefringent fiber loop mirror, or hi-bi fiber loop mirror [30].

In optical sensing, BF-SI can do all-fiber and all-optical sensing for strain, temperature, bending, liquid level, displacement, and so on [31-33]. In optical communications, BF-SI can be directly used as optical filters, interleaver, and wavelength division multiplexer. With a BF-SI included inside the laser cavity, multi-wavelength laser can be constructed due to the comb filtering [34, 35]. Based on the intrinsic delay interference, BF-SI can also be used for DPSK demodulation and pulse format conversions [36].

Particularly, with reduced implementation complexity, BF-SI can also be used for constructing an optical FFT circuit, meaning a cascaded delay interferometer, which can be used for optical OFDM DEMUX. In this part of the thesis work, we are going to study the transmission properties of cascaded and multi-section BF-SIs. The objective is to design optical FFT circuit for all-optical OFDM DEMUX.

3.3.1 Cascaded and Multi-section BF-SI

Generally, BF-SI is constructed by splicing a section of birefringent fiber (BF) to the output ports of a 3-dB fiber coupler to build up a fiber loop mirror, as shown in Fig. 3.11. Inside the loop mirror, the two counter propagating waves travel with identical optical paths but in different polarization directions with respect to BF's main axis. Thus, a relative delay is introduced, resulting in the periodic loss spectrum (the comb filtering spectrum). The operation of one-section BF-SI has been well studied theoretically and experimentally in the literature.

We can also construct variant BF-SIs with multi-section BFs inside one single loop mirror as shown in Fig. 1(b) and (c). Consider $\theta(i+1)$ as angle between the main axis of BF-i and BF-(i+1), therefore, $\theta 1$ and $\theta(n+1)$ would be the angle of input light polarization with respect to the main axis of BF-1 and BF-(n),

respectively. For the situation with one section BF (i = 1), we can have the transmission function of the BF-SI given by

$$T = \left[\sin(\theta_1 + \theta_2)\cos\frac{\beta_1}{2}\right]^2 - \left[\cos\frac{\beta_1}{2}\right]^2, \theta_1 + \theta_2 = \frac{\pi}{2} \qquad \text{(Eq.3.1)}$$

where, $\beta_i = 2\pi n_i L_i / \lambda$, n_i and L_i is the birefringence and fiber length of the i_{th} section BF. The transmission spectrum for one-section BF-SI is simply a comb filtering spectrum. With $\theta_1 + \theta_2 = \pi/2$, meaning an orthogonal polarization direction between the two counter propagating waves in the BF, the transmission of the interferometer has the largest ER and smallest insertion loss. Particularly, the transmission would only response to wavelength rather than the polarization of the input light, offering polarization independent operations.

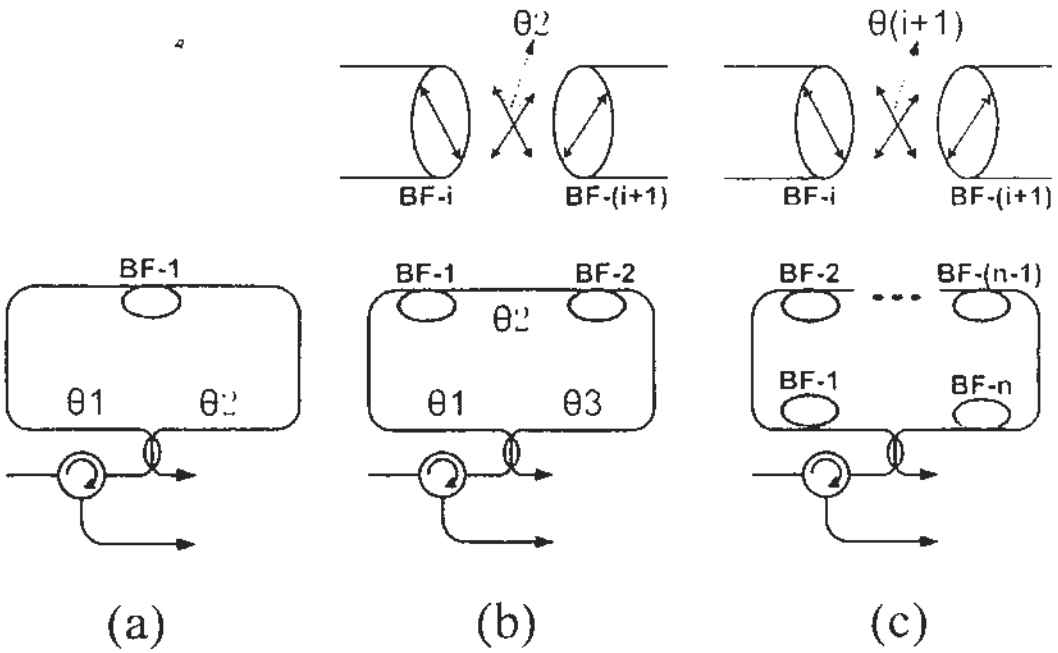

Fig. 3.11 Variant Sagnac interferometers with multi-section BFs inside the loop mirror.

With two different one-section BF-SIs cascaded together, both of them are under the situation with the largest ER and the smallest insertion loss, the total transmission function would be

$$T = \left[\cos\frac{\beta_1}{2}\cos\frac{\beta_2}{2}\right]^2 \qquad \text{(Eq.3.2)}$$

Similarly, we can also derive the transmission functions for three (or more) BF-SIs cascaded together, under the situation with the largest ER and the smallest insertion loss for all of them.

$$T = \left[\cos\frac{\beta_1}{2}\cos\frac{\beta_2}{2}\cos\frac{\beta_3}{2}\right]^2 \qquad \text{(Eq.3.3)}$$

$$T = \left[\cos\frac{\beta_1}{2}\cos\frac{\beta_2}{2}\cos\frac{\beta_3}{2}\bullet\bullet\bullet\cos\frac{\beta_n}{2}\right]^2 \ (n = 1, 2, \ldots n) \qquad \text{(Eq.3.4)}$$

If we consider a BF-SI with multi-section BFs, for example, two sections of BFs with different fiber lengths in the fiber loop, the transmission function will be modified as

$$T = \left[\cos\frac{\beta_1+\beta_2}{2}\sin(\theta_1+\theta_3)\cos\theta_3 + \cos\frac{\beta_1-\beta_2}{2}\cos(\theta_1+\theta_3)\sin\theta_3\right]^2 \qquad \text{(Eq.3.5)}$$

Suppose $\theta_1+\theta_3=\theta_2=\pi/4$, we can find that the transmission function can be written as:

$$T = \frac{1}{4}\left[\cos\frac{\beta_1+\beta_2}{2}+\cos\frac{\beta_1-\beta_2}{2}\right]^2 = \left[\cos\frac{\beta_1}{2}\cos\frac{\beta_2}{2}\right]^2 \ (\theta_1+\theta_3=\theta_2=\frac{\pi}{4}) \qquad \text{(Eq.3.6)}$$

Therefore, the transmission function of two-section BF-SI is exactly the same as that of the two cascaded one-section BF-SIs in Eq.3.2. The following

spectra in Fig. 3.12 and Fig. 3.13 show the simulated transmissions for several kinds of different BF-SIs with a same birefringence of $n=3\times10^{-4}$ for all BFs.

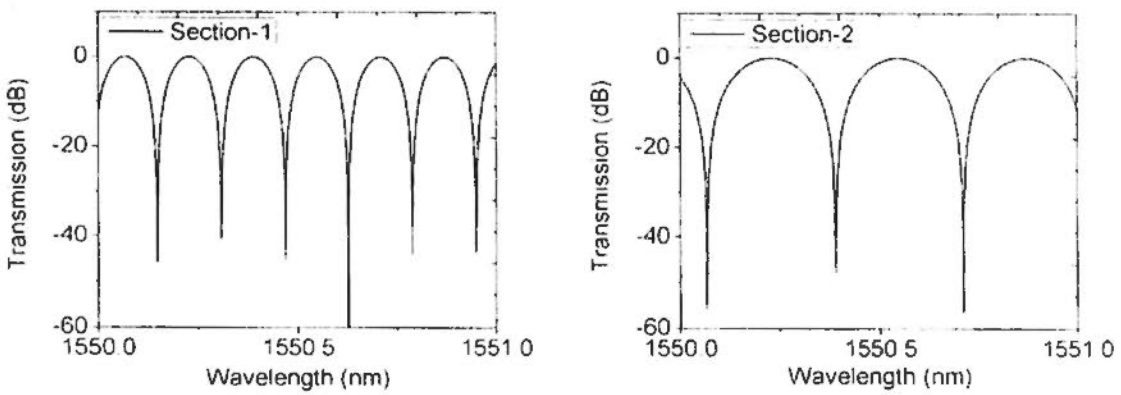

Fig. 3.12 Section-1 (a) and Section-2 (b) stand for one-section BF-SIs with difference BF length of $L_1=50.0$ m and $L_2=25.0$ m, respectively.

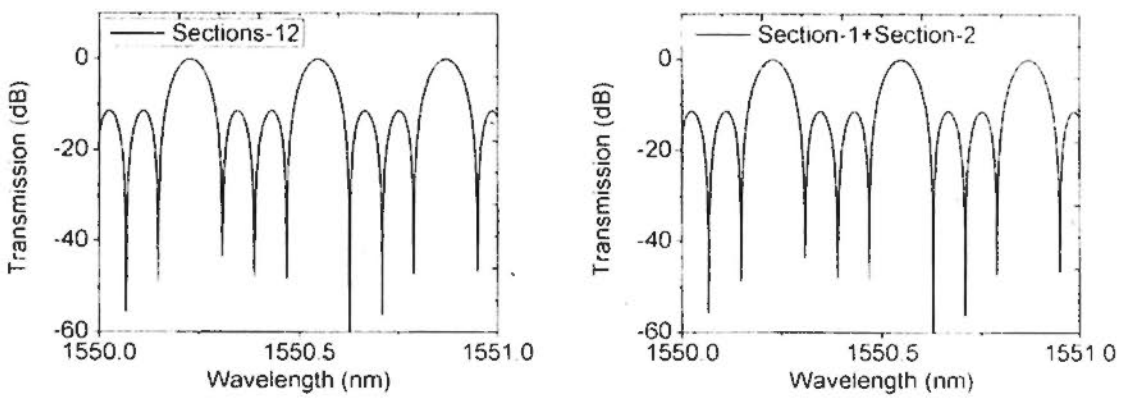

Fig. 3.13 Sections-12 (a) stands for two-section BF-SI with two BFs ($L_1=50.0$ m and $L_2=25.0$ m), $\theta_1+\theta_3=\theta_2=\pi/4$. Section-1+Section-2 (b) stands for two cascaded one-section BF-SIs with difference BF length of $L_1=50.0$ m and $L_2=25.0$ m, respectively.

For three-section BF-SI, the transmission function is:

$$T=\left[A_1+A_2+A_3+A_4\right]^2 \qquad \text{(Eq.3.7)}$$

$$
\begin{aligned}
A_1 &= \cos\frac{\beta_1+\beta_2+\beta_3}{2}\sin(\theta_1+\theta_4)\cos\theta_2\cos\theta_3 \\
A_2 &= \cos\frac{-\beta_1+\beta_2+\beta_3}{2}\cos(\theta_1+\theta_4)\sin\theta_2\cos\theta_3 \\
A_3 &= \cos\frac{\beta_1+\beta_2-\beta_3}{2}\cos(\theta_1+\theta_4)\cos\theta_2\sin\theta_3 \\
A_4 &= -\cos\frac{\beta_1-\beta_2-\beta_3}{2}\sin(\theta_1+\theta_4)\sin\theta_2\cos\theta_3
\end{aligned}
\qquad \text{(Eq.3.8)}
$$

For comparison, we can also derive the expression of three cascaded BF-SIs in another form:

$$
\begin{aligned}
T = \Bigg[\frac{1}{4}\Bigg(&\cos\frac{\beta_1+\beta_2+\beta_3}{2}+\cos\frac{\beta_1+\beta_2-\beta_3}{2} \\
&+\cos\frac{\beta_1-\beta_2+\beta_3}{2}+\cos\frac{\beta_1-\beta_2-\beta_3}{2}\Bigg)\Bigg]^2
\end{aligned}
\qquad \text{(Eq.3.9)}
$$

Unlike the previous two-section BF-SI, it is impossible for three-section BF-SI to have a same transmission function as the three cascaded BF-SIs, even with $\theta_1+\theta_4=\theta_2=\theta_3=\pi/4$. Their different transmission spectra are shown in Fig. 3.14.

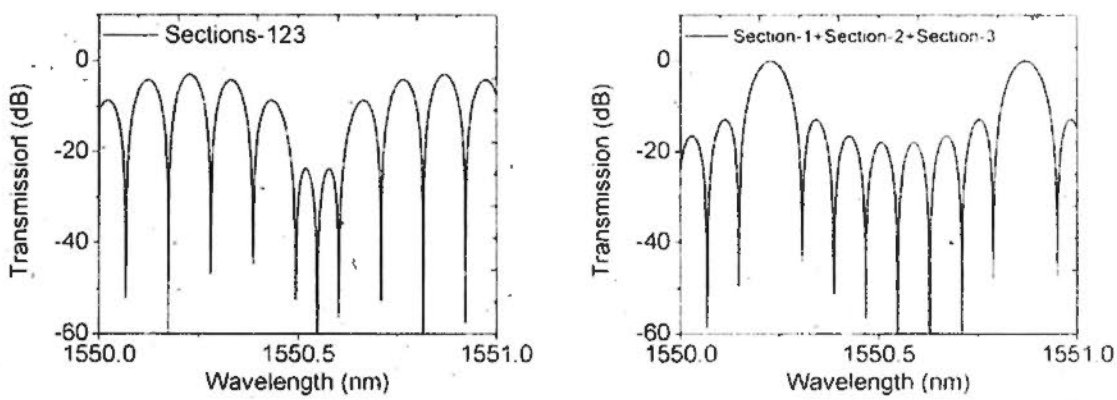

Fig. 3.14 Sections-123 stands for three-section BF-SI with three different BFs (L_1=50.0 m, L_2=25.0 m, and L_2=12.5 m), $\theta_1+\theta_4=\theta_2=\theta_3=\pi/4$. Section-1+Section-2+Section-3 stands for three cascaded one-section Sagnac interferometers with difference BF length of L_1=50.0 m, L_2=25.0 m, and L_3=12.5 m, respectively.

From Fig. 3.13, we can find that the spectrum of Sections-12 is exactly the same as Section-1+Sections-2, as proved by Eq.3.2 and Eq.3.6. Meanwhile, the spectra for Section-1+Section-2+section-3 and Sections-123 are totally different, which also verifies our conclusions from Eq.3.7, Eq.3.8, and Eq.3.9. However, by cascading one single-section Sagnac interferometer with another two-section Sagnac interferometer, such as Section-1+Sections-23 and Section-12+Sections-3, we can also obtain the same transmission spectra as three cascaded Sagnac interferometers (Section-1+Section-2+Section-3), as shown in Fig. 3.15.

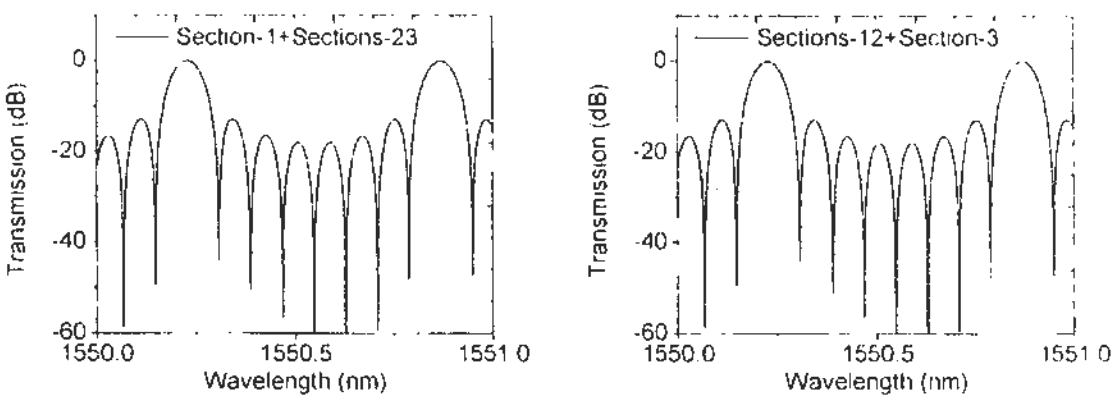

(a) (b)

Fig. 3.15 Spectra of cascaded one-section and two-section Sagnac interferometers.

3.3.2 BF-SIs Designed for Optical OFDM DEMUX

The principle of optical OFDM DEMUX is based on the optical FFT process. The cascaded delay interferometers can be taken as one typical optical FFT circuit, in which, the relative delay for each stage is half of that for the previous stage [27]. As for Sagnac interferometer, the half relative delay means half of the BF fiber length. Therefore, it is very simple to construct such an all-fiber delay interferometer with cascaded or multi-section BF-SIs.

Based on planar lightwave circuit (PLC) [37-40], fiber-coupler based delay interferometer [25, 27], fiber grating [41, 42], and arrayed waveguide grating (AWG) [43, 44], there have been demonstrations of optical OFDM DEMUX up to 10 channels. Usually, at a typical base rate of 10 GHz, an 8-channel demultiplexer together with an extra optical bandpass filter is enough for optical DEMUX of OFDM signals with over 8 subchannels. In this work, we will only look into 4-channel and 8-channel demultiplexers for 10-GHz baseband signals.

The configurations of 4-channel OFDM demultiplexers are shown in Fig. 3.16: two-section Sagnac interferometer and two cascaded Sagnac interferometers, which have the same transmission function as indicated in Fig. 3.13. The angles in Eq.3.6 can be adjusted using polarization controllers (PC) inside the loop mirrors. All BFs have the same birefringence of $\Delta n=3\times10^{-4}$, but different fiber lengths: L_1=50.0 m, L_2=25.0 m, and L_3=12.5 m for BF-1, BF-2 and BF-3, respectively. For 8-carrier OFDM DEMUX, we can use either one configuration of the following ones, which have the same transmission function: Section-1+Section-2+Section-3, Section-1+Sections-23, Section-2+Sections-13 and Section-3+Sections-12. Shown in Fig. 3.17 are the configurations of Section-1+Section-2+Section-3 and Section-1+Sections-23.

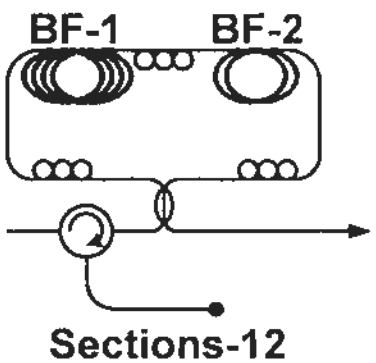

(a)

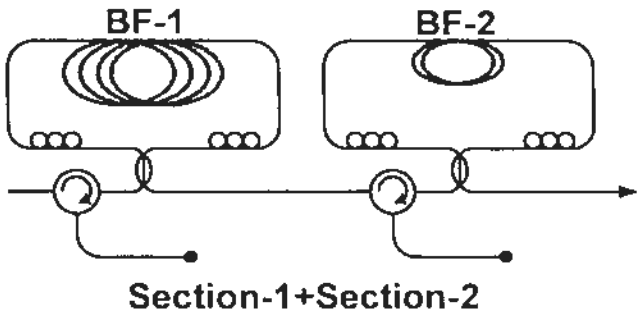

(b)

Fig. 3.16 Configurations of the 4-channel OFDM demultiplexers: (a) two-section Sagnac interferometer; (b) two cascaded Sagnac interferometers.

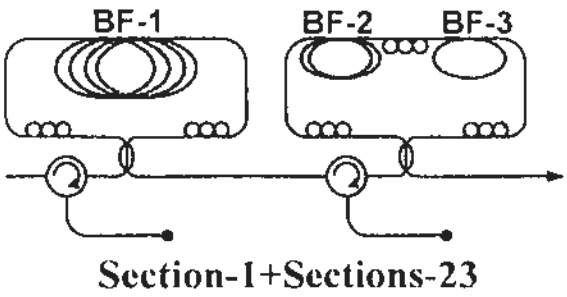

(a)

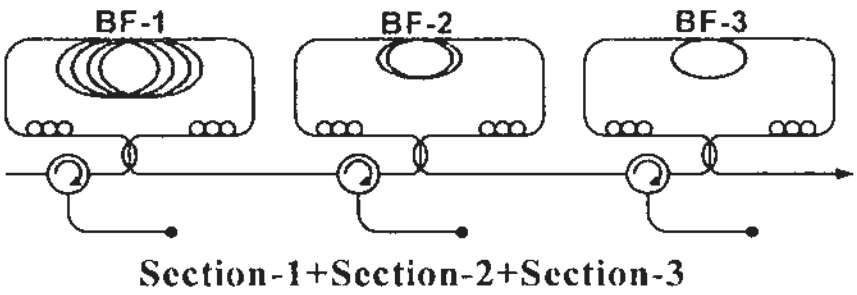

(b)

Fig. 3.17 Configurations of the 8-channel OFDM demultiplexers: (a) one-section Sagnac interferometer cascaded with another two-section Sagnac interferometer; (b) three cascaded Sagnac interferometers.

Thermally or mechanically, the transmission of Sagnac interferometers can be tuned, which is widely used in optical sensing [33, 34]. Here for OFDM

DEMUX, we need to shift the transmission spectrum in order to select different carriers for tunable DEMUX. There are several ways to adjust the transmission spectrum, thermally, mechanically, or electrically. Since common birefringent fiber is sensitive to temperature, temperature tuning is efficient and convenient. Bending and stretching are also effective, which can be realized using Cantilever or PZT. With a common phase modulator, electrical tuning of the phase shift can also be obtained [35].

Considering phase changes of $\Delta\varphi_i$ can be introduced to different birefringent fibers due to temperature change or bending, we can shift the spectrum with different phase change combinations. In order to achieve the DEMUX of *channel-n*, the required phase change $\Delta\varphi_i$ for BF-i should be:

$$\Delta\varphi_i = \frac{2\pi(n-1)}{2^i} \qquad \text{(Eq.3.10)}$$

For 4-channel DEMUX with configurations as shown in Fig. 3.16, we can obtain tunable DEMUX for all channels (from channel-1 to channel-4) with different phase changes for BF-1 and BF-2. Table 3.1 shows the phase change combinations corresponds to the spectra in Fig. 3.18.

Table 3.1 Phase changes of the BFs for tunable 4-channel OFDM DEMUX

$\Delta\varphi_1$ (BF-1)	$\Delta\varphi_2$ (BF-2)	DEMUX channel-n
(n-1)×π	(n-1)×π/2	n=1, 2, 3, 4
0	0	n=1
π	π/2	n=2
0	π	n=3
π	3π/2	n=4

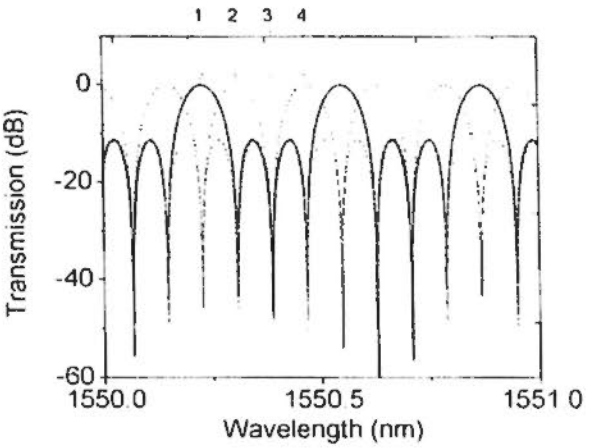

Fig. 3.18 Transmission spectra of a 4-channel OFDM demultiplexer.

We can also derive the required phase changes of different BFs for 8-carrier OFDM DEMUX, as shown in Table 3.2 and Fig. 3.19. For 8-channel OFDM DEMUX, we can use any one of the following configurations, which have the same transmission: Section-1+Section-2+Section-3, Section-1+Sections-23, Section-2+Sections-13 and Section-3+Sections-12.

Table 3.2 Phase changes of the BFs for tunable 8-channel OFDM DEMUX

$\Delta\varphi_1$ (BF-1)	$\Delta\varphi_2$ (BF-2)	$\Delta\varphi_3$ (BF-3)	DEMUX channel-n
(n-1)×π	(n-1)×π/2	(n-1)×π/4	n=1, 2,...8
0	0	0	n=1
π	π/2	π/4	n=2
0	π	π/2	n=3
π	3π/2	3π/4	n=4
0	2π=0	π	n=5
π	5π/2= π/2	5π/4	n=6
0	6π/2= π	3π/2	n=7
π	7π/2= 3π/2	7π/4	n=8

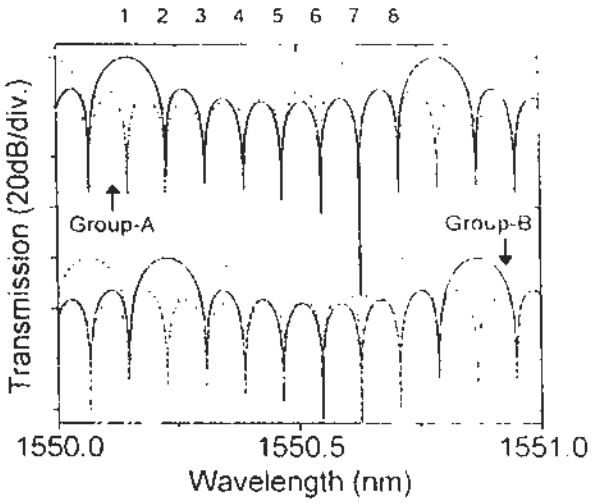

Fig.3.19 Transmission spectra of an 8-channel OFDM demultiplexer.

Full DEMUX configurations for 4-channel and 8-channel OFDM DEMUX are shown in Fig. 3.20 and Fig. 3.21. For each demultiplexed channels, there is a gate for sampling after each the FFT process. The gate should have a narrow switching window for the sampling. One can simply use an EAM or an EOM as the gate, based on the electric-optic modulation. Meanwhile, it is foreseeable that all-optical processing technologies based on nonlinear effects can also be applied to this gating function for OFDM DEMUX. Narrow gating window at picoseconds scale enables the fast gating for OFDM signals with large number of carriers.

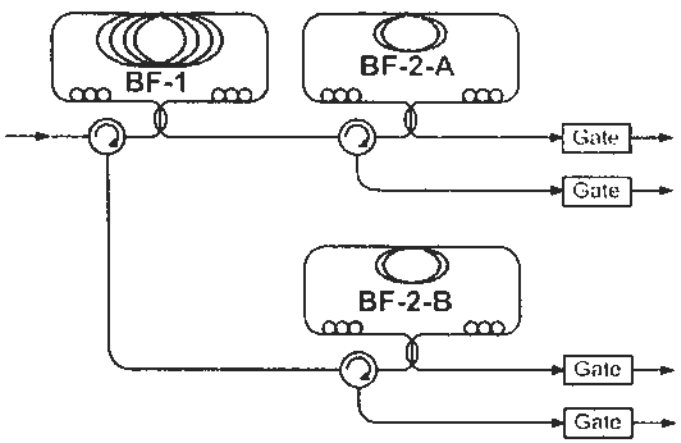

Fig. 3.20 Full DEMUX configuration for 4-channel OFDM signals.

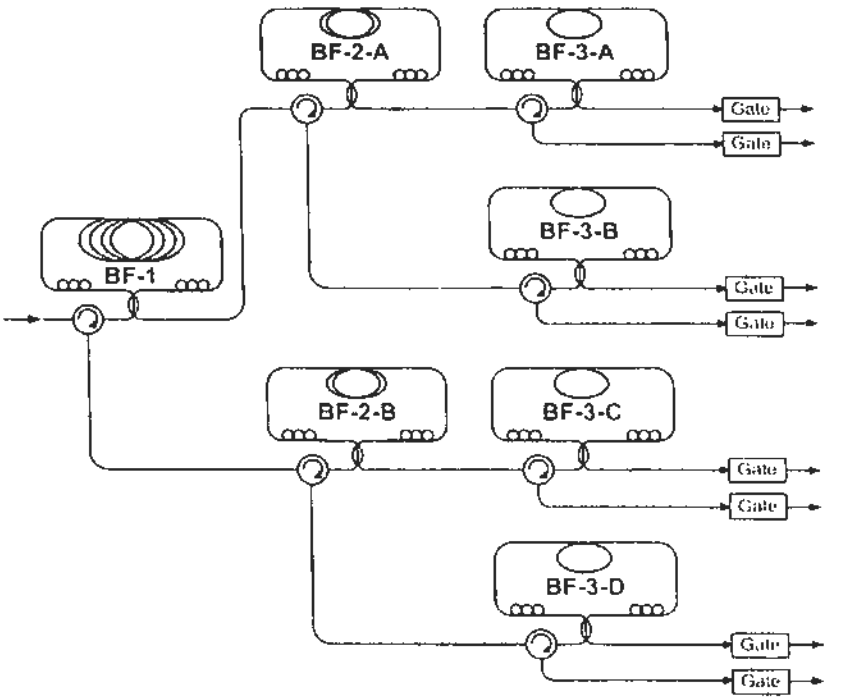

Fig. 3.21 Full DEMUX configuration for 8-channel OFDM signals.

3.3.3 Experimental Results

The BFs in the experiment have a birefringence of $\Delta n=3\times10^{-4}$. Three sections of BFs have been utilized with different fiber lengths: L_1 50.0 m, L_2=25.0 m, and L_3=12.5 m for BF-1, BF-2 and BF-3, respectively. BF-SIs with different configurations, as demonstrated in Section 3.2.2, have been constructed. Their transmissions have been measured using an EDFA as a wideband ASE source.

Fig. 3.22 shows the experimental transmission spectra of two-section BF-SIs, which is in agreement with our simulation results in Fig. 3.13 and Fig. 3.15. The two-section BF-SI is constructed with BF-1 and BF-2, which suits the 4-channel optical OFDM DEMUX for 10-Gb/s base band signals as shown in Fig. 3.22(a). The 8-channel optical OFDM demultiplexers utilize three BFs with different configurations but same transmissions as shown in Fig. 3.22(b) and Fig. 3.22(c).

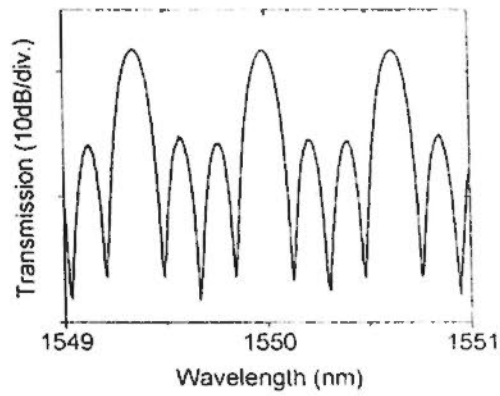

(a)

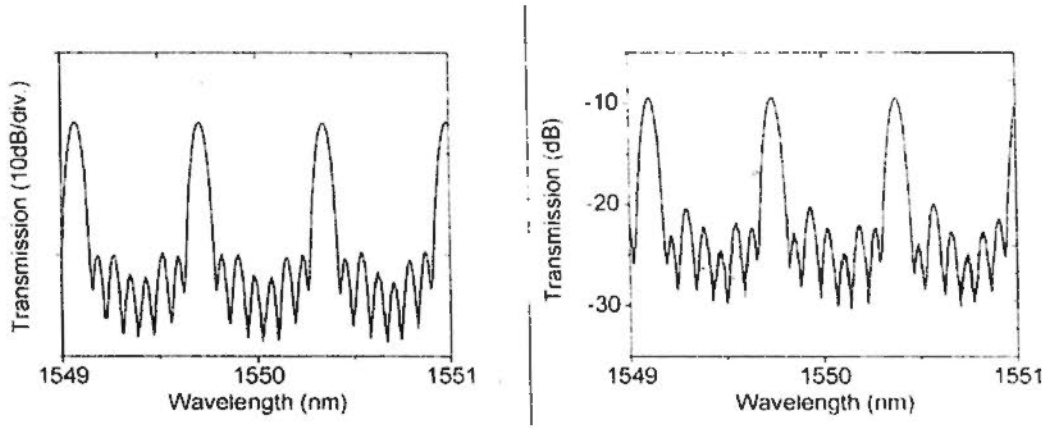

(b) (c)

Fig. 3.22 Experimental transmission spectra of the designed Sagnac interferometers for 4-channel and 8-channel optical OFDM DEMUX: (a) Sections-12; (b) Senction-1+Sections-23; (c) Senctions-12+Section-3.

Fig. 3.23 shows the experimental setup. The tunable laser generates a CW wavelength which is phase modulated at 10.53 GHz. With a depth modulation (high drive voltage), we can obtain a chirped modulation and generates multiple sub-carriers. 5 sub-carriers can be obtained after the phase modulator at a modulation index of 2π (the phase modulator has a V_π of ~5V). The interleaver split the combs into two branches (even channels and odd channels) and separately modulated with 10.53 Gb/s PRBS signals.

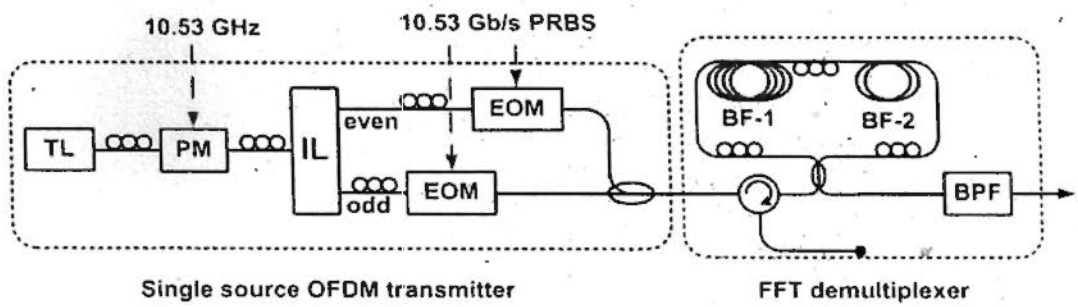

Fig. 3.23 Experimental setup of the single source OFDM transmitter and demultiplexer. TL: tunable laser; PM: phase modulator; IL: interleaver; EOM: electric-optic modulator; BPF: bandpass filter.

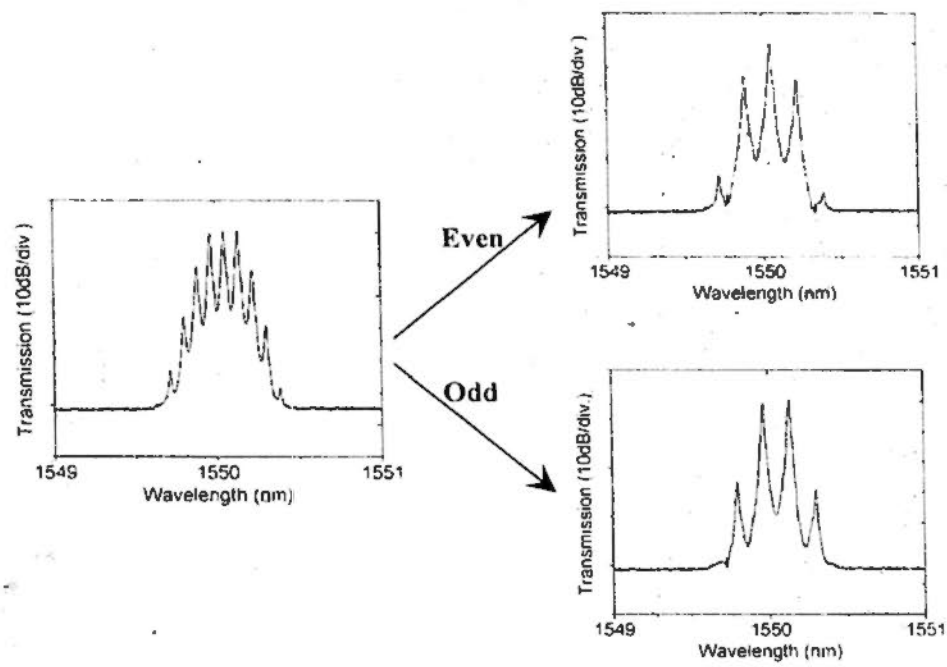

Fig. 3.24 Spectra before (left) and after interleaving(right) for separating the Even and Odd sub-carriers.

The NRZ-OOK signal spectra of the Even channels and Odd channels are shown in Fig. 3.24. By combining the two branches together, we obtain the 5-channel OFDM signal which is also shown in Fig. 3.25. The eye diagram is shown in Fig. 3.26, in which a closed eye is obtained indicating the analog waveform of the optical OFDM signal.

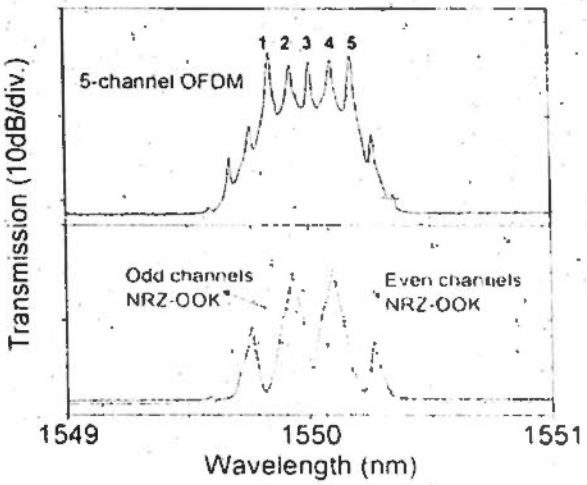

Fig. 3.25 Spectra of the modulated Even and Odd channels (lower) and the 5-channel OFDM signal (upper).

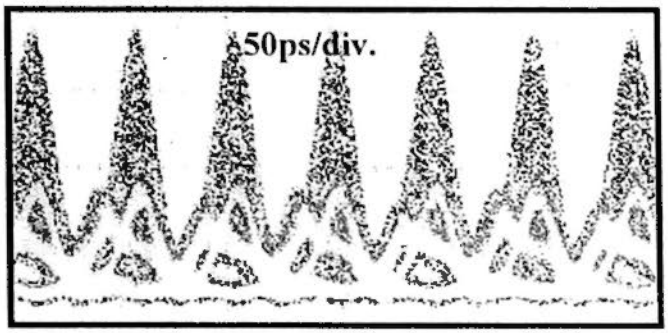

Fig. 3.26 Eye diagram of the 5-channel optical OFDM signal.

By using the designed multi-section BF-SIs, we performed the optical OFDM DEMUX. The two-section Sagnac interferometer is for 4-channel OFDM DEMUX. However, by using an extra band pass filter after the demultiplexer, we can also do 5-channel DEMUX. By simply bending the BFs, we can achieve tunable DEMUX and the demultiplexed 5 channels are also shown in Fig. 3.27. The eye-diagram for the demultiplexed OFDM signal (channel-5) is shown in Fig. 3.28.

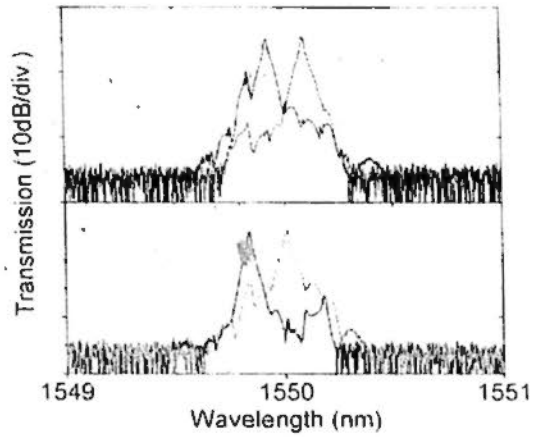

Fig. 3.27 Spectrum of the demultiplexed 5 channels using two-section BF-SI.

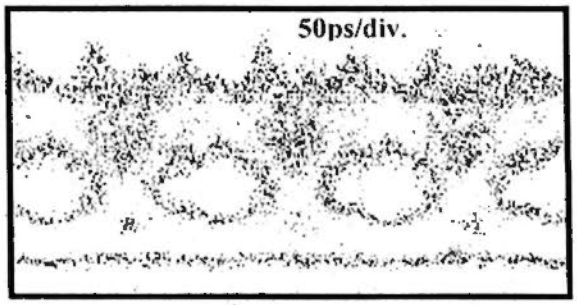

Fig. 3.28 Eye diagram of the demultiplexed Channel-5.

Due to the stability issue of the birefringent fiber, the demultiplexed signal is noisy as shown in Fig. 3.28. An extinction ratio of 6 dB and an SNR of ~3 dB are obtained without sampling. As a matter of fact, the BF-SI we are using does not precisely suit the OFDM transmitter (the frequency), which also affects the demultiplexing performance. The bit error rate has not been performed but we believe error-free DEMUX can be expected with the BF-SI precisely designed (suitable FSR) and well packaged to improve the accuricy and stability.

References

[1]. J. Armstrong, "OFDM: From copper and wireless to optical," presented at the Proc. OFC/NFOEC 2008, San Diego, CA, 2008, Tutorial, OMM1

[2]. Jean Armstrong, "OFDM for Optical Communications," J. Lightwave Technol. **27**, 189-204 (2009)

[3]. R. Freund, M. Nolle, C. Schmidt-Langhorst, R. Ludwig, C. Schubert, G. Bosco, A. Carena, P. Poggiolini, L. Oxenlowe, M. Galili, H. C. Hansen Mulvad, M. Winter, D. Hillerkuss, R. Schmogrow, W. Freude, J. Leuthold, A. D. Ellis, F. C. Garcia Gunning, J. Zhao, P. Frascella, S. K. Ibrahim, and N. Mac Suibhne, "Single-and multi-carrier techniques to build up Tb/s per channel transmission systems," in International Conference on Transparent Optical Networks (ICTON) (2010), Tu.D1.4.

[4]. Neda Cvijetic, "OFDM for Next Generation Optical Access Networks," presented at the Proc. OFC/NFOEC 2011, Los Angeles, CA, 2011, Tutorial, OMG3 (2011)

[5]. Fred Buchali, Roman Dischler, and Xiang Liu, "Optical OFDM: A Promising High-Speed Optical Transport Technology," Bell Labs Technical Journal **14**(1), 125–146 (2009)

[6]. William Shieh, Xingwen Yi, Yiran Ma, and Qi Yang, "Coherent optical OFDM: has its time come? [Invited]," J. Opt. Netw. 7, 234-255 (2008)

[7]. W. Shieh, H. Bao, and Y. Tang, "Coherent optical OFDM: theory and design," Opt. Express **16**, 841-859 (2008)

[8]. W. Shieh and C. Athaudage, "Coherent optical orthogonal frequency division multiplexing," Electron. Lett. **42**, 587-589 (2006)

[9]. X. Yi, W. Shieh, and Y. Tang, "Phase estimation for coherent optical OFDM," IEEE Photon. Technol. Lett. **19**, 919-921 (2007)

[10]. W. Shieh, X. Yi, and Y. Tang, "Transmission experiment of multi-gigabit coherent optical OFDM systems over 1000km SSMF fiber," Electron. Lett. **43**, 183-185 (2007)

[11]. A. J. Lowery, L. Du, and J. Armstrong, " Orthogonal frequency division multiplexing for adaptive dispersion compensation in long haul WDM systems", in Proc. NFOEC 2006, paper PDP39. (2006)

[12]. R. Dischler, F. Buchali, "Transmission of 1.2 Tb/s continuous waveband PDM-OFDM-FDM signal with spectral efficiency of 3.3 bit/s/Hz over 400 km of SSMF", in Proc. OFC 2009, paper PDPC2 (2009)

[13]. X. Liu and F. Buchali, "Improved Nonlinear Tolerance of 112-Gb/s PDM-OFDM in Dispersion-Uncompensated Transmission with Efficient Channel Estimation," Proc. Eur. Conf. on Optical Commun. (ECOC '08) (Brussels, Belg., 2008), paper Mo.3.E.2

[14]. X. Liu, S. Chandrasekhar, B. Zhu, P. J. Winzer, A. H. Gnauck, D. W. Peckham, "Transmission of a 448-Gb/s reduced-guard-interval CO-OFDM signal with a 60-GHz optical bandwidth over 2000 km of ULAF and five 80-GHz-grid ROADMs," Proc. OFC'10, San Diego, CA, 2010

[15]. X. Liu, S. Chandrasekhar, B. Zhu, P. J. Winzer, D. W. Peckham, "7X224-Gb/s WDM transmission of reduced-guard-interval CO-OFDM with 16-QAM subcarrier modulation on a 50-GHz Grid over 2000 km of ULAF and five ROADM passes," ECOC'10 Paper Tu.3.C. (2010)

[16]. Xiang Liu, S. Chandrasekhar, Benyuan Zhu, P. J. Winzer, Alan H. Gnauck, and David W. Peckham, "448-Gb/s Reduced-Guard-Interval CO-OFDM

Transmission Over 2000 km of Ultra-Large-Area Fiber and Five 80-GHz-Grid ROADMs," J. Lightwave Technol. **29**, 483-490 (2011)

[17]. A. D. Ellis and F. C. G. Gunning, "Spectral density enhancement using coherent WDM," IEEE Photon. Technol. Lett. **17**, 504-506 (2005)

[18]. A. D. Ellis, F. C. G. Gunning, B. Cuenot, T. C. Healy, and E. Pincemin, "Towards 1TbE using Coherent WDM," in Opto-Electronics and Communications Conference, 2008 and the 2008 Australian Conference on Optical Fibre Technology, OECC/ACOFT, (2008), pp. 1–4.

[19]. X. Zhou, J. Yu, M. F. Huang, Y. Shao, T. Wang, L. Nelson, P. D. Magill, M. Birk, P. I. Borel, D. W. Peckham, R. Lingle, "64-Tb/s (640X107-Gb/s) PDM-36QAM transmission over 320 km using both pre- and post-transmission digital equalization," Proc. OFC'10 (2010)

[20]. X. Zhou, J. Yu, M. Huang, Y. Shao, T. Wang, P. D. Magill, M. Cvijetic, L. Nelson, M. Birk, G. Zhang, S. Ten, H. B. Matthew, S. K. Mishra, "Transmission of 32-Tb/s capacity over 580 km using RZ-shaped PDM-8QAM modulation format and cascaded multimodulus blind equalization algorithm," J. Lightw. Technol. **28**, 456-464 (2010)

[21]. Xiang Zhou, Jianjun Yu, Ming-Fang Huang, Yin Shao, Ting Wang, Lynn Nelson, Peter Magill, Martin Birk, Peter I. Borel, David W. Peckham, Robert Lingle, and Benyuan Zhu, "64-Tb/s, 8 b/s/Hz, PDM-36QAM Transmission Over 320 km Using Both Pre- and Post-Transmission Digital Signal Processing," J. Lightwave Technol. **29**, 571-577 (2011)

[22]. G. Gavioli, E. Torrengo, G. Bosco, A. Carena, V. Curri, V. Miot, P. Poggiolini, M. Belmonte, F. Forghieri, C. Muzio, S. Piciaccia, A. Brinciotti, A. La Porta, C. Lezzi, S. Savory, and S. Abrate, "Investigation of the Impact

of Ultra-Narrow Carrier Spacing on the Transmission of a 10-Carrier 1Tb/s Superchannel," in Optical Fiber Communication Conference, paper OThD3, (2010)

[23]. Fred Buchali, "Technologies towards Terabit Transmission Systems," presented at the ECOC 2010, 19-23 September, 2010, Torino, Italy, Tutorial, paper We.6.C.1 (2010)

[24]. S. Chandrasekhar and Xiang Liu, "Terabit Superchannels for High Spectral Efficiency Transmission," presented at the ECOC 2010, 19-23 September, 2010, Torino, Italy, paper Tu.3.C.5, (2010)

[25]. D. Hillerkuss, T. Schellinger, R. Schmogrow, M. Winter, T. Vallaitis, R. Bonk, A. Marculescu, J. Li, M. Dreschmann, J. Meyer, S. Ben Ezra, N. Narkiss, B. Nebendahl, F. Parmigiani, P. Petropoulos, B. Resan, K. Weingarten, T. Ellermeyer, J. Lutz, M. Möller, M. Hübner, J. Becker, C. Koos, W. Freude, and J. Leuthold, "Single Source Optical OFDM Transmitter and Optical FFT Receiver Demonstrated at Line Rates of 5.4 and 10.8 Tbit/s," in Optical Fiber Communication Conference, OSA Technical Digest (CD) (Optical Society of America, 2010), paper PDPC1.

[26]. Kyusang Lee, Chan T. D. Thai, and June-Koo Kevin Rhee, "All optical discrete Fourier transform processor for 100 Gbps OFDM transmission," Opt. Express **16**, 4023-4028 (2008)

[27]. D. Hillerkuss, M. Winter, M. Teschke, A. Marculescu, J. Li, G. Sigurdsson, K. Worms, S. Ben Ezra, N. Narkiss, W. Freude, and J. Leuthold, "Simple all-optical FFT scheme enabling Tbit/s real-time signal processing," Opt. Express **18**, 9324-9340 (2010)

[28]. S. Kodama, T. Ito,„N. Watanabe, S. Kondo, H. Takeuchi, H. Ito, and T. Ishibashi, "2.3 picoseconds optical gate monolithically integrating photodiode and electroabsorption modulator," Electron. Lett. **37**(19), 1185 1186 (2001)

[29]. G. A. Pavlath and H. J. Shaw, "Birefringence and polarization effects in fiber gyroscopes," Appl. Opt. **21**, 1752-1757 (1982)

[30]. W. K. Burns and A. D. Kersey, "Fiber-optic gyroscopes with depolarized light," J. Lightwave Technol. **10**, 992-999 (1992)

[31]. E. De La Rosa, L. A. Zenteno, A. N. Starodumov, and D. Monzon, "All-fiber absolute temperature sensor using an unbalanced high-birefringence Sagnac loop," Opt. Lett. **22**, 481-483 (1997)

[32]. A. N. Starodumov, L. A. Zenteno, D. Monzon, and E. De La Rosa, "Fiber Sagnac interferometer temperature sensor," Appl. Phys. Lett. **70**, 19-21 (1997)

[33]. Y. Liu, B. Liu, X. Feng, W. Zhang, G. Zhou, S. Yuan, G. Kai, and X. Dong, "High-birefringence fiber loop mirrors and their applications as sensors," Appl. Opt. **44**, 2382-2390 (2005)

[34]. M. A. Mirza and G. Stewart, "Theory and design of a simple tunable Sagnac loop filter for multiwavelength fiber lasers," Appl. Opt. **47**, 5242-5252 (2008)

[35]. M. P. Fok, K. L. Lee, and C. Shu, , "Wavelength-switchable SOA ring laser constructed with a phase modulator loop mirror filter," IEEE Photon. Technol. Lett., **17**, 1393-1395 (2005)

[36]. C. W. Chow, and H. K. Tsang, "Polarization-independent DPSK demodulation using a birefringent fiber loop," IEEE Photon. Technol. Lett. **17**, 1313-1315 (2005)

[37]. K. Takiguchi, M. Oguma, T. Shibata, and H. Takahashi, "Demultiplexer for optical orthogonal frequency-division multiplexing using an optical fast-Fourier-transform circuit," Opt. Lett. **34**, 1828-1830 (2009)

[38]. K. Takiguchi, M. Oguma, H. Takahashi, and A. Mori, "PLC-Based Eight-Channel OFDM Demultiplexer and Its Demonstration with 160 Gbit/s Signal Reception," in Optical Fiber Communication Conference, OSA Technical Digest (CD) (Optical Society of America, 2010), paper OThB4.

[39]. Koichi Takiguchi, Tsutomu Kitoh, Atsushi Mori, Manabu Oguma, and Hiroshi Takahashi, "Optical orthogonal frequency division multiplexing demultiplexer using slab star coupler-based optical discrete Fourier transform circuit," Opt. Lett. **36**, 1140-1142 (2011)

[40]. K. Takiguchi, M. Oguma, H. Takahashi, and A. Mori, "PLC-based eight-channel OFDM demultiplexer and its demonstration with 160 Gbit/s signal reception," in Conference on Optical Fiber Communication, OFC, (San Diego, CA, 2010), paper OThB4.

[41]. Hongwei Chen, Minghua Chen, Feifei Yin, Ming Xin, and Shizhong Xie, "100Gb/s PolMux-NRZ-AOS-OFDM transmission system," Opt. Express 17, 18768-18773 (2009)

[42]. H. Chen, M. Chen, and S. Xie, "All-optical sampling orthogonal frequency-division multiplexing scheme for high-speed transmission system," J. Lightwave Technol. **27**(21), 4848–4854 (2009)

[43]. Arthur James Lowery, "Design of arrayed-waveguide grating routers for use as optical OFDM demultiplexers," Opt. Express **18**, 14129-14143 (2010)

[44]. Zhenxing Wang, Konstantin S. Kravtsov, Yue-Kai Huang, and Paul R. Prucnal, "Optical FFT/IFFT circuit realization using arrayed waveguide gratings and the applications in all-optical OFDM system," Opt. Express **19**, 4501-4512 (2011)

Chapter 4: Nonlinear Signal Processing based on DA-NOLM

Next generation optical networks have urgent demands of high speed signal processing which usually ideally requires the processing in all-optical domain with massive processing capability, such as wavelength conversion [4], packet switching, logic gating, ADC/DAC, sampling, OTDM DEMUX, clock recovery, regeneration, and so on [1-5]. The previously discussed all-optical processing based on passive devices, such as PCF-MZI in Chapter 2 and Sagnac interferometer in Chapter 3, have limited processing capabilities which can be complemented by optical nonlinear processing techniques which keeps the system in optical domain. An example is wavelength conversion, which can simply convert the data from one wavelength carrier to another one by simply sending the signal to the converter [6]. The converter should have fast-enough response so that the data will not be affected during the wavelength conversion and thus high speed operation can be achieved.

All-optical processing based on nonlinear effects can provide ultra fast response and allows a processing speed over terabits. The response time is only several femtoseconds for the third order nonlinearities in optical fibers. Here bellow in Table-1 shows several devices in comparison with their switching speed and the energy consumption, indicating a comparably fast switching speed with acceptable energy consumption for nonlinear fiber [1]. Recently, along with the improvement of high quality fiber fabrication (such as photonic crystal fibers) and short pulse generation, nonlinear fiber has drawn a lot of interest for all-optical signal processing in next generation optical networks [7, 8].

Table 4.1 Switching comparison between several devices [1]

Device	Switching energy	Switching speed
Transistor	10pJ	Sub-ns
SOA-MZI	~100fJ	ps
Micro-ring	10fJ	ns
Dual-ring flip-flop	5fJ	ps
Nonlinear fiber	1-10pJ	fs

4.1 Nonlinear Effects and NOLM for Optical Signal Processing

This section introduces and discusses several third order nonlinear effects in optical fibers, including self phase modulation (SPM), cross phase modulation (XPM), four wave mixing (FWM), and optical parametric amplification (OPA). The basic properties of those nonlinear effects in highly nonlinear optical fiber (HNLF) together with typical nonlinear signal processing applications are described in Section 4.1.1 Nonlinear optical loop mirror (NOLM) as an active optical interferometer for nonlinear signal processing is described in Section 4.1.2.

4.1.1 Nonlinear Effects for Optical Signal Processing

The optical nonlinear effects include a variety of phenomenon which is induced by the nonlinear response to the optical field that is applied to the nonlinear medium [9]. The nonlinear medium discussed in this work is optical fibers which has its nonlinear effects induced by the third order nonlinearity, which can be described by using nonlinear refractive index given by

$$n(\omega,|E|^2) = n(\omega) + n_2|E|^2 \qquad \text{(Eq.4.1)}$$

in which, $n(\omega)$ is the linear index and $|E|^2$ is the optical field intensity. n_2 is the nonlinear refractive index coefficient, which is a material parameter indicating the nonlinear efficiency. The material of optical fiber is fused silica, which has a n_2 of 2.5×10^{-20} m^2/w.

Nonlinear coefficient γ to describe the nonlinearity of an optical fiber, as given by

$$\gamma = \frac{2\pi n_2}{\lambda A_{eff}} \qquad \text{(Eq.4.2)}$$

One can either reduce the mode effective area A_{eff} or increase n_2 to increase the nonlinear coefficient. Generally, HNLF is fabricated by reducing the core diameter to reduce A_{eff}. As an example, SMF has a γ of ~1 W^{-1}km^{-1}. With reduced core diameter, HNLF usually has a γ above 10 W^{-1}km^{-1}.

Self Phase Modulation (SPM)

SPM is induced by temporal variation of the optical intensity, which introduces a time-varying nonlinear index change and thus results in the phase change ϕ_{NL} which can be described by

$$\phi_{NL} = \gamma P(t) l_{NL} \qquad \text{(Eq.4.3)}$$

in which, $P(t)$ is the instantaneous signal power and l_{NL} is the effective nonlinear fiber length. The time-varying phase change along with the time-varying instantaneous signal power generates new instantaneous frequencies with the frequency difference of $\partial\omega$ as given by [9]

$$\partial\omega = -\frac{\partial\phi_{NL}}{\partial t} = -\frac{\partial}{\partial t}\left[\gamma P(t) l_{NL}\right] \qquad \text{(Eq.4.4)}$$

Therefore, with a constant value of $P(t)$, $\partial\omega$ would be zero even with a large value

of $P(t)$. Thus, SPM only occurs to pulses rather than continues waves.

SPM can significant broadens the spectrum by generating new frequency components. Thus, it can be used in a lot of areas, including nonlinear optical signal processing in optical communications. By utilizing the newly generated frequency components, wavelength conversion can simply be obtained by using a filter. Meanwhile, since the nonlinear effects request high instantaneous power which means that SPM will not occur to bit-zeros. Therefore, the newly generated components are all contributed by bit-ones and thus regeneration and ER enhancement can be achieved [10-12].

Fig. 4.1 shows the SPM using 1-km HNLF which has a nonlinear coefficient of 11 $W^{-1}km^{-1}$ at 1550 nm. The 10-GHz optical pulse train with 10-ps pulse width is amplified using an EDFA which boosts the pulse train to average power of 20 dBm and 26 dBm. The high power pulse train is launched into the HNLF and the output spectra are measured as shown in Fig. 4.1. Significantly spectral broadening is observed in Fig. 4.1(b) and Fig. 4.1(c) with respect to the original input pulse without SPM in Fig. 4.1(a). The four-peak spectrum of Fig. 4.1(b) indicates that the peak phase change induced by SPM at the pulse center is ~3.5π [9]. Thus, the phase peak change would be ~10.5π for the SPM in Fig. 4.1(c).

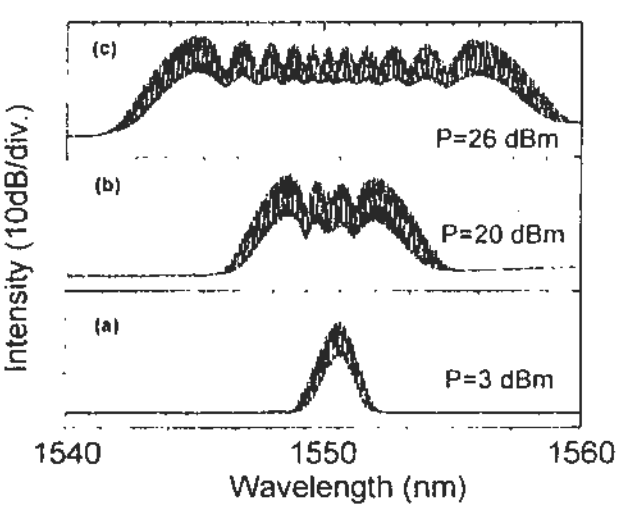

Fig. 4.1 SPM induced spectral broadening.

Cross Phase Modulation (XPM)

The principle of XPM is quite similar to that of SPM, which requires time-varying intensity phase change to generate frequency components. XPM involves two input lights with one of them as the pump and the other one as the probe. The pump light has a high and time-varying power, such as pulses. The probe light could be CW light and also pulses. The phase change induced by the pump light results in a phase modulation at the probe light and thus scatters the power from the probe carrier to other frequency components.

The probe light's phase change contributed by XPM is given by Eq.4.5, which is two times of the phase change by SPM at the same power level [9].

$$\phi_{NL,\ XPM} = 2\gamma P_{pump}(t) l_{NL} \qquad \text{(Eq.4.5)}$$

Since XPM can convert the information from the pump to the probe, it has been widely investigated as a wavelength converter for OOK signals. Wavelength conversion up to terabits has been demonstrated based HNLFs [13]. Similar to SPM, XPM is also able to suppress the noise at bit-zeroes and thus can be utilized for regeneration and ER enhancement. Meanwhile, UWB generation can also be achieved simply by XPM with carefully frequency filtering [14]. With the probe light carrying OTDM data and the pump light as a based band pulse train, optical time division DEMUX for OTDM signals can be achieved [15, 16]. Those applications require careful consideration of the walk off between the pump and the probe. The walk off will reduce the effective nonlinear fiber length and thus affects the XPM significantly.

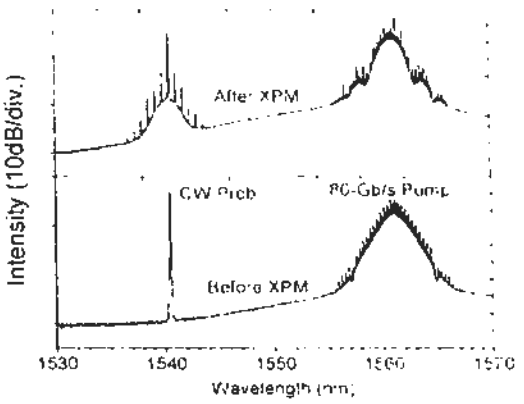

Fig. 4.2 XPM induced spectral broadening.

Fig. 4.2 shows the XPM process utilizing an 80-Gb/s OOK signal as the pump and a CW light as the probe. The 80- Gb/s OOK signal at 1561 nm is boosted to ~20 dBm for pump and is launched in to the HNLF together with the CW probe at 1540 nm. The HNLF has a nonlinear coefficient of 11 $W^{-1}km^{-1}$ at 1550 nm. The CW probe ensures that the spectral broadening at the probe wavelength is contributed only by XPM. The output spectrum in Fig. 4.2(upper) indicates the obvious broadening at 1540 nm.

Four Wave Mixing (FWM)

The nonlinear phenomenon, known as four wave mixing (FWM), is also originates from the third nonlinearity, the same as that of SPM and XPM. In FWM process, consider three inputs with carrier frequencies of ω_1 , ω_2 , and ω_3 propagating simultaneously inside the HNLF, their interaction of the optical fields will generate a fourth field whose frequency ω_4 would be $\omega_4 = \omega_1 \pm \omega_2 \pm \omega_3$ [9]. The interaction can be understood as a beating, which forms a grating and thus scatters the power to the fourth field.

With two of the three inputs having the same field, meaning only two inputs actually, FWM can also be achieved and it is called degenerate FWM which has been widely studied due to its simplified configuration. The degenerate FWM can be described as Eq.4.6,

$$E_{idler} = \left(E_{pump} E_{signal}^{*}\right) E_{pump} \gamma_{(\Delta\omega)} \exp i(\omega_{idler} t + \Delta\phi_{idler}) \qquad \text{(Eq.4.6)}$$

where E_{signal}, E_{pump} and E_{idler} are the field amplitudes of the signal, pump and newly generated idler. $\gamma_{(\Delta\omega)}$ is the complex coupling coefficient which decreases rapidly as $\Delta\omega = \left|\omega_{pump} - \omega_{signal}\right|$ increases. $\Delta\phi_{idler} = 2\phi_{pump} - \phi_{signal}$ is the phase of the idler which includes the phase of the signal and thus carries the phase information. Therefore, FWM can be used for wavelength conversions for both OOK and PSK signals. Shown in Fig. 4.3 is the spectrum all-optical wavelength conversion for 160-Gb/s OOK signals based on degenerate FWM.

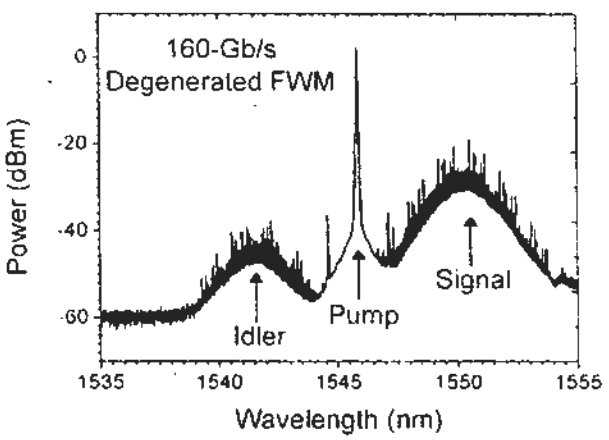

Fig. 4.3 Spectrum of degenerate FWM for 160-Gb/s all-optical wavelength conversion.

The wide range of FWM application includes wavelength conversion, wavelength multicasting, all-optical regeneration, phase sensitive amplification, format conversion and optical phase conjugation (OPC) [17-24]. Among those

applications, OPC is the one that is capable of long haul dispersion compensation which is called mid-span dispersion compensation. Shown in Fig. 4.4 are the experimental eye diagrams for 100-km SMF transmission of 40-Gb/s OOK signal assisted by FWM for OPC. After the 50-km transmission, the dispersion induces significant pulse broadening and left only noise on the eye diagram. With FWM for wavelength conversion to obtain a phase conjugated idler for another 50-km transmission, the dispersion is compensated and open eye is obtained.

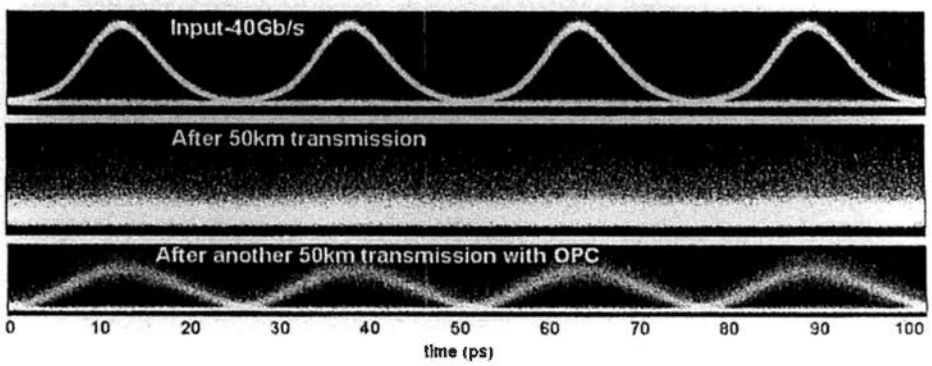

Fig. 4.4 Eye diagrams for 100-km transmission based on mid-span dispersion compensation by OPC.

Optical Parametric Amplification (OPA)

Optical parametric amplification (OPA) is an attractive technology which has recently been drawing much attention due to its advantageous high gain optical amplification with quantum limited noise figure [25]. The origin of OPA in optical fiber is also the third order nonlinearity which can be described by modulation instability [9, 26]. It is indicated that the OPA gain spectrum is primarily determined by the phase matching condition $\Delta\beta$ which is related to dispersion coefficients of β_2 and β_4 as described by Eq.4.7 [25]

$$\Delta\beta = \beta_2\left(\left|\omega_{signal} - \omega_{pump}\right|\right)^2 + \beta_4\left(\left|\omega_{signal} - \omega_{pump}\right|\right)^4 / 12 \qquad \text{(Eq.4.7)}$$

where, ω_{signal} and ω_{pump} are the frequencies of the signal and pump. Thus, the OPA gain range satisfies $-4\gamma P_0 < \Delta\beta < 0$, in which γ and P_0 are the fiber nonlinear coefficient and pump power, respectively. With high order dispersion neglected when $\beta_2 >> \beta_4$, one can only have $\Delta\beta < 0$ with $\beta_2 < 0$. Therefore, OPA only happens at the anomalous dispersion region (ADR). However, with a comparatively large β_4, OPA can also happen at the normal dispersion region (NDR) with $\beta_2 > 0$, which requires a large and negative β_4 and a comparably large frequency division of $|\omega_{signal} - \omega_{pump}|$ to satisfy the phase match condition [25, 26].

Fig. 4.5 shows the comparison of OPA phase matching conditions between the ADR pump and NDR pump, indicating the different gain regions: for the pump in ADR, the gain is close to the pump and has a wideband gain region; the the pump in NDR, the gain is far away from the pump and has a narrow band gain region [26].

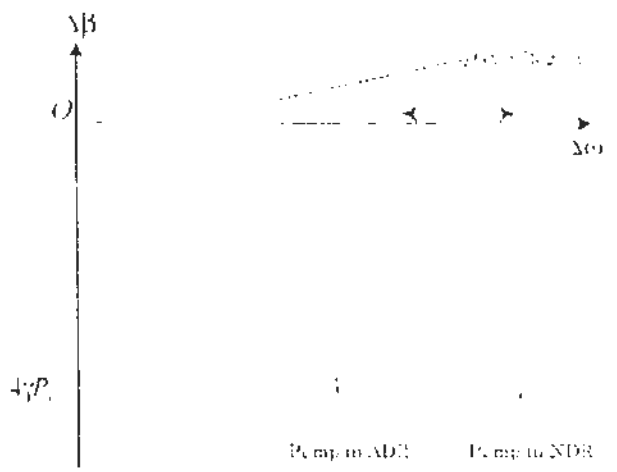

Fig. 4.5 Phase matching indicating the OPA gain bandwidth for the pump in anomalous dispersion region (ADR) and normal dispersion region (NDR) [26].

Fig. 4.6 shows the OPA spectra utilizing a 10-GHz pump pulse with 10-ps pulse width. The OPA fiber is a HNLF with the zero dispersion wavelength located

at 1550 nm. The dispersion slope at 1550 nm is 0.02 ps/nm^2/km. The NDR pump results in a wideband gain symmetrically aside the pump wavelength. The amplified ASE sidebands indicate a peak gain of 21 dB with 20-dBm average pump power.

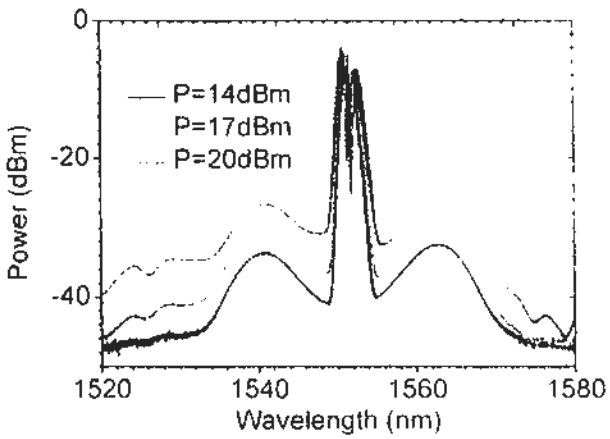

Fig. 4.6 OPA spectra with amplified ASE sidebands.

4.1.2 NOLM for Optical Signal Processing

Nonlinear optical signal processing based on nonlinear optical fiber loop mirror (NOLM) has widely been studied. Due to its self-switching ability, the flexibility and simplicity for implementation, and the massive capability for variety of processing functions, NOLM is recognized as a valuable device in the area of optical communications [27].

NOLM is constructed with a fiber loop mirror within which a HNLF is included. Intrinsically, NOLM is an interferometer (Sagnac interferometer) with the clockwise branch and counter clockwise branch as the two interference light branches. Therefore, the interferometer shares a single optical path which makes the loop mirror as a total reflection loop without nonlinear process.

However, by introducing the different nonlinear processes between the clockwise and counter clockwise branches, such as SPM, XPM, FWM and OPA,

one can obtain a phase difference and thus a switching can be achieved rather than total reflection. Since nonlinear effects are utilized for the switching, ultra high speed operation capability can be expected by NOLM. Another noticeable advantage of NOLM is its processing capability, included are optical switching, phase conjugation, wavelength conversion, wavelength multicasting, OTDM DEMUX and add-drop multiplexing, mode locking, pulse compression and pedestal suppression, optical regeneration, analog to digital conversion, logic gating, and so on [28-33].

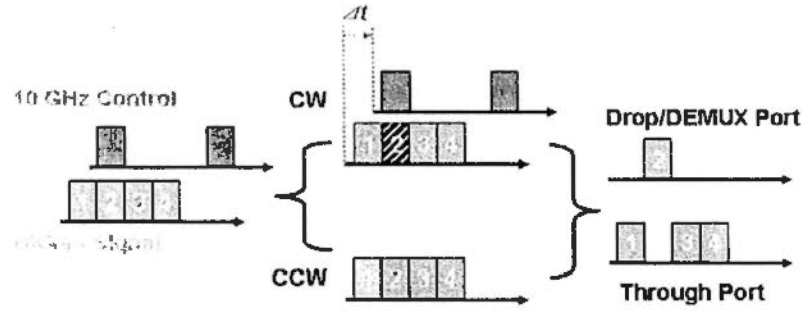

Fig. 4.7 Schematic illustration of a 40-to-10 Gb/s all-optical OTDM DEMUX scheme based on NOLM.

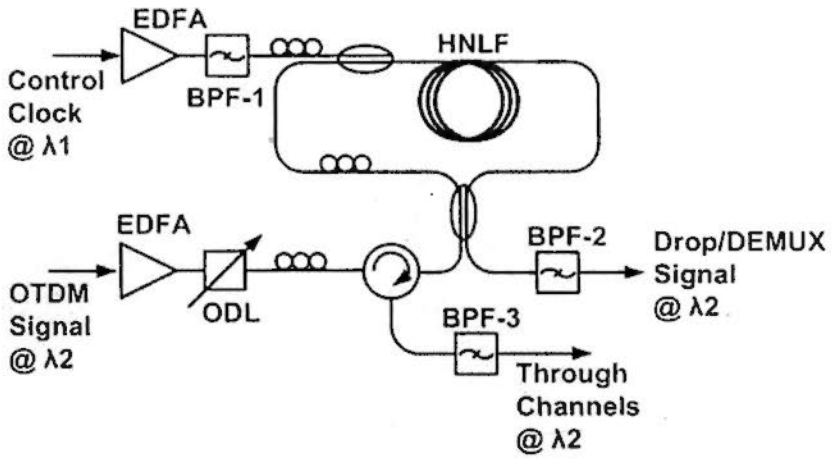

Fig. 4.8 Configuration of a NOLM based OTDM demultiplexer. ODL: optical delay line; BPF: bandpass filter; EDFA: Erbium doped fiber amplifier

One of the widely demonstrated applications of NOLM is its use for optical OTDM DEMUX, as schematically illustrated in Fig. 4.7. The nonlinear process happens only in one branch, the clockwise (CW) branch, which introduces a phase change to channel-2 over the signal. The counter clockwise (CCW) branch operates without nonlinear process. Therefore, with the phase difference for interference at the coupler, channel-2 can be switched out from the 40-Gb/s signal and thus OTDM DEMUX is achieved. The configuration of the demultiplexer based NOLM is shown in Fig. 4.8, which is also the experimental setup for the 160-to-10 Gb/s optical DEMUX.

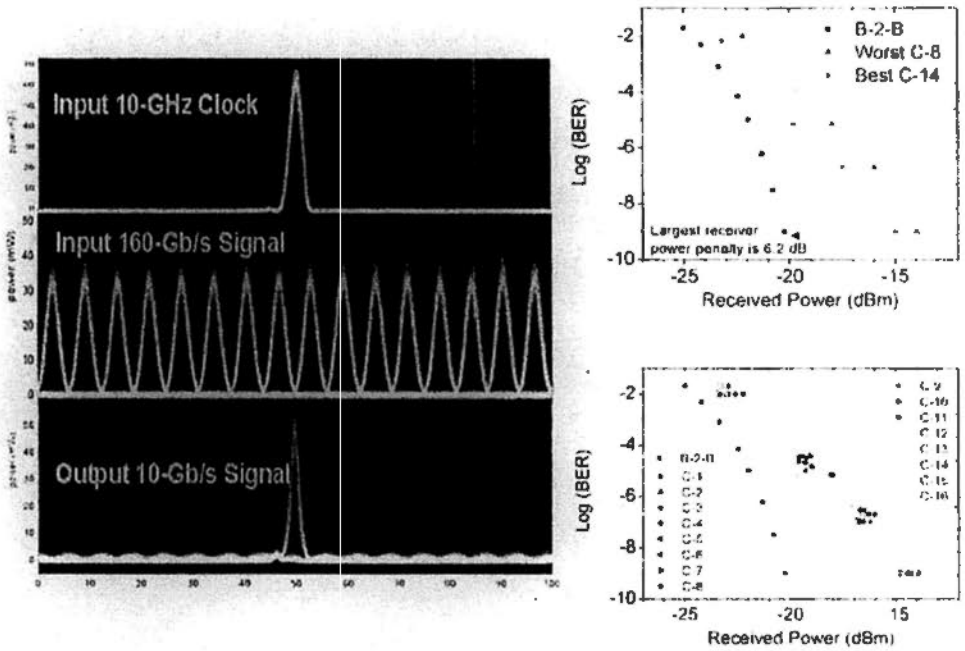

Fig. 4.9 The results for 160-to-10 Gb/s optical DEMUX. The eye diagram (left) after DEMUX is widely open. The BER measurements (right) indicate the error free operation [29].

The results shown in Fig. 4.9 are the eye diagrams as well as the bit error rate measurements for 160-to-10 Gb/s optical DEMUX. The 10 channels are all

error free after the NOLM DEMUX with the largest receiver power penalty of 6.2 dB.

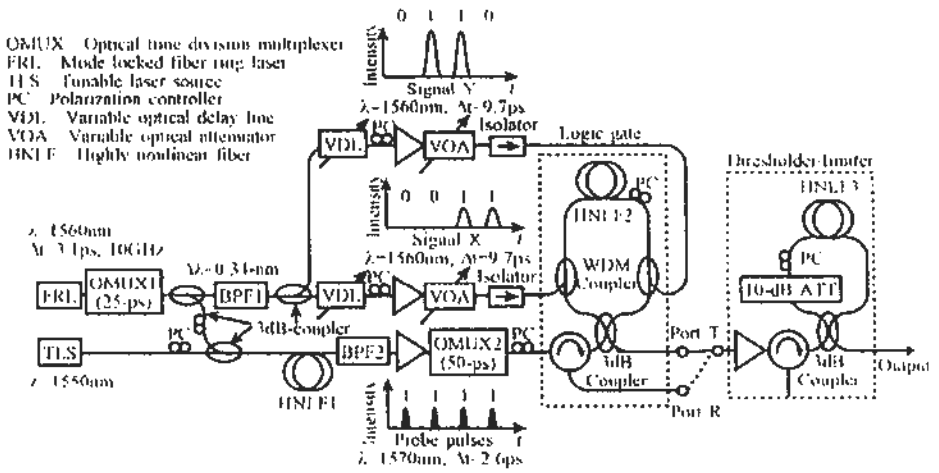

Fig. 4.10 Configuration of the versatile logic gates [34].

The NOLM has flexible configurations which enables a variety of optical signal processing functions. Fig. 4.10 introduces a complex configuration of NOLM for logic gating which indicates the flexible and massive processing capability of NOLM. With such a configuration based on NOLM, one can obtain logic gate operations of AND, NAND, OR, NOR, XOR, and XNOR [34].

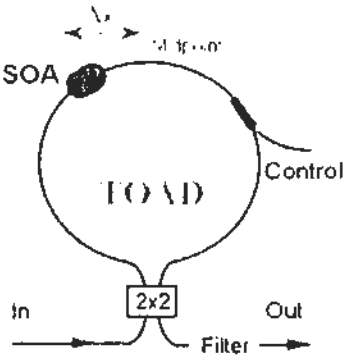

Fig. 4.11 Schematic illustration of a TOAD [35].

There are also some variants of NOLM which utilizes nonlinear medium like SOA rather than HNLF for the nonlinear process. One of which worth of

noticing is terahertz optical asymmetric demultiplexer (TOAD) which is based on SOA [35, 36]. Differs from HNLF in which the nonlinear process only happen between the co-propagating beams in the same direction, the nonlinear effects like XPM can also happen between the counter propagating two beams in SOA. Therefore, the offset of SOA from the midpoint of the loop mirror will results in a narrow gating window with respect to a comparably large control pulse width.

Apart from those NOLM and its variants introduced in this section, there are also dispersion asymmetric NOLM, which will be investigated in the other sections in this chapter with the demonstration of optical signal processing including reconfigurable optical OTDM DEMUX.

4.2 Dispersion Asymmetric NOLM (DA-NOLM)

Dispersion asymmetric nonlinear optical loop mirror (DA-NOLM) differs from the conventional NOLM by introducing a chromatic dispersive medium inside the loop mirror and thus obtain advanced and improved function for optical signal processing [37, 38]. By introducing the dispersive medium, one can obtain an asymmetry for the nonlinear processes between the clockwise and counter clockwise operations. This asymmetry can also be induced by differences in amplification, attenuation, and polarization between the clockwise and counter clockwise operations [39], rather than dispersion asymmetry, which has the advantage of reconfigurable operation capability by wavelength tuning, compared to the other ones.

There have been several demonstrations of DA-NOLM for application in optical signal processing. One can obtain WDM all-optical regeneration by using a DA-NOLM for 10 Gb/s RZ-OOK signals, based on SPM [40, 41]. One can also

achieve pedestal suppressed short pulse generation using DA-NOLM, which is also based on SPM [42, 43]. DA-NOLM for demodulating DPSK signals with bit rate variable operation is also achieved based on FWM [44].

In the following sections, DA-NOLM for optical signal processing is studied. The principle of DA-NOLM is introduced in Section 4.2. Reconfiguration OTDM demultiplexing is investigated in Section 4.3. Two channel all-optical demultiplexing by using one single baseband pulse train is achieved. Repetition rate multiplication is studied in Section 4.4. In Section 4.5, all-optical pulse format conversions with bit rate variable operation are studied. To utilize a dispersion management inside the loop mirror, the modified dispersion asymmetric NOLM (MDA-NOLM) is demonstrated for 80-to-10 Gb/s reconfigurable two-channel DEMUX as presented in Section 4.6.

4.2.1 DA-NOLM as An Active Interferometer

The dispersion asymmetric NOLM (DA-NOLM) is one kind of imbalanced NOLMs, which utilizes the imbalance of nonlinear processes between the clockwise and counter clockwise operations [45, 46]. The imbalance of nonlinear processes can be introduced by asymmetrically distributed gain or attenuation aside the nonlinear medium inside the loop mirror [47-50]. In literatures, DA-NOLM has also been mentioned as dispersion imbalance NOLM and delay asymmetric NOLM [40, 44].

The general configuration of DA-NOLM is shown in Fig. 4.12, in which an imbalance of nonlinear process can be introduced between the clockwise and counter clockwise operations. The 3-dB coupler equally splits the input light into two branches which has the clockwise and counter clockwise light waves went

through the GVD and the nonlinear mediums with opposite orders. The clockwise light wave shall go through GVD process first and nonlinear process afterwards. Contrarily, the counter clockwise light wave will have nonlinear process first and GVD process afterwards. Therefore, phase differences can be obtained due to the imbalanced nonlinear processes when the light waves are recombined together at the coupler. Thus a switching can be achieved for a variety of signal processing.

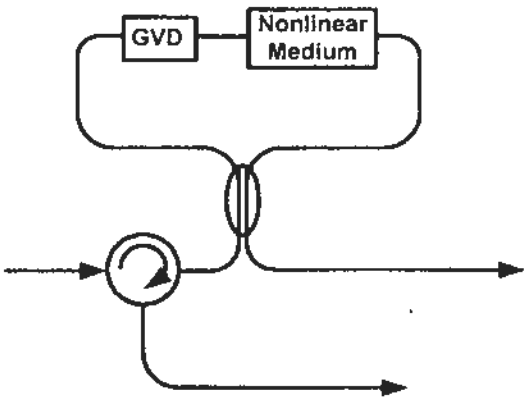

Fig. 4.12 General configuration of a DA-NOLM

One can simply use certain length of SMF or DCF as the dispersive element. For the nonlinear medium, HNLF is used in this work and thus all-fiber configuration of DA-NOLM can be obtained.

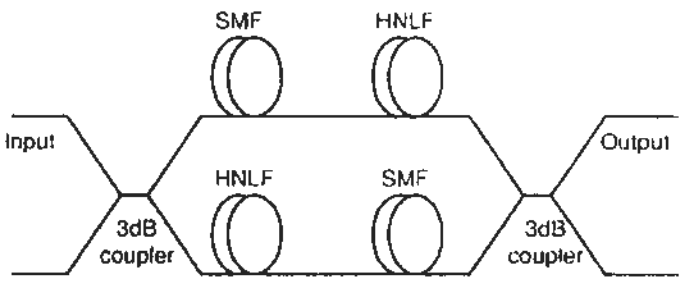

Fig. 4.13 Equivalent Mach-Zehnder interferometer for DA-NOLM [5].

As previously discussed, NOLM is one kind of fiber interferometers, active and nonlinear interferometer. Therefore, the principle of DA-NOLM can be interpreted using an equivalent Mach-Zehnder interferometer configuration, as shown in Fig. 4.13. The nonlinear processes in the HNLF could be SPM, XPM, and FWM, which server different functions.

4.2.2 SPM in DA-NOLM

The SPM process in DA-NOLM enables a variety of signal processing functions including all-optical regeneration, noise suppressing as well as short pulse generation [51-53].

Since SPM only happens for pulses, SPM in DA-NOLM for optical regeneration is only for intensity regenerations. For example as detailed in Ref. 40, the noisy 6X10 Gb/s OOK signals after transmission are regenerated with ~3 dB receiver sensitivity improvement. The signals are amplified and launched into the DA-NOLM. In the clockwise branch, the signals will firstly be broadened by dispersive fibers (DCF) which reduces the peak power and thus a smaller nonlinear phase change was obtained, compared with that in the counter clockwise branch which has a larger nonlinear phase change since the signal went through the nonlinear fiber first. The different nonlinear phase changes results in a phase difference between the two counter propagating light waves and thus a switch was obtained and it only happens for the bit-ones in the signal. Therefore, only the bit-ones were switched out and thus the noise for the signal was reduced and the regeneration is achieved.

The DA-NOLM for pulse generation is also based on SPM, which has a narrowed switching window at the center of the pulse due to the high peak power in

the center compared with the sidebands. Therefore, the output pulse can be compressed with the pedestals been suppressed [42]. One can also notice that the dispersive element can also serve for pulse generation rather than pulse broadening for the deeply phase modulated CW light wave. Thus, based on DA-NOLM, pedestal free pulse generation can also be obtained from a CW input with phase modulation [43].

4.2.3 FWM in DA-NOLM

The degenerate FWM process in DA-NOLM makes the DA-NOLM as a delay interferometer and thus a variety of signal processing functions can be obtained, such as DPSK demodulation [44].

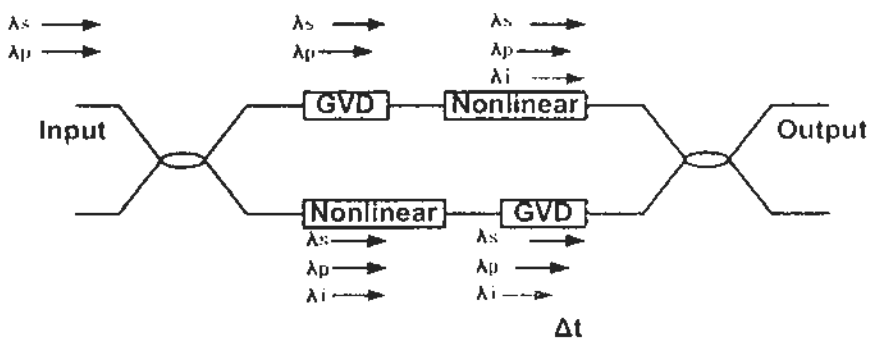

Fig. 4.14 Schematic illustration of the FWM in DA-NOLM based on the Mach-Zehnder interferometer modal.

The delay interference of DA-NOLM can be interpreted by the equivalent MZI modal as shown in Fig. 4.14. The relative delay is regarded to the idler wavelength origins from the FWM in HNLF, whether the idler wavelength is generated before GVD or after GVD. The relative delay is governed by the pump-signal wavelength detuning and thus a tunable delay can be obtained by wavelength

tuning. By utilizing a SMF for introducing the dispersion, the wavelength tunable delay can be described by

$$\Delta t = 2DL_{SMF}(\lambda_s - \lambda_p) \qquad \text{(Eq.4.8)}$$

where D is the dispersion coefficient of SMF and L_{SMF} is the SMF fiber length. λ_s and λ_p are the signal and pump wavelength, respectively. With a 100-ps delay, one can obtain a 0.08-nm FSR at the relevant wavelength. Along with the change of the signal wavelength, the FSR also changes due to the variation of the delay.

4.3 DA-NOLM for Reconfigurable OTDM DEMUX

Optical time division multiplexing (OTDM) is an important technology for generating high speed optical signals while occupying only one single wavelength channel. In OTDM systems, demultiplexing (DEMUX) can be implemented either by electrical or optical means. Along with the rapid increase of bit rates up to tens and hundreds of gigabit/s, it is more favorable to perform all-optical DEMUX, avoiding OEO conversion and offering ultra-fast response of the processing [54, 55]. All-optical DEMUX has been previously demonstrated based on various nonlinear effect in optical fibers and semiconductor optical amplifiers (SOA), such as cross phase modulation (XPM) in a nonlinear optical loop mirror (NOLM) and nonlinear polarization rotation (NPR) [56-58].

In addition, in a reconfigurable optical network, it is necessary to perform dynamic allocation of the bandwidth [59]. An example is in allocating different tributaries from the OTDM signal to one local distribution point, followed by subdividing the tributaries to sub-local distribution points or local users. Such a scenario requires reconfigurable DEMUX which can be realized with cascaded

stages of DEMUX and multiple control pulses with reconfigurable operation. In order to achieve two-channel or multi-channel DEMUX with the above all-optical DEMUX techniques, multi-step operation or multiple pulse control will be required.

4.3.1 DA-NOLM for 40-to-10 Gb/s Two-channel DEMUX

In this part of the thesis work, we demonstrate a solution to use only a single control pulse for simultaneous (one-step) two-channel DEMUX based on a NOLM with asymmetric dispersion inside the loop [60, 61]. Besides, no extra fiber coupler is needed inside the 3-dB fiber loop mirror. Channel selection can be easily realized by wavelength tuning owing to asymmetric dispersion in the fiber loop. All-optical two-channel DEMUX has been achieved for 40-Gb/s OTDM OOK signals. Switchable operation between two-channel and single-channel DEMUX has also been demonstrated, offering the flexibility for reconfigurable operation and for dynamic bandwidth allocation.

The structure of the dispersion asymmetric NOLM (DA-NOLM) is schematically shown in Fig. 4.15(a). The loop mirror contains a nonlinear medium such as a highly nonlinear fiber (HNLF) next to a group velocity dispersion (GVD) element. The GVD element can simply be a standard single mode fiber (SMF) that introduces a relative delay between light branches at different wavelengths (the delay between the control pulse and the OTDM signal in this case). In the counter clockwise (CCW) operation, the control pulse at λ_1 and signal at λ_2 propagate together in the nonlinear medium. XPM will result in a phase change of the signal at λ_2. As for the clockwise (CW) operation, the control and the signal will first arrive at the GVD element where a relative delay will be introduced. Subsequently, the signal will undergo XPM initiated by the relatively delayed control pulse in the

nonlinear medium. However, the phase change now occurs at a different OTDM channel compared to that of the CCW operation. Hence, two different baseband channels can be switched out.

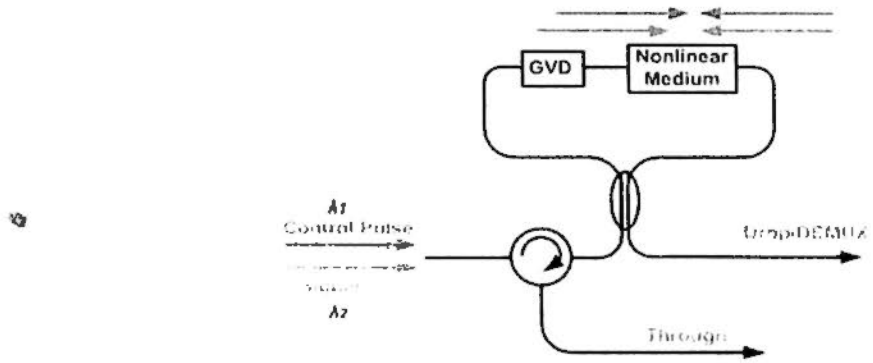

(a)

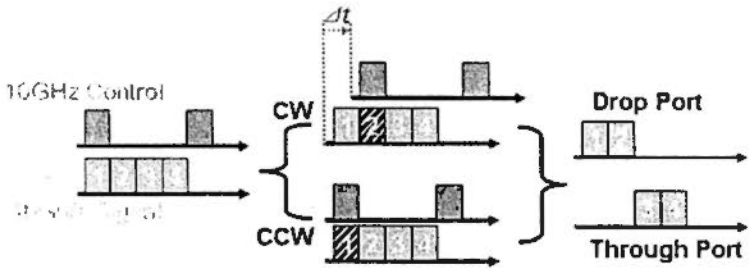

(b)

Fig. 4.15 Schematic illustration of the DA-NOLM for two-channel OTDM DEMUX. GVD: group velocity dispersion; CW: clockwise; CCW: counter clockwise.

In Fig. 4.15(b), we consider a 40-Gb/s OTDM signal. Neglecting the effect on pulse broadening, the output (Drop Port) of the DA-NOLM after XPM can be described as [40]:

$$P^{out} = \frac{1}{2} P^{in}(1 - \cos\Delta\varphi) \qquad \text{(Eq.4.9)}$$

where $\Delta\varphi$ is the phase change between the CW and the CCW operations caused by XPM. Without the control pulse, the zero phase change ($\Delta\varphi$=0) over the input signal makes the loop a total reflecting mirror. With a pulse control and a HNLF as

the XPM medium, one can derive the phase changes of channel-one (C-1) and channel-two (C-2) in the OTDM signal by

$$\Delta\varphi_1 = |\Delta\varphi_1^{cw} - \Delta\varphi_1^{ccw}| = 2|\gamma L(P_1^{cw} - P_1^{ccw})| \quad \text{(Eq.4.10)}$$

$$\Delta\varphi_2 = |\Delta\varphi_2^{ccw} - \Delta\varphi_2^{cw}| = 2|\gamma L(P_2^{ccw} - P_2^{cw})| \quad \text{(Eq.4.11)}$$

In Eq.4.10, γ and L stand for the nonlinear coefficient and the length of the HNLF, and $P_{1/2}^{cw/ccw}$ is the peak control power for the XPM process over C-1/C-2 in the CW/CCW operation. Assume that a control power of P_0 is required for a π phase change and that $P_1^{cw} = 0$, $P_1^{ccw} = P_0$, $P_2^{cw} = P_0$, $P_2^{ccw} = 0$ in Fig. 5.4(b), a π phase change will be introduced for both C-1 and C-2, giving rise to simultaneous two-channel DEMUX according to Eq.4.9.

Table 4.2 Reconfigurable DEMUX with a GVD of 10 ps/nm

$\Delta\lambda$	Δt	Demultiplexed Channels
2.5 nm	25 ps	C-1, C-2
5.0 nm	50 ps	C-1, C-3
7.5 nm	75 ps	C-1, C-4

The relative delay (Δt) is adjustable by wavelength tuning of the control pulse due to the presence of GVD. This feature offers reconfigurability of the demultiplexer. For example, with ~25 ps relative delay, C-1 and C-2 can be simultaneously demultiplexed from the 40-Gb/s OTDM signal, while C-1 and C-3 will be demultiplexed when the relative delay is ~50 ps. The relation between the wavelength spacing and the relative delay is shown in Table 4.2 for different DEMUX channels obtained with a GVD of 10 ps/nm.

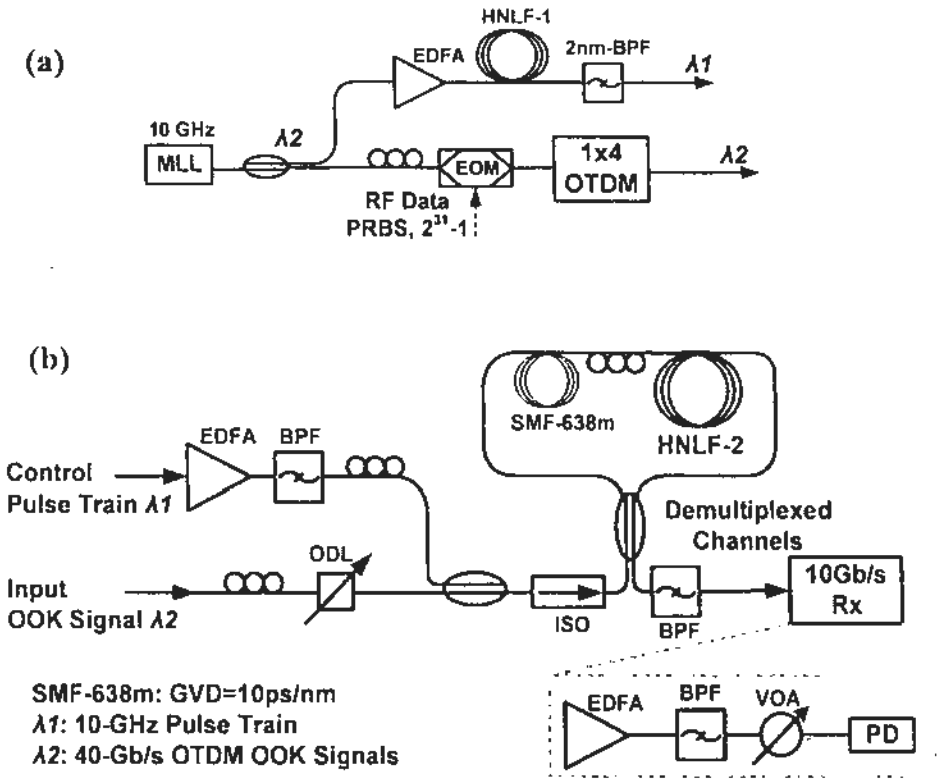

Fig. 4.16 (a) Setup for the generation of 10-GHz control pulse and 40-Gb/s OTDM OOK signal; (b) Setup for two-channel DEMUX based on the dispersion asymmetric NOLM. ODL: optical delay line; BPF: band pass filter; ISO: isolator; PD: photodetector; VOA: variable optical attenuator.

Fig. 4.16 shows the experimental setup for two-channel DEMUX of a 40-Gb/s OTDM OOK signal. In Fig. 4.16(a), the upper branch of the 10-GHz pulse train at $\lambda 2$ is amplified to ~26 dBm (average power) for spectral broadening by self-phase modulation (SPM) in HNLF-1, which has a nonlinear coefficient of 11-$W^{-1}km^{-1}$ at ~1550 nm. The input 10-GHz pulse train at $\lambda 2$ has a pulse width of 10.6 ps. The SPM process in HNLF-1 significantly broadens the spectrum from 2 nm to 14 nm (20-dB bandwidth) as shown in Fig. 4.17. By spectral slicing with a tunable bandpass filter (2-nm Gaussian filter, 3-dB bandwidth) after HNLF-1, we obtain a wavelength tunable 10-GHz control pulsed source with a typical width of 11 ps.

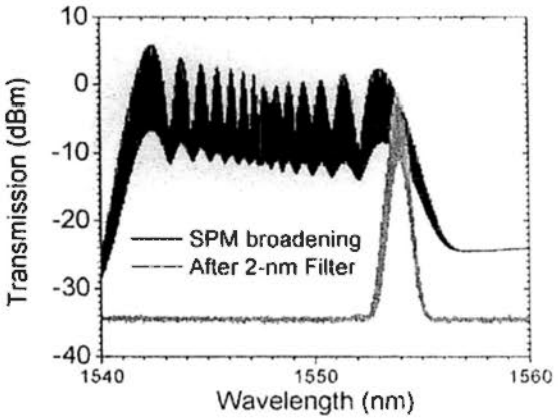

Fig. 4.17 Measured optical spectrum of the 10-GHz control pulse after SPM in the HNLF-1. The lower curve shows a spectrally sliced output.

In Fig. 4.16(a), the lower branch of the 10-GHz pulse train at λ_2 is used in 40-Gb/s OTDM OOK signal generation through electro-optic modulation at 10-Gb/s with pseudo random binary sequence (PRBS, 2^{31}-1) followed by 1×4 optical multiplexing. In this work, we set λ_2 at 1547-nm and tune λ_1 over the range of 1542 to 1556-nm.

The 40-Gb/s OTDM OOK signal is then combined with the 10-GHz amplified control pulse in the optical coupler, as illustrated in Fig. 4.16(b). The signal and the control pulse are together launched into the DA-NOLM through an isolator. Inside the loop, a 638-m SMF is used to introduce the GVD and another 1-km HNLF (HNLF-2) is used as the nonlinear medium. HNLF-2 has a nonlinear coefficient of 11.7 $W^{-1}km^{-1}$ and a dispersion coefficient of 0.02 $ps{\cdot}nm^{-1}km^{-1}$ around 1550 nm. The GVD of the SMF is 10 ps/nm, resulting in a relative delay of 50 ps when $\Delta\lambda = |\lambda_1 - \lambda_2| = 5$ nm. With the 10-GHz control pulse overlapped temporally with C-1 but spaced spectrally at 2.5, 5.0, and 7.5 nm apart from the signal as shown in Fig. 4.18(a), we achieve two-channel DEMUX for C-1/C-2, C-1/C-3 and C-1/C-4, respectively. The corresponding eye diagrams are shown in Fig. 4.18(b).

Meanwhile, according to Fig. 1, C-1 is synchronized with the control pulse before it enters the DA-NOLM. Hence, C-1 rather than the other channels experience XPM in the CCW operation. By synchronizing C-2 instead of C-1 with the control pulse, one can also achieve C-2/C-3 and C-2/C-4 DEMUX with 2.5 and 5.0-nm wavelength detunings, respectively. The two-channel DEMUX results, with widely opened eye-diagrams shown in Fig. 4.18(b), are in good agreement with the analysis in Table-1.

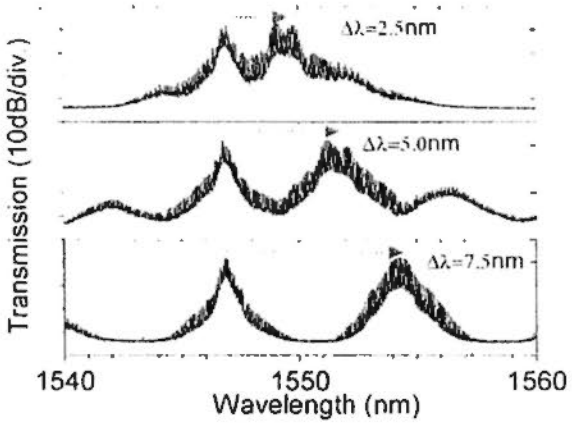

(a)

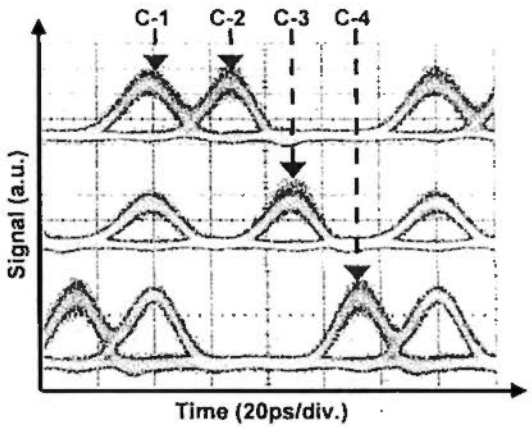

(b)

Fig. 4.18 (a) Spectra showing different wavelength spacings between the control pulse and the OTDM signal for two-channel DEMUX; (b) Eye diagrams of the two corresponding demultiplexed channels.

The proposed DA-NOLM is also capable of single-channel DEMUX. Switchable operation between two-channel and single-channel DEMUX is shown in Fig. 4.19. Here, λ1 is set at 1554.5 nm and C-1 overlaps temporally with the control pulse. The XPM process for C-1 occurs in the CCW operation while that of C-4 occurs in the CW operation after the GVD medium. Since the control and signal pulses are broadened and distorted before demultiplexing takes place through optical gating with XPM, the performance is poorer in the CW operation. In this work, we use a polarization controller (PC) in the fiber loop to balance the DEMUX performances between the two channels. A small difference can still be observed as depicted in Fig. 4.18(b) and Fig. 4.19. The CCW operation DEMUX (C-1) performs slightly better than that of the CW operation (C-2, C-3, C-4).

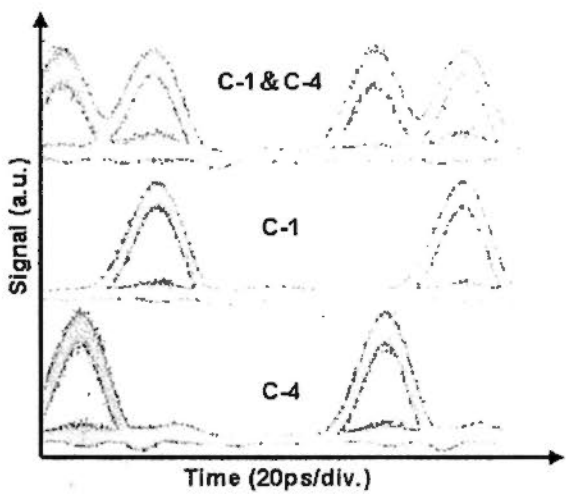

Fig. 4.19 Eye diagrams obtained from two-channel and single-channel switchable DEMUX.

As shown in Fig. 4.19, the eye openings of the selectable single-channel DEMUX obtained by polarization readjustment are comparable to those of two-

channel DEMUX. Based on single-channel DEMUX with control wavelength detunings of 2.5, 5.0 and 7.5 nm, we have performed BER measurements and the results are shown in Fig. 4.20. Error free DEMUX has been obtained for all channels. C-1 DEMUX is obtained by XPM in the CCW operation while C-2, C-3 and C-4 DEMUX are obtained by XPM in the CW operation. The results indicate error free two-channel DEMUX with ~2-dB difference in receiver sensitivity between the two output channels. Compared to the back-to-back 10-Gb/s BER measurement, our demultiplexer introduces ~2-dB and ~4-dB power penalty for CCW and CW operations, respectively. This difference is induced by the dispersion inside the loop mirror which can be improved by dispersion management to minimize the pulse broadening as demonstrated in Section 4.6.

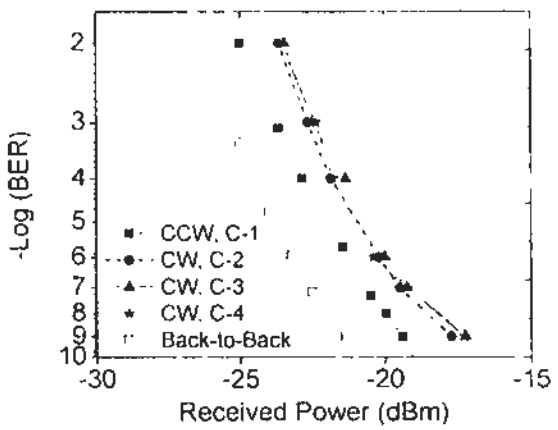

Fig. 4.20 BER measurement results of the DA-NOLM based DEMUX.

It is worth mentioning that to perform a BER measurement for simultaneous two-channel DEMUX, one will need to carry out an extra demultiplexing step to retrieve a single 10-Gb/s tributary, thus resulting in additional power penalty. Hence, the result will not be a fair comparison with that obtained from conventional single-channel DEMUX.

4.3.2 DA-NOLM for 80-to-10 Gb/s Two-channel DEMUX/ADM

It is foreseeable that the proposed DA-NOLM can also be used for other formats like phase shift keying (PSK). Meanwhile, in this part of the thesis work, we use a relatively large GVD (10 ps/nm) to introduce the relative delay. It appears that the GVD can lead to pulse broadening and will be a concern in high-bit-rate DEMUX. To minimize the broadening effect while keeping a large relative delay, one can use a smaller GVD with a larger control-signal wavelength detuning, or a specially designed GVD mapping to compensate the broadening.

Theoretically, with a small GVD but a sufficiently large pump-signal wavelength detuning, the speed limitation can be well improved. However, considering the focus on C-band operation with a wavelength detuning range of ~30 nm limited by the EDFA, the smallest |GVD| that can be used is ~0.85 ps/nm in order to introduce ~50 ps relative delay between the signal and the control pulse for 10-Gb/s baseband OTDM signals (100-ps period). Notice that only half-period delay is needed for the reconfigurable DEMUX and half the required GVD is needed using GVD mapping configuration. Therefore, for a transform limited 320-Gb/s signal with 1.1-ps pulse width (Gaussian pulse with bandwidth ~3.2 nm), the pulse broadening would be ~2.7 ps. Instead, for a 160-Gb/s signal with ~2.0-ps pulse width (Gaussian pulse with bandwidth ~1.8 nm), the pulse broadening is only ~1.5 ps. Since the periods for 320-Gb/s and 160-Gb/s signal are 3.125 ps and 6.25 ps, respectively, we may consider 160-Gb/s operation be a limit for the DEMUX with a baseband of 10-Gb/s. In such a case, using higher speed baseband signal is another approach for improving the speed limitation.

Considering the operation in C-band for 10-Gb/s baseband OTDM signals based on the same setup using another SMF, we have obtained 80-to-10 Gb/s two-change reconfigurable demultiplexing.

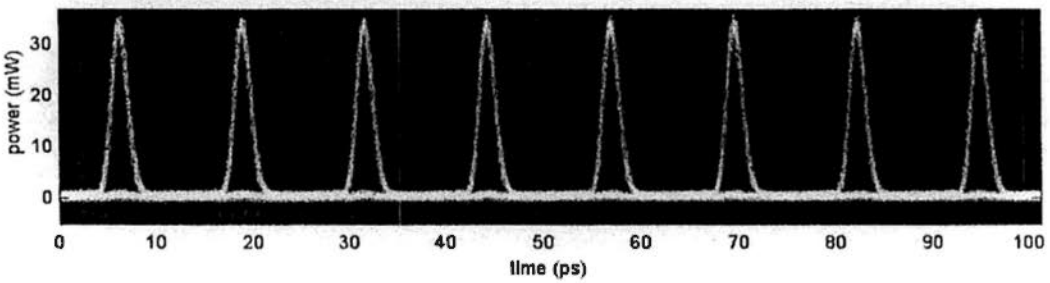

Fig. 4.21 Eye diagram of the 80-Gb/s OTDM signal.

As shown in Fig. 4.21, the 80-Gb/s OTDM signal has a pulse width of ~3 ps. The generation of the wavelength tunable 10-GHz control pulse is also based on SPM in a HNLF which generates a much wider and flatter super-continuum as depicted in Fig. 4.22. The control pulse width is ~2 ps and the average pump power is 15 dBm.

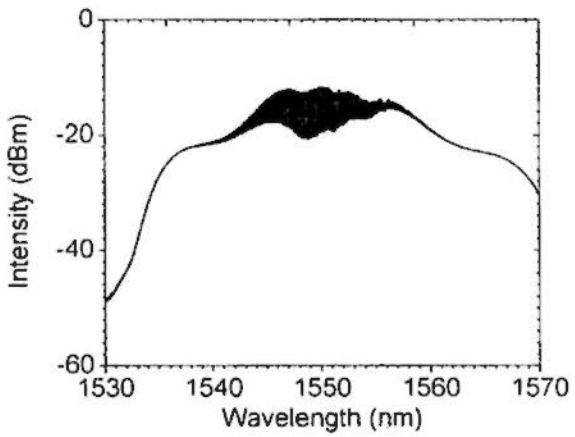

Fig. 4.22 Super-continuum generated by SPM using a 10-GHz pulse train.

The SMF utilized for 80-to-10 Gb/s optical DEMUX has a length of 270 m which introduces a GVD of 4.6 ps/nm. The input spectrum shown in Fig. 4.23

indicates different delays of 25 ps, 37.5 ps and 50 ps for the DEMUX with different pump wavelengths of 1548.4 nm, 1545.6 nm and 1543 nm, respectively. The control pulse is obtained by spectral slicing using a 2-nm BPF and the averaged pulse width of the wavelength tunable 10-GHz is ~4 ps.

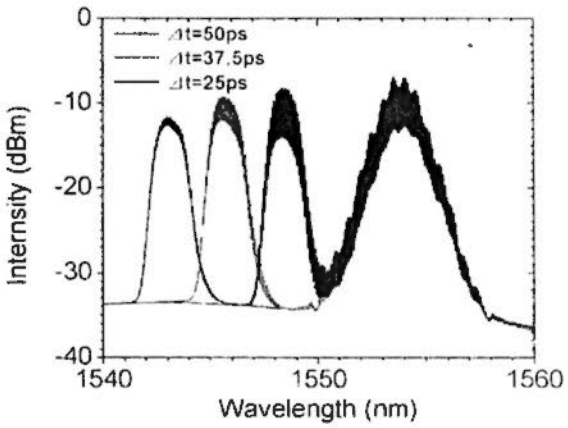

Fig. 4.23 Input spectra indicating the tuning of the control wavelength for reconfigurable DEMUX.

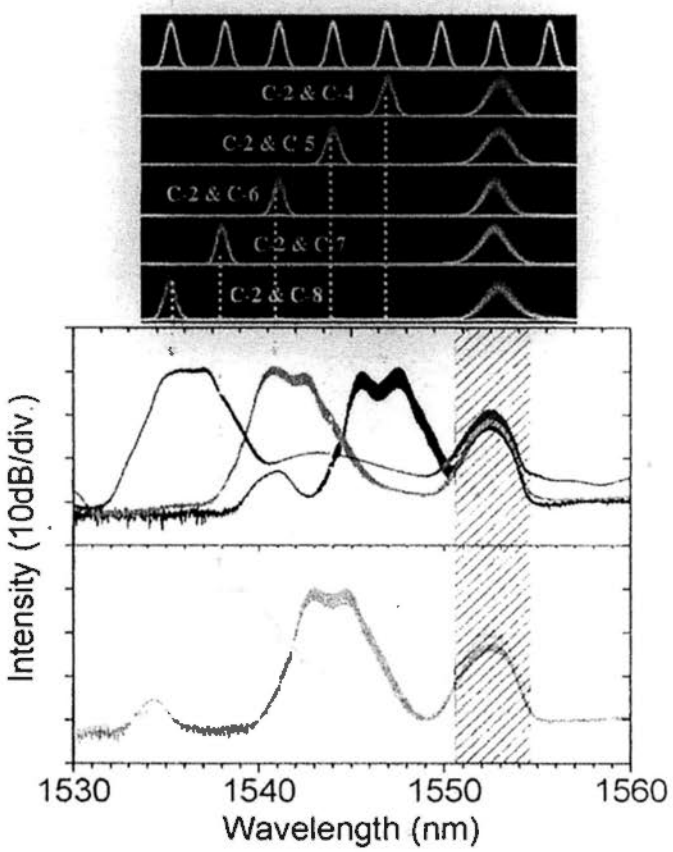

Fig. 4.24 Output eye diagrams and spectra for the two-channels 80-to-10 Gb/s optical demultiplexing.

The results shown in Fig. 4.24 are the output spectra and eye diagrams after the demultiplexing. The two-channel demultiplexing is achieved with different combinations. Five DEMUX schemes are shown in Fig. 4.24 with the control wavelength tuned to 1548.4 nm, 1545.6 nm, 1542.7 nm, 1539.2 nm, and 1536.5 nm. The signal is located at 1553 nm. The demultiplexed two channels have different pulse widths, one contributed by the CCW operation has smaller pulse width of 3.5 ps with respect to the other one with 7-ps pulse with which is contributed by the CW operation. The difference of the pulse width is caused by the different switching window and the different broadening due to the GVD.

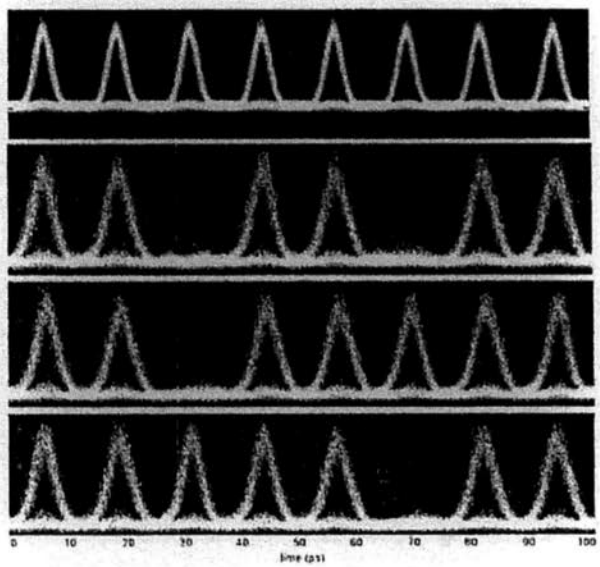

Fig. 4.25 Switchable operation between two-channel DROP and signal channel DROP based on the DA-NOLM.

One can simply detect the output signal at the through port of DA-NOLM and thus obtain the DROP function for ADM. As shown in Fig. 4.25 are the eye

diagrams for signal with switchable operation between two-channel and one channel drop. Significant suppression of the drop channels can be observed with the left channels still widely eye-open. There is also pulse broadening of the left channels due to the presence of GVD. The pulse broadening of the DEMXU and ADM can both be improved by dispersion management as investigated in Section 4.6.

4.4 DA-NOLM for Repetition Rate Multiplication

Repetition rate multiplication is usually realized using passive devices, such as delay interferometer like PCF-MZI that have demonstrated in Chapter 2. The intrinsic shortage of those passive devices is their fixed FSR, meaning the dedicated operation repetition rate. Even with extra external control, thermally or mechanically, it is still difficult to achieve wideband bit rate variable operation based on those passive devices.

The DA-NOLM as an active and nonlinear delay interferometer has different FSR at different wavelengths. Therefore, the tunable delay interference can be obtained simply by control wavelength tuning. Based on the XPM in DA-NOLM, one can achieve repetition rate multiplications with repetition rate variable operations.

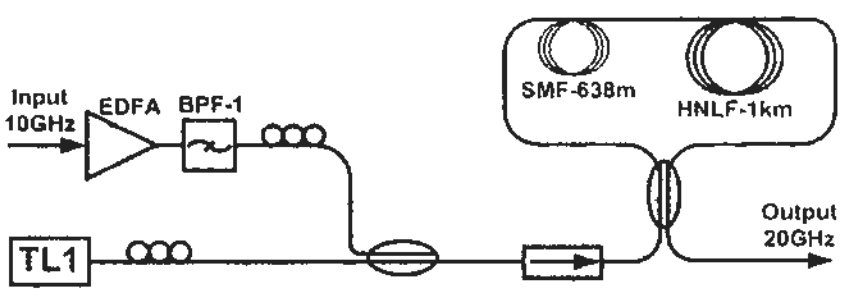

Fig. 4.26 Experimental setup for 10-to-20 GHz repetition rate multiplication.

The setup for the repetition rate multiplication based on DA-NOLM is shown in Fig. 4.26, which is similar to the one for OTDM DEMUX in Section 4.3, only the OTDM signal is replaced by the CW light from the tunable laser. The input 10-GHz pulse is generated by a mode locked fiber laser which has a pulse width of 2 ps. Although the control pulse have unstable phase due to the active mode locking, one can still obtain a repetition rate multiplied pulse train with well improved phase coherence at the probe wavelength. Thus, the phase coherent pulses can be used PSK modulation formats.

Fig. 4.27 shows the output spectra of DA-NOLM for the repetition rate multiplication with different probe wavelengths. The six probe wavelengths correspond to different delays. With a half period delay or the odd multiples of half period delay, repetition rate multiplication can be obtained. Since the dispersion of SMF is 10-ps/nm and the control wavelength is 1560-nm, we can expect the multiplication can be achieved around the wavelengths of 1555-nm and 1545-nm, which introduces relative delay of 50-ps and 150-ps, respectively.

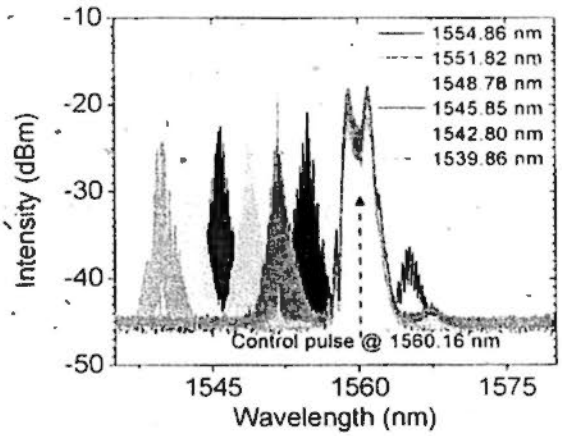

Fig. 4.27 DA-NOLM output spectra with different probe wavelengths.

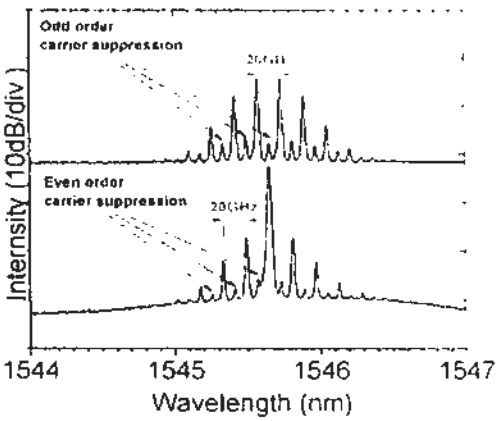

Fig. 4.28 Spectrum of the 20-GHz pulse after the repetition rate multiplication.

The spectrum shown in Fig. 4.28 indicates the alternative suppressing of the 10-GHz clock tones and thus results in the 20-GHz carrier spacing at the probe wavelength of 1545.6 nm. By simply wavelength tuning, one can obtain different suppression of the sub-carriers. Indicated from the center carrier suppression in Fig. 4.28, a suppression ratio of 25-dB can be obtained, which means a comparably large ER of 25-dB can be introduced by the active and nonlinear delay interferometer of DA-NOLM.

4.5 DA-NOLM for Tunable Pulse Format Conversion

We have previously demonstrated pulse format conversions based on PCF-MZI, which is a passive delay interferometer [62]. In this part of the thesis work, the FWM based DA-NOLM as the active and nonlinear delay interferometer for pulse format conversions can also be achieved [63]. The operation principle is the same as that based on PCF-MZI, which utilizes the delay interference for spectral shaping. Differs from PCF-MZI which has fixed delay, due to the tunable delay of DA-NOLM, the pulse format conversions, including RZ-to-NRZ and NRZ-to-PRZ, are

bit rate variable. The simultaneously wavelength conversion based on the degenerate FWM also enables the operation for phase incoherent signals, which is particularly important for high speed OTDM signal generated MLFL.

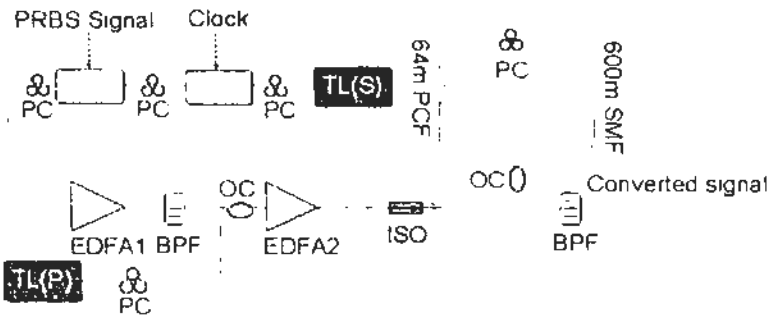

Fig. 4.29 Experimental setup of the DA-NOLM for bit-rate variable format conversions [63].

Shown in Fig. 4.29 is the experimental setup for the pulse format conversion. A tunable laser at 1549.4 nm is used to generate an input RZ-OOK or NRZ-OOK signal (PRBS, 2^{31}-1) using electro-optic intensity modulators (EOMs). The pump is produced by another tunable laser and it is combined with the signal through a 3 dB coupler. The pump and the signal are launched together to the DA-NOLM after EDFA amplification. The DA-NOLM is constructed with a 64-m dispersion flattened photonic crystal fiber (PCF) as the FWM medium and a 600-m standard single mode fiber (SMF) with a ~10 ps/nm group velocity dispersion [44]. The PCF has a nonlinear coefficient of 11 $W^{-1}km^{-1}$ and a dispersion coefficient of -1.3 ps/nm/km at ~1550 nm. The 3-dB wavelength conversion bandwidth for FWM is ~16 nm. By fine tuning the pump wavelength to control the relative time delay and the phase difference, format conversions can be achieved at variable bit rates. A BPF is used at the output port of the DA-NOLM to extract the converted signal at the idler wavelength.

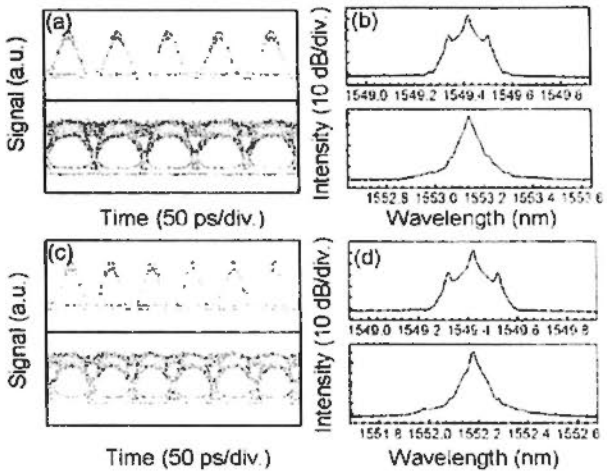

Fig. 4.30 (a) and (b): eye diagrams and spectra of 10 Gbit/s input RZ-OOK signal (top) and converted NRZ-OOK signal (bottom); (c) and (d): eye diagrams and spectra of 12.5 Gbit/s input RZ-OOK signal (top) and converted NRZ-OOK signal (bottom).

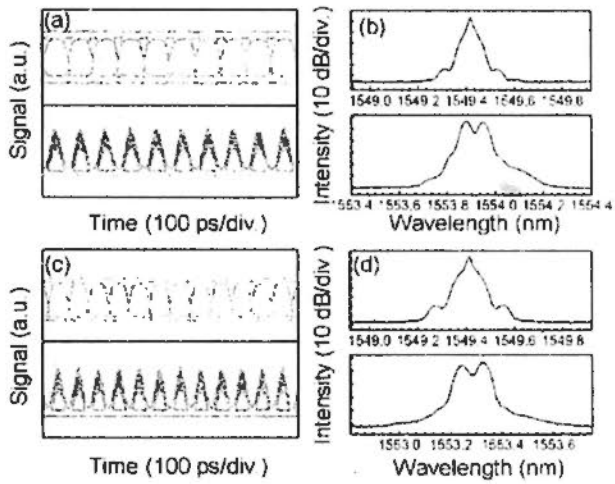

Fig. 4.31 (a) and (b): eye diagrams and spectra of 10 Gbit/s input NRZ-OOK signal (top) and converted PRZ signal (bottom); (c) and (d): eye diagrams and spectra of 12.5 Gbit/s input NRZ-OOK signal (top) and converted PRZ signal (bottom)

The eye diagrams and optical spectra of the input and output signals for 10 and 12.5 Gbit/s RZ-to-NRZ format conversions are shown in Fig. 4.30. And the results for NRZ-to-PRZ format conversion at 10 and 12.5 Gbit/s are shown in Fig. 4.31. The plots indicate the bit rate variable operation of the pulse format

conversions with widely opened eye diagrams. Due to the nonlinear process, there is extra noise introduced compared to the operation using passive devices such as PCF-MZIs.

4.6 Modified DA-NOLM for Signal Processing

Previously in Section 4.3, we demonstrated the use of a DA-NOLM for reconfigurable DEMUX of 40-Gb/s On-Off keying (OOK) signals [60, 61]. The operation speed of the DEMUX is limited due to group velocity dispersion (GVD) inside the loop mirror that leads to pulse broadening, especially when the signal pulse becomes shorter and occupies a wider bandwidth.

In this part of the thesis work, we propose a modified dispersion-asymmetric nonlinear optical loop mirror (MDA-NOLM) [64, 65] which has a specially designed dispersion management. The aim is to minimize the total GVD inside the loop while maintaining a large dispersion imbalance on both sides of the nonlinear medium.

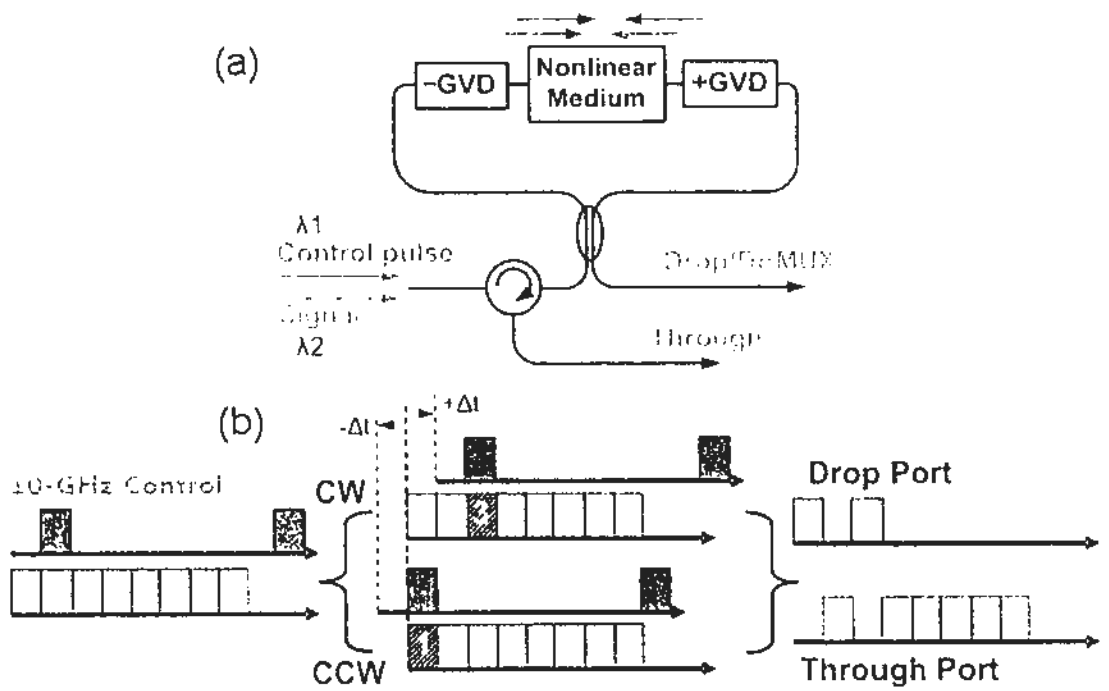

Fig. 4.32 Schematic illustration of the MDA-NOLM for two-channel OTDM DEMUX. GVD: group velocity dispersion; CW: clockwise; CCW: counter clockwise.

The structure can be simply implemented using two dispersive elements with equal but opposite GVDs, as illustrated in Fig. 4.32. Standard single mode fiber (SMF) and dispersion compensating fiber (DCF) can be used to provide normal dispersion (+GVD) and anomalous dispersion (–GVD) respectively around 1550 nm. By specially tailoring their lengths to satisfy |–GVD| = |+GVD|, we can obtain full dispersion compensation for the signal and thus a ZERO dispersion inside the loop mirror. The pulse broadening is thus minimized. The opposite GVDs on both sides of the nonlinear medium will enhance the imbalance performance between the clockwise (CW) and the counter-clockwise (CCW) operations in the loop mirror. With the MDA-NOLM, the speed performance of reconfigurable optical DEMUX is significantly enhanced.

In Fig. 4.32(a), the control pulse at λ1 and the optical time-division-multiplexed (OTDM) signal at λ2 (>λ1) are combined and are launched together into the MDA-NOLM. For the CW operation, λ1 will lead λ2 after the "–GVD" element. Cross phase modulation (XPM) will subsequently take place in the nonlinear medium. A relative delay between the control pulse and the OTDM signal is given by $-\Delta t = (\lambda 1-\lambda 2) \times (-GVD)$. Along with the delay, the "–GVD" also introduces pulse broadening which will be compensated by an opposite dispersion element "+GVD" after the nonlinear medium. Therefore, the signal will remain un-broadened while the phase of one selected tributary (channel-3: C-3) will be changed by XPM as illustrated in Fig. 4.32(b). As for the CCW operation, λ2 will

lead λ1 instead of lag behind it after the "+GVD" element. The opposite relative delay $+\Delta t = (\lambda 1-\lambda 2) \times (+GVD)$ will cause the phase change to appear at a different tributary (C-1). The pulse broadening introduced by "+GVD" will also be compensated by the "–GVD" element after the nonlinear process, similar to that of the CW operation. The total relative delay between the two demultiplexed channels, C-3 and C-1, is $2\Delta t = 2GVD \times (\lambda 1-\lambda 2)$ and is two times larger than that of the conventional DA-NOLM [40, 44, 63].

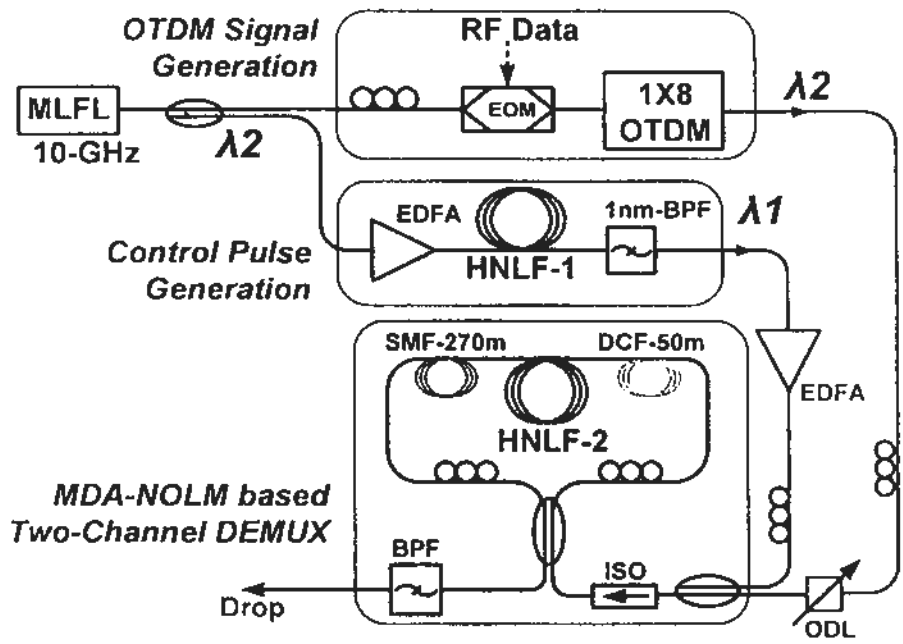

Fig. 4.33 Experimental setup of the 80-to-10 Gb/s DEMUX based on MDA-NOLM. ODL: optical delay line; BPF: band pass filter; ISO: isolator.

The experimental setup for 80-to-10 Gb/s two-channel DEMUX is shown in Fig. 4.33. The 10-GHz mode locked fiber laser (MLFL) generates a pulse train at λ2=1551.9 nm with a pulse width of 2.0 ps. The upper branch of the 10-GHz pulse train at λ2 is used for 80-Gb/s OTDM OOK signal generation through electro-optic modulation (EOM) at 10-Gb/s with a pseudo random binary sequence followed by 1×8 optical multiplication. The lower branch of the 10-GHz pulse train is amplified

to an average power of 23.0 dBm for supercontinuum generation in a highly nonlinear fiber (HNLF-1), which has a nonlinear coefficient of 11.0 $W^{-1}km^{-1}$ at ~1550.0 nm. By spectral slicing with a tunable flat-top band pass filter (BPF) of 1-nm bandwidth, we obtain a widely tunable (1530 nm to 1570 nm) 10-GHz pulsed source with ~4.0 ps pulse width.

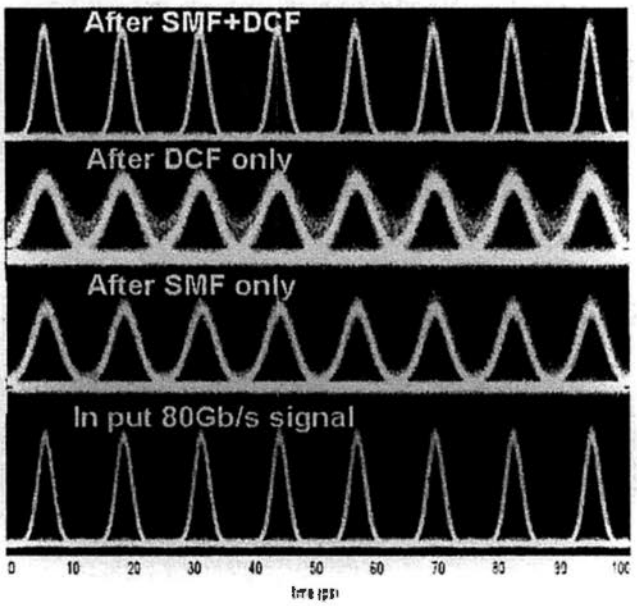

Fig. 4.34 The pulse broadening of the 80-Gb/s OOK signal after transmission of the SMF, DCF and them both.

Fig. 4.34 shows the eye diagrams of the 80-Gb/s signal after propagating in SMF, DCF and them both, indicating the dispersion compensation for minimizing the pulse broadening which enables the operation of the MDA-NOLM.

The 80-Gb/s OTDM OOK signal at λ2 together with the amplified control pulse at λ1 is launched into the MDA-NOLM after an isolator. Inside the MDA-NOLM, we adopt 270-m SMF for "+GVD" and 50-m DCF for "–GVD". The dispersion coefficients of the fibers around 1550 nm are +4.6 ps/nm (270-m SMF) and –4.6 ps/nm (50-m DCF), respectively. The 1-km HNLF-2 has a nonlinear

coefficient of 11.7 $W^{-1}km^{-1}$ and a dispersion coefficient of 0.02 $ps{\cdot}nm^{-1}km^{-1}$ at 1550.0 nm. The XPM process introduces a phase change at two different channels through the CW and CCW operations. Thus, two channels will be switched out in the "drop" port while the other channels are directed to the "through" port.

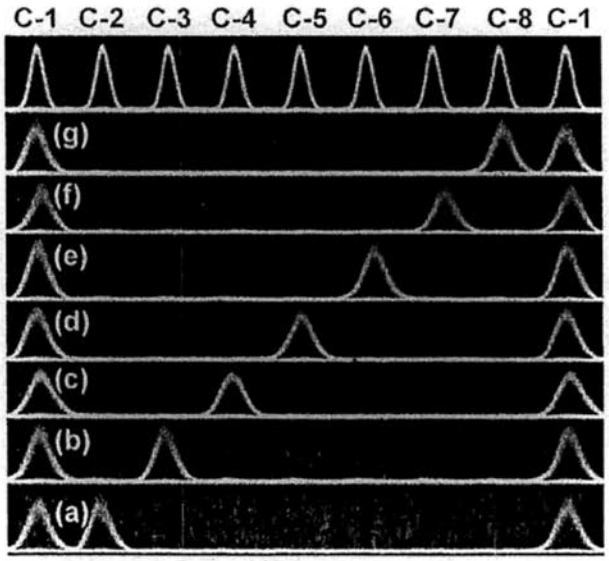

Fig. 4.35 Eye diagrams obtained from the reconfigurable DEMUX.

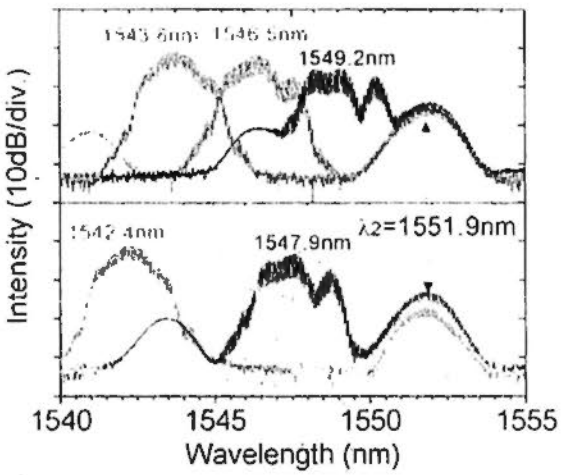

Fig. 4.36 Spectra obtained from the reconfigurable DEMUX.

Fig. 4.35 and Fig. 4.36 show the eye diagrams and the spectra of the input and output signals for two-channel DEMUX of the OTDM signal. The input 80-Gb/s OTDM OOK signal is set at 1551.9 nm and has a pulse width of 3.0 ps. The

frequency bandwidth is 2.0 nm. It is observed that the signal pulse will be broadened to 5.0 ps and 6.8 ps after transmission in 50-m DCF and 270-m SMF, respectively. However, with the DCF and SMF used together, the pulse width is well restored to 3.0 ps, indicating a full compensation of pulse broadening. The two demultiplexed channels have equal pulse width of 4.5 ps.

Table 4.3 Two-channel DEMUX schemes at different control wavelengths λ1. The signal wavelength λ2 is 1551.9 nm

	λ1 (nm)	$\Delta\lambda = \lvert\lambda 1 - \lambda 2\rvert$ (nm)	$\Delta t = 4.6 \times \Delta\lambda$ (ps)	Total relative delay between two channels (ps)	DEMUX channels
A	1549.2	2.7	12.4	24.8	C-1 & C-3
	1546.5	5.4	24.8	49.6	C-8 & C-4
	1543.8	8.1	37.3	74.6	C-7 & C-5
B	1547.9	4.0	18.4	36.8	C-1 & C-4
	1545.2	6.7	30.8	61.6	C-8 & C-5
	1542.4	9.5	43.7	87.4	C-7 & C-6

Table 4.3 shows the two-channel DEMUX schemes at different control wavelengths. For group A, the control pulse overlaps with C-2 before they are launched into the MDA-NOLM. For group B, the control pulse is located at the centre between C-2 and C-3. All tributaries from C-1 to C-8 are demultiplexed with widely open eye diagrams by tuning the optical delay line and the wavelength of the control pulse from 1542.4 nm to 1549.2 nm, as shown in Fig. 4.35 and Fig. 4.36.

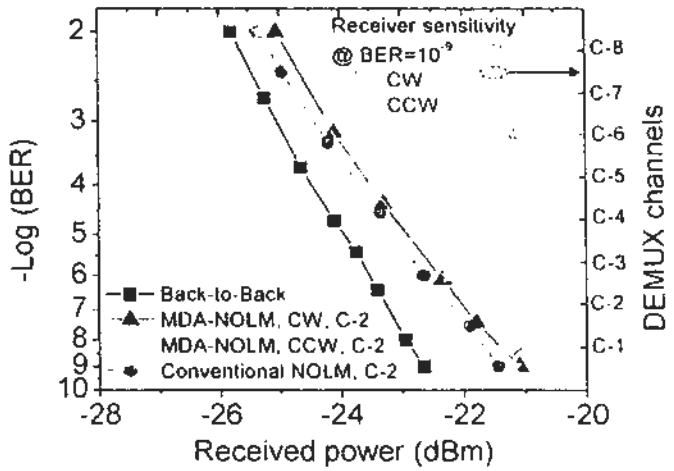

Fig. 4.37 BER measurement results for 80-to-10 Gb/s reconfigurable two-channel DEMUX based on the MDA-NOLM.

Bit error rate measurement is performed based on single channel DEMUX, similar to the work demonstrated in Ref. 24. Notice that the MDA-NOLM is also capable of switchable operation between single channel DEMUX and two channel DEMUX by polarization adjustment. Shown in Fig. 4.37 are the BER results, indicating an error-free DEMUX with performance comparable to the conventional NOLM-based all-optical DEMUX. The receiver sensitivity difference between CW and CCW operations has been improved compared to that of DA-NOLM based DEMUX that depicts a 2-dB difference for operations in the opposite directions [24, 29].

The demonstrated MDA-NOLM reserves the nonlinear imbalanced operation with improved dispersion tolerance. Therefore, MDA-NOLM can be applied to applications for DPSK demodulation, optical regeneration, pulse format conversion and short pulse generation, with improved operation performance.

References

[1]. K. E Stubkjaer, "Technologies for Optical Processing," in Tech. Dig. OFC/NFOEC, San Diego, CA, 2008. Invited tutorial OMV1

[2]. Shigeki, Watanabe, "Optical signal processing using nonlinear fibers," J. Opt. Fiber. Commun. Rep. 3, 1–24 (2005)

[3]. S. Watanabe and F. Futami, "All-optical signal processing using highly-nonlinear optical fibers," IEICE Trans., E84-B, 1179–1189 (2001)

[4]. B. J. Eggleton, S. Radic, and D. J. Moss, "Nonlinear Optics in Communications: From Crippling Impairment to Ultrafast Tools," in Optical Fiber Telecommunications V: Components and Sub-systems, I. P. Kaminow, T. Li, and A. E. Willner, eds. (Academic Press, Oxford, UK, February 2008), Chap. 20. (2008)

[5]. Hirano, M., Nakanishi, T., Okuno, T., Onishi, M., "Silica-Based Highly Nonlinear Fibers and Their Application", IEEE J. Sel. Top. Quantum Electron. **15**, 103 -113, (2009)

[6]. S.Watanabe and F. Futami, "All-opticalwavelength conversion using ultra-fast nonlinearities in optical fiber," IEICE Trans., E85-C, 889–895 (2002).

[7]. J. M. Dudley, "Nonlinear Fibre Optics, New Fibres – New opportunities," presented at the ECOC2007, Tutorial, Berlin, Germany, 16-20 (2007)

[8]. J. M. Dudley and J. R. Taylor, "Ten years of nonlinear optics in photonic crystal fibre," Nat. Photonics 3(2), 85–90 (2009)

[9]. G. P. Agrawal, Nonlinear Fiber Optics, (Academic Press, 2001)

[10]. P. V. Mamyshev, "All-optical data regeneration based on self-phase modulation effect," in Proc. European Conference on Optical Communications (ECOC'98), p. 475. (1998)

[11]. N. Yoshikane, I. Morita, T. Tsuritani, A. Agata, N. Edagawa, and S. Akiba, "Benefit of SPM-based all-optical reshaper in receiver for long-haul DWDM transmission systems," IEEE J. Sel. Top. Quantum Electron. **10**, 412-420 (2004)

[12]. Andreas E. H. Oehler, Simon C. Zeller, Kurt J. Weingarten, and Ursula Keller, "Broad multiwavelength source with 50 GHz channel spacing for wavelength division multiplexing applications in the telecom C band," Opt. Lett., **33**, pp.2158-2160, (2008)

[13]. M. Galili, L. Oxenløwe, H. Mulvad, A. Clausen, and P. Jeppesen, "Optical Wavelength Conversion by Cross-Phase Modulation of Data Signals up to 640 Gb/s," IEEE J. Sel. Top. Quantum Electron. **14**(3), 573–579 (2008)

[14]. Jianping Yao, Fei Zeng, and Qing Wang, "Photonic Generation of Ultrawideband Signals," J. Lightwave Technol. **25**, 3219-3235 (2007)

[15]. J. Li, B. Olsson, M. Karlsson, and P. A. Andrekson, "OTDM Demultiplexer Based on XPM-Induced Wavelength Shifting in Highly Nonlinear Fiber," in Optical Fiber Communication Conference, Technical Digest (Optical Society of America, 2003), paper TuH6. (2003)

[16]. Jie Li, Bengt-Erik Olsson, Magnus Karlsson, and Peter A. Andrekson. "OTDM Add-Drop Multiplexer Based on XPM-Induced Wavelength Shifting in Highly Nonlinear Fiber," J. Lightwave Technol. **23**, 2654- (2005)

[17]. H. Ishikawa, "Ultrafast all-optical signal processing devices", chapter 5, ISBN 978-0-470–51820-5, Wiley (2008)

[18]. K. K. Chow, K. Kikuchi, T. Nagashima, T. Hasegawa, S. Ohara, and N. Sugimoto, "Widely tunable wavelength conversion by four-wave mixing

in 1-m dispersion-shifted Bismuth-Oxide photonic crystal fiber," in Proc. OFC (2007), paper OTul2, (2007)

[19]. G.-W. Lu, K. S. Abedin, T. Miyazaki, "Wavelength Multicasting of DPSK Signals Using Dual-Pump FWM in a Bismuth-Oxide Highly Nonlinear Fiber," in Proc. OFC (2008), paper OMP4, (2008)

[20]. M. P. Fok and C. Shu, "Multipump four-wave mixing in a photonic crystal fiber for 6x10Gb/s wavelength multicasting of DPSK signals," IEEE Photon. Technol. Lett. **19**, 1166-1168 (2007)

[21]. R. Salem, M. A. Foster, A. C. Turner, D. F. Geraghty, M. Lipson, A. L. Gaeta, "Signal regeneration using lowpower four-wave mixing on silicon chip," Nature Photonics **2**, 35-38 (2008)

[22]. K. Croussore, I. Kim, C. Kim, Y. Han, and G. Li, "Phase-and-amplitude regeneration of differential phase-shift keyed signals using a phase-sensitive amplifier," Opt. Express **14**(6), 2085–2094 (2006)

[23]. Guo-Wei Lu and Tetsuya Miyazaki, "Optical phase erasure based on FWM in HNLF enabling format conversion from 320-Gb/s RZDQPSK to 160-Gb/s RZ-DPSK," Opt. Express **17**, 13346-13353 (2009)

[24]. Bill P.-P. Kuo, Evgeny Myslivets, Andreas O. J. Wiberg, Sanja Zlatanovic, Camille-Sophie Brès, Slaven Moro, Faezeh Gholami, Ana Peric, Nikola Alic, and Stojan Radic, "Transmission of 640-Gb/s RZ-OOK Channel Over 100-km SSMF by Wavelength-Transparent Conjugation," J. Lightwave Technol. **29**, 516-523 (2011)

[25]. M. E. Marhic, K. K. Y. Wong, and L. G. Kazovsky, "Wide-band tuning of the gain spectra of one-pump fiber optical parametric amplifiers," IEEE J. Sel. Top. Quantum Electron. **10**, 1133-1141 (2004)

[26]. Kyota Seki and Shinji Yamashita, "Narrowband and tunable optical parametric amplification in Bismuth-Oxide-based highly nonlinear fiber," Opt. Express **16**, 13871-13877 (2008)

[27]. S. Boscolo, S. K. Turitsyn, and K. J. Blow, "Nonlinear loop mirror-based all-optical signal processing in fiber-optic communications," Opt. Fiber Technol. **14**(4), 299–316 (2008)

[28]. T. Yamamoto, E. Yoshida, and M. Nakazawa, "Ultrafast nonlinear optical loop mirror for demultiplexing 640 Gbit/s TDM signals," Electron. Lett. **34**(10), 1013–1014 (1998)

[29]. H. Sotobayashi, C. Sawaguchi, Y. Koyamada and W. Chujo, "Ultrafast walk-off-free nonlinear optical loop mirror by a simplified configuration for 320-Gbit/s time-division multiplexing signal demultiplexing," Opt. Lett. **27** (2002), pp. 1555–1557, (2002)

[30]. Konstantin Kravtsov, Paul R. Prucnal, and Mikhail M. Bubnov, "Simple nonlinear interferometer-based all-optical thresholder and its applications for optical CDMA," Opt. Express **15**, 13114-13122 (2007)

[31]. E.A. Kuzin, B. Ibarra-Escamilla, D.E. Garcia-Gomez and J.W. Haus, "Fiber laser modelocked by the nonlinear polarization rotation Sagnac interferometer," Opt. Lett. **26** (2001), pp. 1559–1561. (2001)

[32]. M.D. Pelusi, Y. Matsui and A. Suzuki, "Pedestal suppression from compressed femtosecond pulses using a nonlinear fiber loop mirror," IEEE J. Quantum Electron. **35**, pp. 867–874. (1999)

[33]. O. Pottiez, B. Ibarra-Escamilla and E.A. Kuzin, "High-quality amplitude jitter reduction and extinction enhancement using a power-symmetric NOLM and a polarizer," Opt. Express **15**, pp. 2564--2572. (2007)

[34]. Yuji Miyoshi, Kensuke Ikeda, Hideaki Tobioka, Takashi Inoue, Shu Namiki, and Ken-ichi Kitayama, "Ultrafast all-optical logic gate using a nonlinear optical loop mirror based multi-periodic transfer function," Opt. Express **16**, 2570-2577 (2008)

[35]. Ivan Glesk, and Paul Prucnal, "Ultrafast operations in all-optical devices for communications networks," **14** January 2008, SPIE Newsroom. (2008) http://spie.org/x19163.xml?ArticleID=x19163

[36]. B. C. Wang, L. Xu, V. Baby, D. Y. Zhou, R. J. Runser, I. Glesk, P. R. Prucnal, "Experimental study on the regeneration capability of the terahertz optical asymmetric demultiplexer," Opt. Commun. **199**, no. 1-4, pp. 83-88, (2001)

[37]. William S. Wong, Shu Namiki, Mordechai Margalit, Hermann A. Haus, and Erich P. Ippen, "Self-switching of optical pulses in dispersion-imbalanced nonlinear loop mirrors," Opt. Lett. **22**, 1150-1152 (1997)

[38]. William S. Wong, Per B. Hansen, Torben N. Nielsen, Mordechai Margalit, Shu Namiki, Erich P. Ippen, Hermann A. Haus, and Life Fellow, "In-Band Amplified Spontaneous Emission Noise Filtering with a Dispersion-Imbalanced Nonlinear Loop Mirror," J. Lightwave Technol. **16**, 1768- (1998)

[39]. Olivier Pottiez, E. Kuzin, B. Ibarra-Escamilla, J. Camas-Anzueto, and F. Gutiérrez-Zainos, "Easily tunable nonlinear optical loop mirror based on polarization asymmetry," Opt. Express **12**, 3878-3887 (2004)

[40]. N. Chi, L. Xu, K. S. Berg, T. Tokle, and P. Jeppesen, "All-optical wavelength conversion and multichannel 2R regeneration based on highly nonlinear dispersion-imbalanced loop mirror," IEEE Photon. Technol. Lett. **14**, 469–471 (2002).

[41]. Nan Chi, Birger Carlsson, and Palle Jeppesen, "2R Regeneration Based on Dispersion-Imbalanced Loop Mirror and Its Applications in WDM Systems," J. Lightwave Technol. **20**, 1809- (2002)

[42]. M. D. Pelusi, Y. Matsui, and A. Suzuki, "Pedestal suppression from compressed femtosecond pulses using a nonlinear fiber loop mirror," IEEE J. Quantum Electron. **35**, 867-874 (1999).

[43]. Shiquan Yang and Xiaoyi Bao, "Generating a high-extinction-ratio pulse from a phase-modulated optical signal with a dispersion-imbalanced nonlinear loop mirror," Opt. Lett. **31**, 1032-1034 (2006)

[44]. Mable P. Fok and Chester Shu, "Delay-asymmetric nonlinear loop mirror for DPSK demodulation," Opt. Lett. **33**, 2845-2847 (2008)

[45]. M. E. Fermann, F. Haberl, M. Hofer, and H. Hochreiter, "Nonlinear amplifying loop mirror," Opt. Lett. **15**, 752-754 (1990)

[46]. S. Boscolo, S. K. Turitsyn, and K. J. Blow, "Nonlinear loop mirror-based all-optical signal processing in fiber-optic communications," Opt. Fiber Technol. **14**(4), 299-316 (2008).

[47]. P. K. A. Wai and Wen-hua Cao, "Ultrashort soliton generation through higher-order soliton compression in a nonlinear optical loop mirror constructed from dispersion-decreasing fiber," J. Opt. Soc. Am. B **20**, 1346-1355 (2003)

[48]. Mohammed Hayder Al-Mansoori and Mohd Adzir Mahdi, "Multiwavelength L-Band Brillouin–Erbium Comb Fiber Laser Utilizing Nonlinear Amplifying Loop Mirror," J. Lightwave Technol. **27**, 5038-5044 (2009)

[49]. O. Pottiez, B. Ibarra-Escamilla and E.A. Kuzin, "High-quality amplitude jitter reduction and extinction enhancement using a power-symmetric NOLM and a polarizer," Opt. Express **15** (2007), pp. 2564- 2572.

[50]. Feng Qu, Xiaoming Liu, Pu Zhang, Xubiao Jiang, Hongming Zhang, and Minyu Yao, "Analysis on the effect of nonlinear polarization evolution in nonlinear amplifying loop mirror," Chin. Opt. Lett. **3**, 669-671 (2005)

[51]. M. P. Fok and C. Shu, "Highly Nonlinear Bismuth-Oxide Fiber Based Dispersion Imbalanced Loop Mirror for Interferometric Noise Suppression," in Optical Fiber Communication Conference and Exposition and The National Fiber Optic Engineers Conference, OSA Technical Digest (CD) (Optical Society of America, 2008), paper OThJ5, (2008)

[52]. Y. Deng, M. P. Fok, and P. R. Prucnal, "Multiple Access Interference and Interferometric Noise Suppression Using Dispersion Imbalanced Loop Mirror in Optical CDMA Networks," in Optical Fiber Communication Conference, OSA Technical Digest (CD), paper OThI4, (2009)

[53]. Y. Deng, K. Thompson, M. P. Fok, and P. R. Prucnal, " Interferometric noise characterization and suppression in optical CDMA networks," IEEE Photon. Technol. Lett. **21**, 981-983 (2009)

[54]. S. Watanabe, "Optical signal processing using nonlinear fibers," J. Opt. Fiber Commun. Rep. 3(1), 1–24 (2006)

[55]. S. Boscolo, S. K. Turitsyn, and K. J. Blow, "Nonlinear loop mirror-based all-optical signal processing in fiber-optic communications," Opt. Fiber Technol. **14**(4), 299–316 (2008)

[56]. T. Yamamoto, E. Yoshida, and M. Nakazawa, "Ultrafast nonlinear optical loop mirror for demultiplexing 640 Gbit/s TDM signals," Electron. Lett. **34**(10), 1013–1014 (1998)

[57]. I. D. Phillips, A. Gloag, P. N. Kean, N. J. Doran, I. Bennion, and A. D. Ellis, "Simultaneous demultiplexing, data regeneration, and clock recovery with a single semiconductor optical amplifier based nonlinear-optical loop mirror," Opt. Lett. **22**(17), 1326–1328 (1997)

[58]. J. H. Lee, T. Tanemura, K. Kikuchi, T. Nagashima, T. Hasegawa, S. Ohara, and N. Sugimoto, "Use of 1-m Bi2O3 nonlinear fiber for 160-Gbit/s optical time-division demultiplexing based on polarization rotation and a wavelength shift induced by cross-phase modulation," Opt. Lett. **30**(11), 1267–1269 (2005)

[59]. M. Roelens, J. A. Bolger, D. Williams, S. Frisken, G. W. Baxter, A. M. Clarke, and B. J. Eggleton, "Flexible and Reconfigurable Time-Domain De-Multiplexing of Optical Signals at 160 Gbit/s," IEEE Photon. Technol. Lett. **21**(10), 618–620 (2009)

[60]. Jiangbing Du, Yongheng Dai, Gordon K. P. Lei, and Chester Shu, "Reconfigurable two-channel demultiplexing using a single baseband control pulse train in a dispersion asymmetric NOLM," Opt. Express **18**, 18691-18696 (2010)

[61]. Jiangbing DU, Yongheng Dai, Gordon K. P. Lei, and Chester Shu, "Dispersion Asymmetric NOLM for Reconfigurable All-optical Two-channel Demultiplexing Using Single Baseband Control Pulse" presented at ECOC2010, paper FM6, Italy, 2010.

[62]. J. Du, Y. Dai, G. K. Lei, H. Wei, and C. Shu, "RZ-to-NRZ and NRZ-to-PRZ Format Conversions Using a Photonic Crystal Fiber Based Mach-Zehnder Interferometer," in Optical Fiber Communication Conference, OSA Technical Digest (CD) (Optical Society of America, 2010), paper OMO4.

[63]. L. Wang, Y. Dai, G. Lei, J. Du, and C. Shu, "All-Optical RZ-to-NRZ and NRZ-to-PRZ Format Conversions Based on Delay- Asymmetric Nonlinear Loop Mirror," IEEE Photon. Technol. Lett. **23**(6), 368-370 (2011)

[64]. Jiangbing Du, Yongheng Dai, Gordon K. P. Lei, and Chester Shu, "Reconfigurable all-optical two-channel demultiplexer based on modified dispersion asymmetric nonlinear optical loop mirror," Electronics Letters **46**, 1613-1614, (2010)

[65]. Jiangbing Du, Yongheng Dai, Gordon K. P. Lei, and Chester Shu, "Reconfigurable All-Optical Two-Channel Demultiplexer based on Modified Dispersion Asymmetric Nonlinear Optical Loop Mirror," presented at Asia Communications and Photonics Conference and Exhibition 2010 (ACP), paper ThB3, Shanghai

Chapter 5: Optical Comb Generation and Clock Recovery

Optical signal processing covers a wide variety of functions that rely on different devices and processing techniques. In order to meet the requests of data traffic speed and system robustness in next generation optical communication networks, one has to look further beyond interferometers for optical signal processing.

In this chapter, we will look into optical comb generation and optical clock recovery based on nonlinear signal processing. Optical comb generation is investigated with the use of nonlinear signal processing techniques to improve the sub-carrier quality. The use of degenerate FWM for chirp magnification is demonstrated in Section 5.1. Additional sub-carriers are generated by the chirp magnification effect. In Section 5.2, an SBS loop mirror is utilized for extinction ratio (ER) enhancement in optical comb generation. Last, optical clock recovery is investigated in Section 5.3 with the use of SBS loop mirror.

5.1 FWM based Chirp Magnifier

Recently, orthogonal frequency division multiplexing (OFDM) has attracted much attention owing to its unmatched performance in spectral efficiency that significantly enhances the optical transmission capacity [1]. An optical OFDM signal consists of multiple sub-carriers to transmit data information. The spectral bands in neighboring sub-carriers may overlap, resulting in channel capacity approaching the fundamental Shannon limit. One of the common approaches to

implement an optical OFDM transmitter is by using a mode-locked laser as the comb source for the generation of un-modulated carriers [2]. Tens of carriers can be generated by spectral broadening of the laser output based on self phase modulation in a highly nonlinear optical fiber (HNLF), which enables the generation of optical OFDM signals with an aggregate bit rate up to terabits per second [3,4]. A fundamental drawback of using a mode-locked laser is the fixed operating frequency determined by the length of the optical cavity, limiting the OFDM transmitter for wideband and bit-rate tunable operations. Also, high quality mode-locked lasers with stable phase and short pulse duration to generate high extinction ratio (ER) sub-carriers are costly and are not readily available.

One can also use phase modulation to generate multiple carriers as a comb source [5]. The advantages offered by phase modulation include bit rate tunability, high stability, and broadband wavelength tuning. However, the number of generated carriers is limited. Usually, a very large driving power or a specially designed low V-π modulator will be required in order to achieve a sufficiently high modulation index.

In this section, we demonstrate a chirp magnification scheme for phase modulated signals based on degenerate four wave mixing (FWM) in a highly nonlinear fiber. The magnification significantly broadens the spectrum at the idler wavelengths and generates additional carriers, which are difficult to be achieved using direct phase modulation. Based on the chirp magnifier, we have obtained a bit-rate tunable optical comb source with 13 carriers for optical OFDM signal generation.

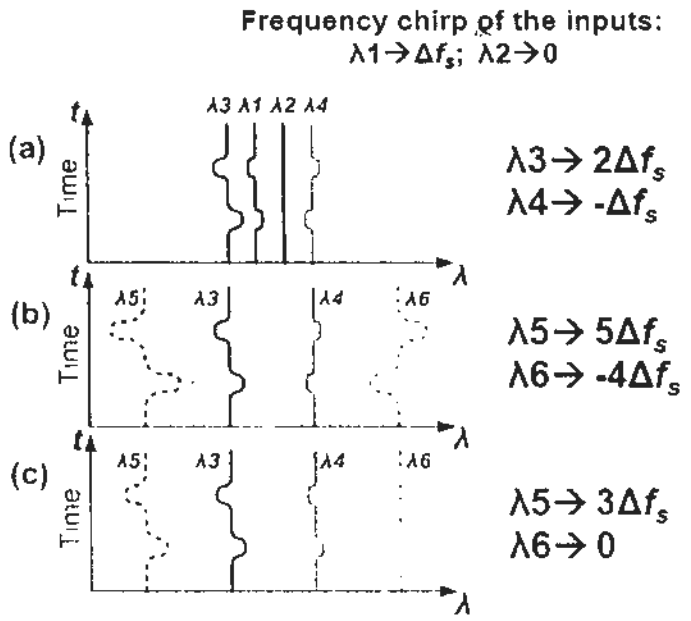

Fig. 5.1 Schematic illustration of the principle of chirp magnification based on degenerate four-wave mixing.

The idler generated in pump-modulated FWM has a doubled phase-modulation index compared to that of the pump wavelength. Therefore, one can use a low modulation voltage to obtain a comparably high modulation index, which thus significantly reduces the required driving power. Hence, phase modulation becomes useful even for modulators with a large V-π [6]. Based on this phenomenon, one can also achieve format conversion for DPSK and DQPSK signals [7-9]. When we consider this phenomenon in the spectral domain, the amount of frequency change in the idler is also doubled in pump-modulated FWM, resulting in a larger spectral width.

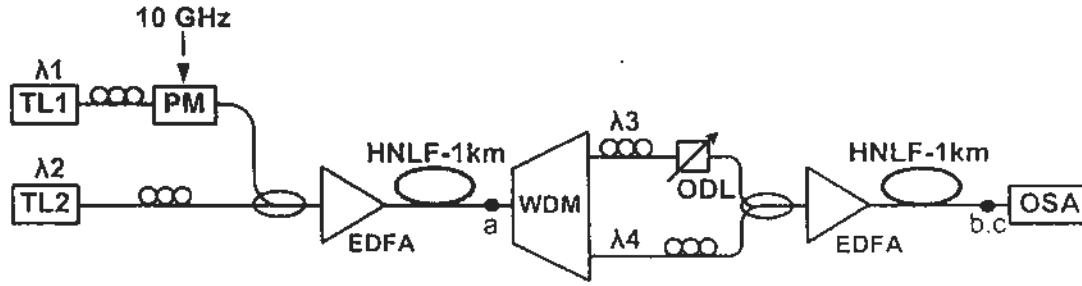

Fig. 5.2 Experimental setup of the chirp magnifier. TL: tunable laser; PM: phase modulator; WDM: wavelength division multiplexer; ODL: optical delay line; EDFA: Erbium-doped fiber amplifier; OSA: optical spectrum analyzer.

Consider phase modulation of an optical carrier at a wavelength λ1. The modulation can be achieved by using a phase modulator with a relatively high modulation index. After the phase modulation, upper and lower sideband components are generated but they are separated in the time domain, as shown in Fig. 5.1(a). Given a modulation index m (which describes how much the modulated variable of the carrier signal varies around its unmodulated level) at a tone modulation frequency f_0, the largest frequency change is given by $\Delta f_m = mf_0$ and the frequency chirp will be $\Delta f_s = mf_0 cos(2\pi f_0 t)$. Along with the magnification of the modulation index m, the chirp will also be magnified.

In a degenerate FWM process with inputs from a continuous wave (CW) laser at λ2 and a chirped carrier at λ1, one can obtain an idler at wavelength λ3=2*λ1-λ2 with doubled modulation index. Hence, the largest frequency change is also doubled. For the other idler wavelength at λ4=2*λ2-λ1, we obtain the same frequency chirp as that of λ1 but with an opposite chirp sign. Subsequently, with λ3 and λ4 directly serve as the FWM inputs, we will obtain λ5=2*λ3-λ4 and λ6=2*λ4-λ3 as the new idlers, as shown in Fig. 5.1(b). The idlers possess even larger spectral widths with 5-times (5X) magnified frequency chirp at λ5 and 4X magnified

frequency chirp at λ6. Meanwhile, we can introduce a half-period delay or an odd multiple of half-period delay between the signals at λ3 and λ4 to obtain the same chirp sign, as shown in Fig. 5.1(c). In this case, λ5 will have 3X magnified chirp and λ6 will ideally become CW light which thus has a zero frequency chirp.

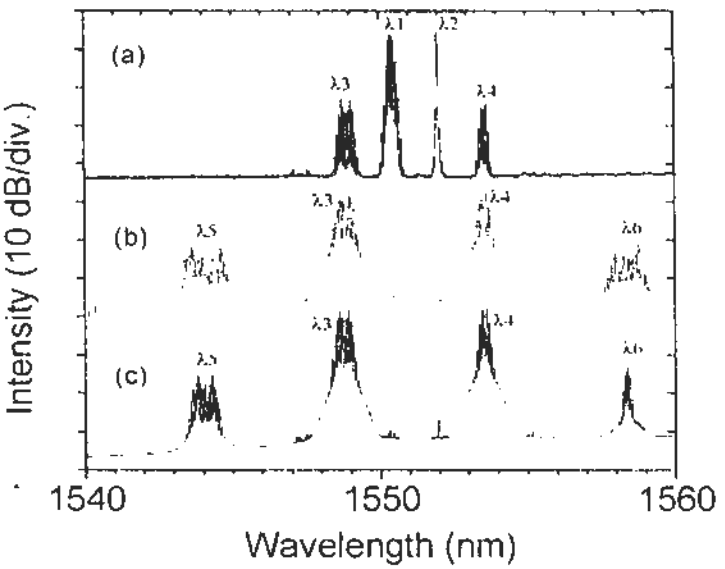

Fig. 5.3 Measured optical spectra after 2 to 5 times chirp magnification. In (b), λ3 and λ4 are relatively delayed by an even multiple of half-period; In (c), λ3 and λ4 are relatively delayed by an odd multiple of half-period.

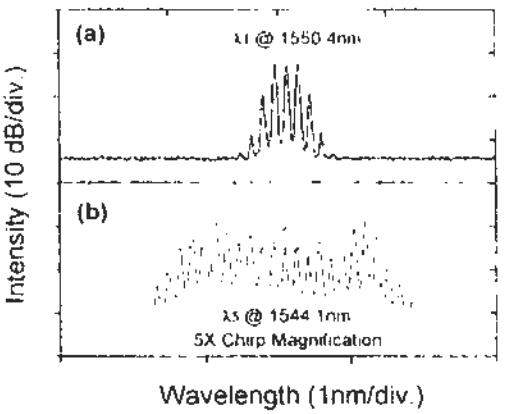

Fig. 5.4 Comparison of the spectra between the originally modulated light at λ1 and the 5X chirp-magnified light at λ5.

Fig. 5.2 shows the experimental setup of the chirp magnifier. λ1 is phase modulated at 10 GHz with a modulation index of ~2π. In the HNLF (all HNLFs used in this work have a nonlinear coefficient of ~11 $km^{-1}W^{-1}$ around 1550 nm), degenerate FWM between λ1 and λ2 results in generated idlers at λ3 and λ4, as shown in Fig. 5.3(a). λ3 has 2X magnified frequency chirp. With λ3 and λ4 serving again as the FWM input, we further obtain idlers at λ5 and λ6. Introducing different relative delays between λ3 and λ4, we can obtain 5X chirp magnification for λ5 and 4X chirp magnification for λ6 as shown in Fig. 5.3(b), or 3X chirp magnification for λ5 as shown in Fig. 5.3(c). Fig. 6.4(a) and Fig. 5.4(b) show the details of the spectra of the original signal at λ1 and that of λ5 with 5X magnified frequency chirp, respectively. The result indicates significant spectral broadening with newly generated sub-carriers after chirp magnification by FWM.

The chirp magnified idlers can serve as an optical comb source for multi-carrier optical OFDM generation.

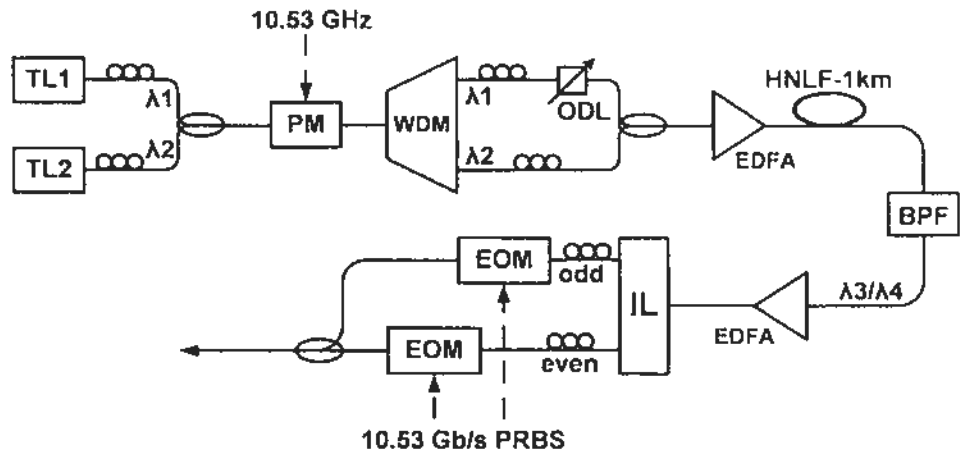

Fig. 5.5 Experimental setup of the chirp magnifier. TL: tunable laser; PM: phase modulator; WDM: wavelength division multiplexer; ODL: optical delay line; IL: interleaver.

The proposed optical chirp magnifier is utilized for generating an optical comb which is applied for OFDM signal generation. The experimental set up is shown in Fig. 5.5. Two continuous waves (CW) at λ1 and λ2 are combined and modulated by a phase modulator. The modulator has a V-π of ~5V, enabling us to generate 5 carriers (within 10-dB bandwidth) for both λ1 and λ2 with a modulation index of ~2π at a frequency of 10.53 GHz. A wavelength division multiplexer (WDM) splits λ1 and λ2 into two branches and a relative delay is introduced between them using a tunable optical delay line. With an odd multiple of a half-period delay (~ 50 ps), the positively chirped portion of the λ1 carrier will overlap with the negatively chirped portion of the λ2 carrier in the time domain. Similarly, the negatively chirped portion of the λ1 carrier will overlap with the positively chirped portion of the λ2 carrier. After the FWM process, two idler wavelengths at λ3 and λ 4 are obtained, each with 3X magnified frequency chirp.

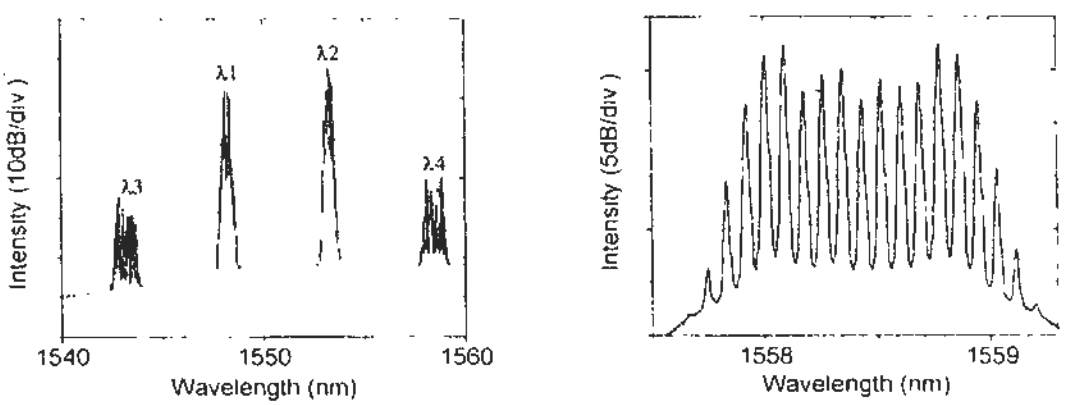

Fig. 5.6 Chirp magnification. (a): FWM spectrum; (b): idler wavelength λ4.

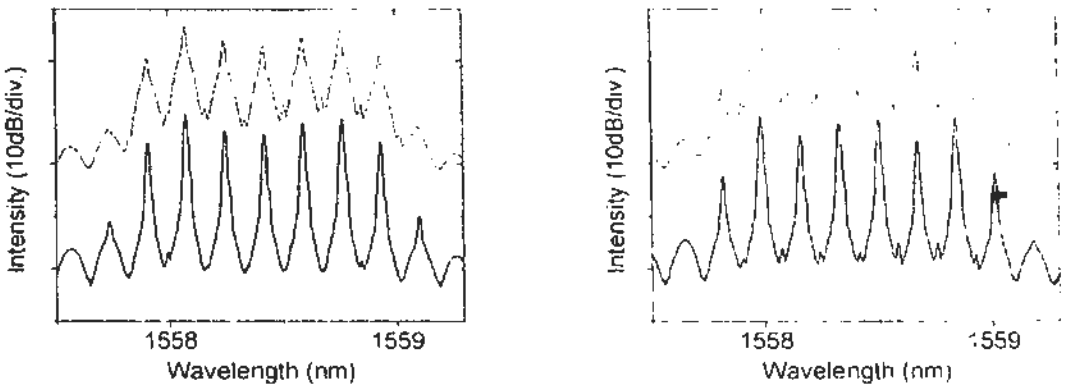

(a) (b)

Fig. 5.7 Optical spectra of the even (a) and odd (b) channels of the comb source before (lower plot) and after (upper plot) modulation.

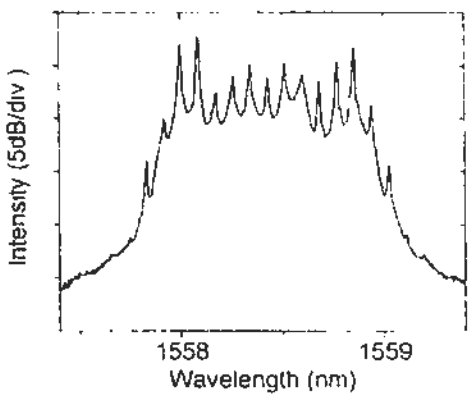

Fig. 5.8 Optical spectrum of the optical OFDM signal at λ4.

Fig. 5.6 shows the spectrum after FWM. The spectral widths of the generated idlers are again larger than those of the inputs. Details of the spectrum at λ4 are shown in Fig. 5.6(b). Within a 10-dB bandwidth, 13 sub-carriers are produced. The average extinction ratio is 18 dB. As an optical comb source, the 3X chirp magnified λ4 is directed to a frequency interleaver. The even and odd carriers are separately modulated. Two electro-optic modulators (EOMs) are used for non-return-to-zero on-off-keying (NRZ-OOK) modulations. The spectra after interleaving and modulation are shown in Fig. 5.7.

Shown in Fig. 5.8 is the spectrum of the 13-channel optical OFDM signals with a base rate of 10.53 Gb/s. The chirp magnifier for optical comb generation is wavelength and bit-rate transparent, offering the advantages of wideband and bit-rate tunable optical OFDM signal generation.

5.2 SBS Loop Mirror for Optical Comb Generation

Optical frequency comb is an ideal multi-carrier light source with precisely and densely spaced periodical and multiple optical channels. The precise and stable frequencies of the optical comb are demanded in applications such as ultra short pulse generation, arbitrary-waveform generation, optical sensing and frequency metrology [10, 11]. The maintained phase and frequency relationship between sub-channels of an optical comb also makes it suitable for coherent wavelength-division multiplexed (WDM) systems [12, 13], orthogonal frequency division multiplexed (OFDM) [14-16], and microwave photonics [17]. Due to the heavy demands, academics and industries have long been trying to generate optical comb sources with variable frequency spacing, high extinction ratio (ER), flat and wideband high power carriers.

There have been several solutions demonstrated for optical comb generation. One of the most widely used techniques is external modulation including electro-optical intensity modulation, phase modulation, asymmetric Mach-Zehnder modulation and recirculation loop with EDFA/SOA [18-20]. Another effective solution is by mode locking of lasers, such as mode-locked laser diodes (MLLD), mode-locked quantum-dot/dash semi-conductor lasers (ML-QDSL) and passively mode-locked Er:Yb: glass oscillators (ERGO) [12, 21, 22]. The external-modulation method has minimal implementation complexity. It is also wavelength and bit-rate

tunable (meaning the variable frequency spacing). The drawbacks are the limited extinction ratio, carrier number and modulation speed (meaning the largest frequency spacing).

Extra effort is usually needed to overcome these limitations, such as nonlinear signal processing based super-continuum generation in high nonlinear optical fibers (HNLF) to increase the carrier number [12]. On the other hand, mode locking method can generate high-repetition-rate pulses with widths shorter than picoseconds. The technique enables us to obtain optical combs with higher ER up to 40 dB and higher repetition rate up to hundreds of GHz, yet with large numbers of carriers and a spectrally flat intensity profile. The bit-rate can even be extended to 427 GHz based on optical signal processing, which is impossible for external modulation method [21]. However, the fixed bit-rate and high cost of the mode-locked lasers make them unattractive for wide use.

In this Section, we demonstrate the use of SBS for optical comb generation. The narrow gain band of SBS enables us to significantly enhance the ER of the optical comb. Meanwhile, the flatness of the comb can also be well improved through gain saturation. A 6-carrier optical comb with an ER of 38 dB and a sub-carrier flatness of 3-dB is obtained from the optical comb source generated by XPM. A 25-dB ER enhancement has been achieved. The whole system is wavelength tunable and bit-rate transparent with minimal implementation complexity. Wideband operation can be expected to generate additional sub-carriers with high ER and improved spectral flatness. Limited by our band pass fiber which has a bandwidth of 4-nm, we have obtained 7 sub-carriers within the bandwidth.

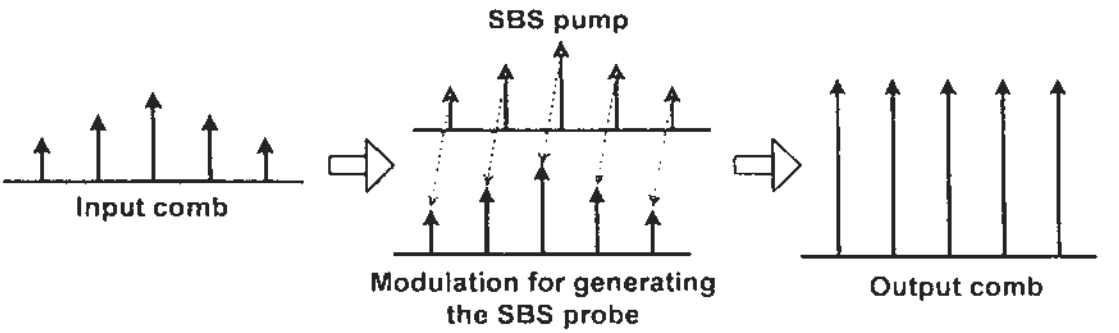

Fig. 5.9 Schematic illustration of the principle of SBS for ER enhancement.

The principle of the ER enhancement by SBS is shown in Fig. 5.9. The input optical comb source has multiple sub-carriers with a small ER. With the carrier power varying significantly from one to another, the optical comb exhibits a poor flatness. By intensity modulation of the input light using an EOM in the SBS loop, one can generate a red-shifted copy of the input comb with a frequency shift equal to the modulation frequency. Therefore, the spectrally shifted copy of the input optical comb will fall within the SBS gain bandwidth and thus act as the SBS probe, provided that the modulation frequency is equal to the Brillouin frequency shift of the HNLF. The narrow gain bandwidth of SBS will amplify the carriers rather than the pedestals which are out of the gain region and thus ER enhancement can be achieved. Meanwhile, due to the saturation of the SBS gain, the flatness of the sub-carriers can also be improved.

Fig. 5.10 shows the experimental setup of the optical comb generator. The tunable laser generates a continuum wave at 1540 nm. The shadowed area is the SBS loop constructed by one 10:90 optical coupler with an EOM, an ISO and 1-km HNLF. There are two HNLFs being used with one for cross phase modulation (XPM) and the other for SBS. The two 1-km HNLFs both have a nonlinear

coefficient of 11 $W^{-1}km^{-1}$ at 1550 nm wavelength. An optical spectral analyzer (OSA) with a resolution of 0.1 nm is used for obtaining the output spectrum.

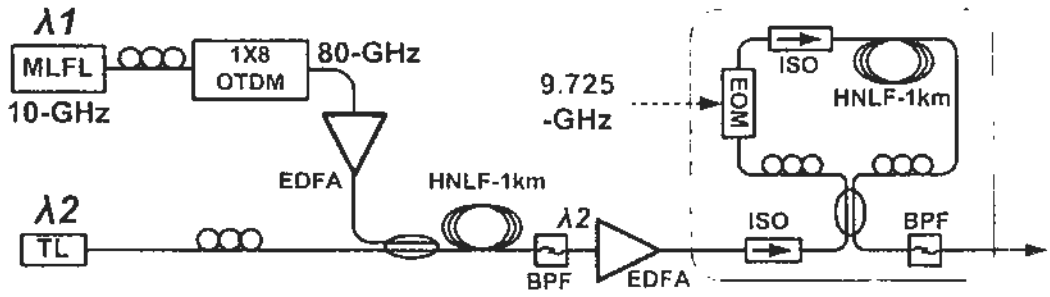

Fig. 5.10 Experimental setup of the 80-GHz optical comb generation. MLFL: mode locked fiber laser; TL: tunable laser; BPF: band pass filter; EOM: electro-optic modulator; ISO: isolator.

The 80-GHz pulse train is obtained by multiplication of 10-GHz pulses with 2-ps width obtained from a MLFL. Since the 10-GHz MLFL is based on active mode locking, the unstable phase of the pulse train results in a spectrum without any clock tones. The 80-GHz output at 1553 nm is then amplified by an EDFA to act as the control for the XPM process. The nonlinear process generates multiple sideband clock tones at the probe wavelength of 1540 nm. Thus, an optical comb source is generated with 80-GHz sub-carrier frequency spacing as shown in Fig. 5.11. A 4-nm BPF after the HNLF filters out the optical comb at 1540 nm.

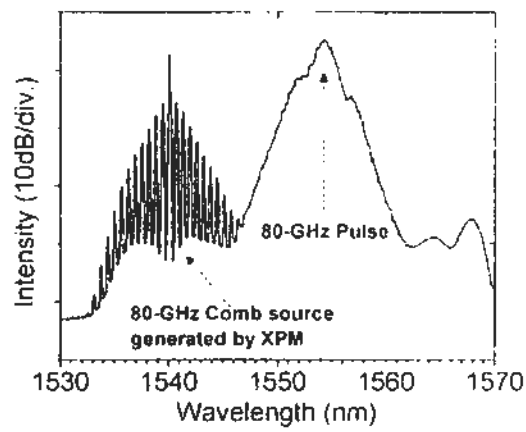

Fig. 5.11 Spectrum measured after applying XPM to generate multiple carriers.

The optical comb is then amplified to an average power of 400 mW by another EDFA before it is launched into the SBS loop mirror. Within the SBS loop mirror, the CCW branch light has 90% of the input power and acts as the SBS pump in the HNLF. The CW branch light with 10% of the input power is intensity modulated by using an EOM at a frequency of 9.725 GHz. The modulation generates sideband carriers (tones) which are shifted by the modulation frequency of 9.725 GHz or its multiples. Since the modulation frequency is equal to the SBS frequency shift, the carriers that are red-shifted by 9.725 GHz fall within the SBS gain region of the CCW pump light. Thus, the narrow gain bandwidth of SBS will provide significant amplification of the carriers rather than the pedestal.

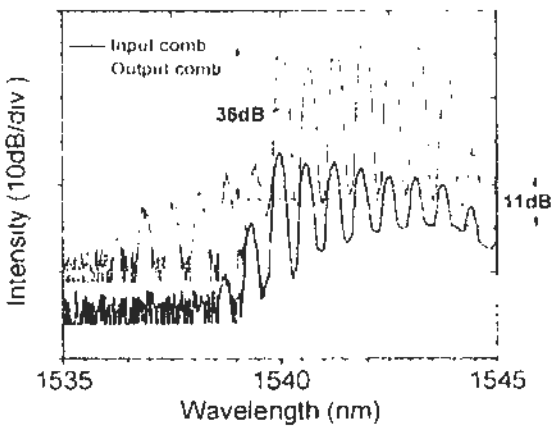

Fig. 5.12 Spectra of the input and output combs indicating the ER enhancement by the SBS loop.

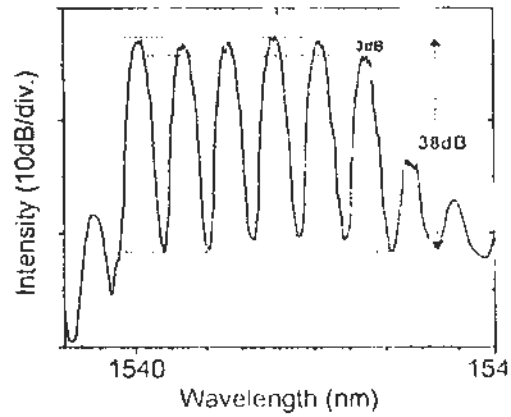

Fig. 5.13 Spectrum of the 6-carrier optical comb with 38-dB ER and 3-dB flatness.

The ER enhancement of the carriers is achieved as shown in Fig. 5.12. The input comb has 9 sub-carriers within the 4-nm bandwidth of the BPF. After the processing by the SBS loop mirror, there are 7 sub-carriers being significantly amplified. An ER of 36 dB is obtained which indicate 25-dB ER enhancement with respect to the input comb. Fig. 5.13 shows the optical comb source with 6 sub-carriers possessing an ER of 38 dB and a flatness of 3-dB. Compared with the input, the flatness improvement is about 4 dB. By using a coupler with a smaller split ratio, such as 20:80 rather 10:90 in this work, one can expect better flatness improvement performance.

The proposed ER enhancement approach is a complementary technology which can be applied to variant of optical comb generation methods, such as the external modulation based optical comb generation approach which is a widely using approach in optical OFDM transmitters. In particular, in order to achieve high speed optical OFDM signal generation, re-circulating loop modulation is frequently used. The technique is recognized as an effective solution for optical comb generation with a large number of high quality sub-carriers [18, 20]. More than one hundred sub-carriers have been obtained for 11.2 Tb/s optical OFDM generation, as

demonstrated by YU *et. al.* [20]. The re-circulating approach enables the generation of a large number of sub-carriers. Unfortunately, the sub-carriers have limited ER due to the use of EDFA and recirculated modulation in the loop. The ER is generally between 20 and 30 dB, which can be well improved by using the proposed SBS loop mirror for ER enhancement. The improved ER will lead to a lower noise level of the optical OFDM signals.

5.3 SBS Loop Mirror for Clock Recovery

Clock recovery (CR) is important in digital communications for providing a synchronous signal, which is highly desirable for logic operation, time-division demultiplexing, pulse format conversion, and retiming in 3R regeneration. Clock recovery can be achieved by using electro-optical phase-locking loop, semiconductor optical amplifier (SOA) ring laser or self-pulsing distributed feedback laser with injection-locking, Fabry-Perot filter (FPF), and stimulated-Brillouin-scattering (SBS) loop [23-27]. Among those techniques, the SBS-based approach has the unique advantage in its transparency to data rate which can be applied to high speed clock recovery up to hundreds of Gigabit/s [30].

OTDM enables the generation of high speed signals up to hundreds of Gb/s. However, time division multiplexing is not favorable for obtaining a strong and stable clock tone due to possible temporal misalignment. The clock tones are particularly unstable for OTDM signals obtained from short pulses generated from mode locked lasers, such as a MLFL, which has unstable phase for the short pulses. Those pulses can only be used for data formats generated with intensity modulation instead of phase modulation.

In this Section 5.2, we have studied the use of an SBS loop mirror for optical comb generation with ER enhancement and flatness improvement. The principle for CR based on SBS scheme is essentially the same as that for optical comb generation. Specifically, SBS loop mirror is applied to high speed OTDM-OOK signals in our work for clock tone extraction.

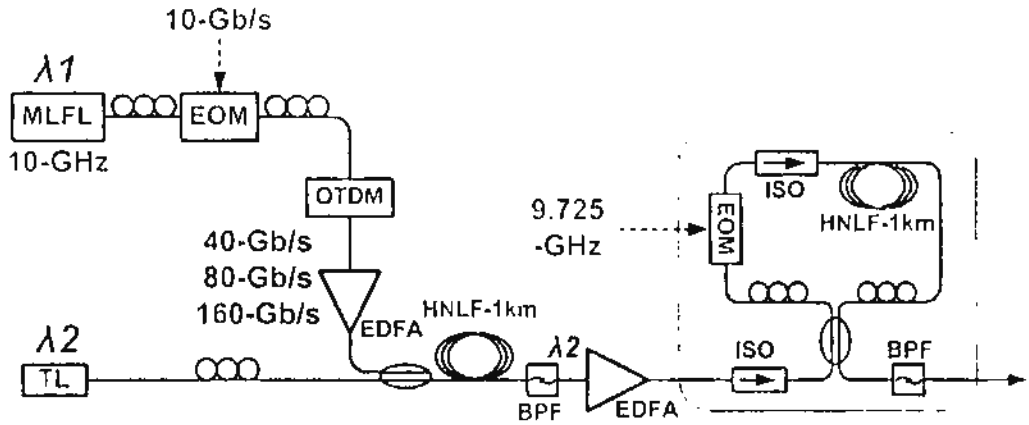

Fig. 5.14 Experimental setup for the 40/80/160 -Gb/s clock recovery. MLFL: mode locked fiber laser; TL: tunable laser; BPF: band pass filter; EOM: electro-optic modulator; ISO: isolator.

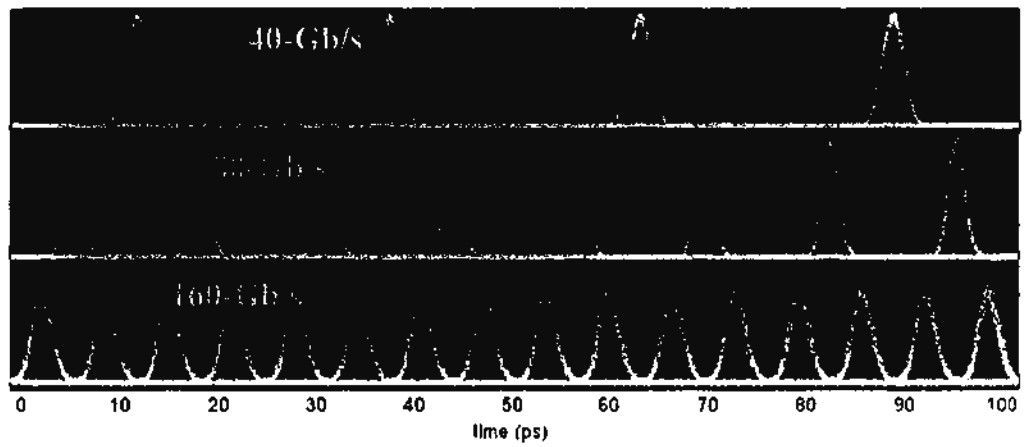

Fig. 5.15 Eye diagrams of the 40/80/160 -Gb/s OTDM-OOK signals.

Fig. 5.14 shows the experimental setup for the clock recovery of 40-Gb/s, 80-Gb/s and 160-Gb/s OTDM signals. The setup is similar to the one for the comb

generation presented in Section 5.2. The phase-unstable short pulses are intensity modulated by 10 Gb/s PRBS data and then multiplexed in time with a factor of two/three/four to obtain 40/80/160 -Gb/s OTDM-OOK signals as shown in Fig. 5.15. The OTDM-OOK signal and the CW probe are launched into a HNLF for XPM to obtain stronger clock tones at the probe wavelength. After passing through a BPF, the probe wavelength with multiple tones are amplified by another EDFA and then directed to an SBS loop mirror for the clock tone extraction.

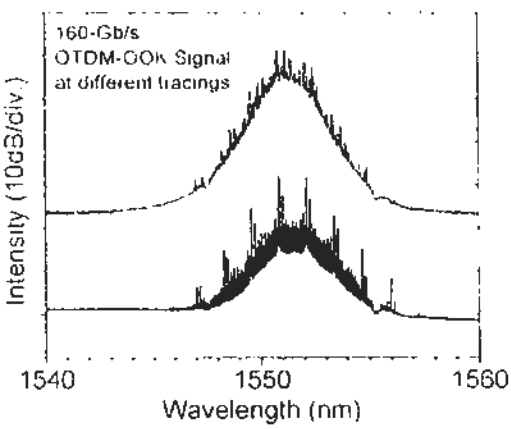

Fig. 5.16 Spectra of the 160-Gb/s OTDM-OOK signal at different tracings indicating the instability of the spectral characteristics.

Fig. 5.16 shows the spectra of the 160-Gb/s OTDM-OOK signal at λ1 around 1551.5 nm. The OTDM signal cannot be utilized directly as the pump in the SBS loop mirror due to unstable phase of the pulses generated from the MLFL. The two spectra in Fig. 5.16 are obtained for the same signal but at different tracings, indicating the varying spectral characteristics with unstable and complex harmonic tones. In order to obtain more stable clock tones, we utilized the XPM process to transform the intensity information of the OTDM-OOK signal to the probe CW wavelength, which is generated by a tunable DFB laser with good coherence. By using a BPF to remove the XPM pump at λ1, we obtain a stabilized spectrum with

enhanced clock tones as shown in Fig. 5.17 (lower). The intensity of the probe output is essentially constant. Notice that one can also recover the intensity information by sideband or center filtering using a BPF with a suitable bandwidth, thus achieving optical wavelength conversion.

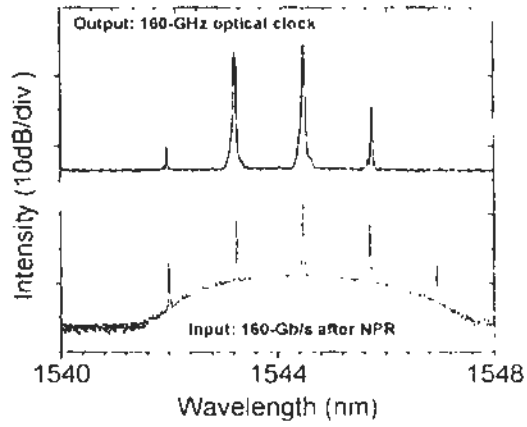

Fig. 5.17 The input and output spectra for 160-Gb/s OTDM-OOK clock recovery.

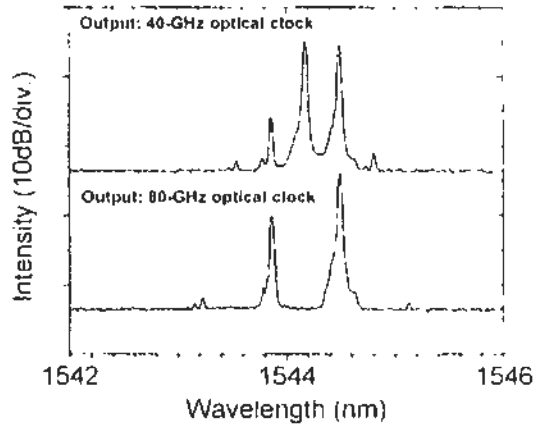

Fig. 5.18 The output spectra for 40 and 80 -Gb/s OTDM-OOK clock recovery.

The input and output spectra for 160-Gb/s OTDM-OOK clock recovery are shown in Fig. 5.17. The input spectrum is obtained after XPM process with a 4-nm BPF. The 160-GHz clock tones are generated with relatively strong carriers which can thus be used as the SBS pump. The power level of the pedestal in the input spectrum indicates the phase/intensity data information of the OOK signal due to

XPM. The clock tones are extracted with the pedestals suppressed and thus the data information is erased, leaving only the clock as shown in the output spectrum. One can also notice the improvement of the ER of the carriers after clock recovery. The same operations are implemented with different data rates of 80-Gb/s and 40-Gb/s. The output optical clock spectra are shown in Fig. 5.18.

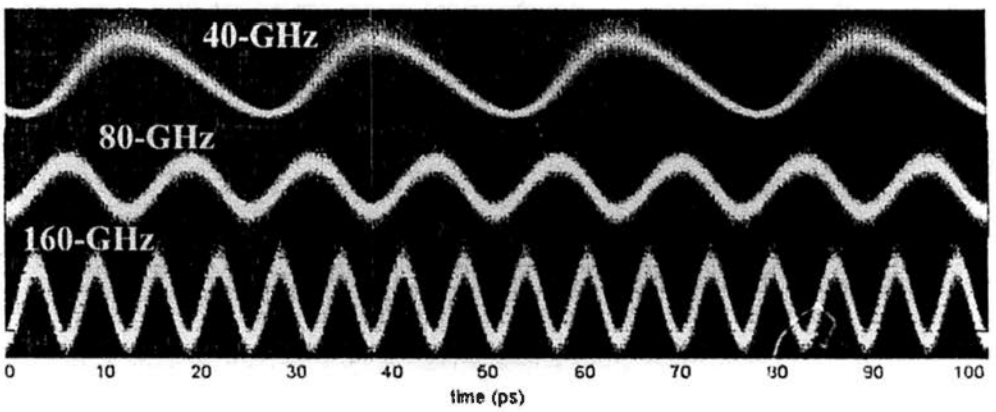

Fig. 5.19 Waveforms of the output pulse trains after clock recovery.

The waveforms shown in Fig. 5.19 are the output pulse trains obtained from the clock recovery scheme. The beating of the clock tones results in a sinusoidal profile of the optical intensity. The timing jitters of the 40-GHz, 80-GHz, and 160-GHz pulse trains are about 510 fs, 400 fs, and 230 fs, respectively. Due to the speed limit of the photodetector, we did not measure the RF spectrum which is usually used for determining the phase noise/jitter of the recovered clock. One can refer to Ref. 31 and Ref. 32 in which the clock recovery for DPSK signals has been achieved based on a similar principle, yet performed at lower data rates with measured output RF spectra.

References

[1]. J. Armstrong, "OFDM for Optical Communications," J. Lightwave Technol., **27**, pp.189-204, (2009)

[2]. D. Hillerkuss, M. Winter, M. Teschke, A. Marculescu, J. Li, G. Sigurdsson, K. Worms, S. Ben Ezra, N. Narkiss, W. Freude, and J. Leuthold, "Simple all-optical FFT scheme enabling Tbit/s real-time signal processing," Opt. Express, **18**, pp.9324-9340, (2010)

[3]. Andreas E. H. Oehler, Simon C. Zeller, Kurt J. Weingarten, and Ursula Keller, "Broad multiwavelength source with 50 GHz channel spacing for wavelength division multiplexing applications in the telecom C band," Opt. Lett., **33**, pp.2158-2160, (2008)

[4]. D. Hillerkuss, et al., "Single source optical OFDM transmitter and optical FFT receiver demonstrated at line rates of 5.4 and 10.8 Tbit/s," Proc. OFC '10, San Diego, USA, paper PDPC1, (2010)

[5]. K. Takiguchi, M. Oguma, H. Takahashi and A. Mori, "Integrated-optic eight-channel OFDM demultiplexer and its demonstration with 160 Gbit/s signal reception," Electron. Lett., **46**, pp.575--576, (2010)

[6]. Y. Gao, Y. Xie, and S. He, "Reducing the driving voltage of a phase modulator with cascaded four-wave-mixing processes," J. Opt. Soc. Am. B, **27**, pp.2360-2364, (2010)

[7]. G. Lu, K. Abedin, and T. Miyazaki, "All-optical RZ-DPSK WDM to RZ-DQPSK phase multiplexing using four-wave mixing in highly nonlinear fiber," IEEE Photon. Technol. Lett., **19**, pp.1699-1701, (2007)

[8]. Y. Gao, L. Xu, S. Gao, and S. He, "Optical ASK-DPSK and QAM Signal Generation Using FWM in High Nonlinearity Fiber (HNLF)," in Optical

Fiber Communication Conference, OSA Technical Digest (CD) (Optical Society of America, 2011), paper OML6, (2011)

[9]. Guo-Wei Lu and Tetsuya Miyazaki, "Optical phase erasure based on FWM in HNLF enabling format conversion from 320-Gb/s RZDQPSK to 160-Gb/s RZ-DPSK," Opt. Express **17**, 13346-13353 (2009)

[10]. Z. Jiang, C.-B. Huang, D. E. Leaird, and A. M. Weiner, "Optical arbitrary waveform processing of more than 100 spectral comb lines," Nat. Photonics **1**, 463-467 (2007)

[11]. Scott A. Diddams, David J. Jones, Long-Sheng Ma, Steven T. Cundiff, and John L. Hall, "Optical frequency measurement across a 104-THz gap with a femtosecond laser frequency comb," Opt. Lett. **25**, 186-188 (2000)

[12]. Andreas E. H. Oehler, Simon C. Zeller, Kurt J. Weingarten, and Ursula Keller, "Broad multiwavelength source with 50 GHz channel spacing for wavelength division multiplexing applications in the telecom C band," Opt. Lett. 33, 2158-2160 (2008)

[13]. A.D. Ellis, and F.C.G. Gunning, "Spectral Density Enhancement Using Coherent WDM", IEEE Photon. Technol. Lett., **17**, 504-506 (2005)

[14]. N. Dupuis, C. R. Doerr, L. Zhang, L. Chen, N. J. Sauer, L. Buhl, and D. Ahn, "InP-based comb generator for optical OFDM," in National Fiber Optic Engineers Conference, OSA Technical Digest (CD) (Optical Society of America, 2011), paper PDPC8 (2011)

[15]. Xingwen Yi, Nicolas K. Fontaine, Ryan P. Scott, and S. J. Ben Yoo, "Tb/s Coherent Optical OFDM Systems Enabled by Optical Frequency Combs," J. Lightwave Technol. **28**, 2054-2061 (2010)

[16]. I. Morohashi, T. Sakamoto, N. Yamamoto, H. Sotobayashi, T. Kawanishi, and I. Hosako, "1 THz-Bandwidth Optical Comb Generation using Mach-Zehnder-Modulator-Based Flat Comb Generator with Optical Feedback Loop," in Optical Fiber Communication Conference, OSA Technical Digest (CD) (Optical Society of America, 2011), paper JThA029 (2011)

[17]. Shuko Yokoyama, Ryotaro Nakamura, Masaki Nose, Tsutomu Araki, and Takeshi Yasui, "Terahertz spectrum analyzer based on a terahertz frequency comb," Opt. Express **16**, 13052-13061 (2008)

[18]. Y. Ma, Q. Yang, Y. Tang, S. Chen, and W. Shieh, "1-Tb/s Single-Channel Coherent Optical OFDM Transmission With Orthogonal-Band Multiplexing and Subwavelength Bandwidth Access", IEEE, J. Lightwave Technology, vol. **28**, no.4, (2010)

[19]. T. Sakamoto, T. Kawanishi and M. Izutsu, "Widely wavelength-tunable ultra-flat frequency comb generation using conventional dual-drive Mach-Zehnder modulator", Electronics Letters, vol. **43**, no. 19, 2007, pp.1039-1040, (2007)

[20]. J. Yu, Z. Dong, and N. Chi, "Generation, Transmission and Coherent Detection of 11.2 Tb/s (112x100Gb/s) Single Source Optical OFDM Superchannel," in National Fiber Optic Engineers Conference, OSA Technical Digest (CD) (Optical Society of America, 2011), paper PDPA6 (2011)

[21]. Marcia Costa e Silva, Alexandra Lagrost, Laurent Bramerie, Mathilde Gay, Pascal Besnard, Michel Joindot, Jean-Claude Simon, Alexandre Shen, and Guan-Hua Duan, "Up to 427 GHz All Optical Frequency Down-Conversion

Clock Recovery Based on Quantum-Dash Fabry–Perot Mode-Locked Laser," J. Lightwave Technol. **29**, 609-615 (2011)

[22]. Xuefeng Tang, Sung Han Chung, Abdullah S. Karar, John C. Cartledge, Alexandre Shen, and Guang-Hua Duan, "Spectral Filtering Characteristics of a Quantum-Dash Fabry-Pérot Laser and Its Implications on 40 Gb/s XPM Based Optical Retiming Performance," J. Lightwave Technol. **29**, 31-36 (2011)

[23]. C.Boerner, V. Marembert, S. Ferber, C. Schubert, C. Schmidt-Langhorst, R. Ludwig, and H. G. Weber, "320 Gbit/s clock recovery with electro-optical PLL using a bidirectionally operated electroabsorption modulator as phase comparator," in Optical Fiber Communication Conference, OSA Technical Digest (CD) (Optical Society of America, 2003), paper OTuO3 (2003)

[24]. K. Vlachos, G. Theophilopoulos, A. Hatziefremidis, and H. Avramopoulos, "30 Gbps, broadly tunable, all-optical clock recovery circuit," in Optical Fiber Communication Conference, OSA Technical Digest (CD) (Optical Society of America, 2000), paper ThP2-1 (2000)

[25]. Y. Li, C. Kim, G. Li, Y. Kaneko, R. L. Jungerman, and O. Buccafusca, "Wavelength and polarization insensitive all-optical clock recovery from 96-Gb/s data by using a two-section gain-coupled DFB laser," IEEE Photon. Technol. Lett. **15**, 590-592 (2003)

[26]. G. Contestabile, A. D' Errico, M. Presi, and E. Ciaramella, "40-GHz all-optical clock extraction using a semiconductor-assisted Fabry-Perot filter," IEEE Photon. Technol. Lett. **16**, 2523-2525 (2004)

[27]. D. L. Butler, J. S. Wey, M. W. Chbat, G. L. Burdge, and J. Goldhar, "Optical clock recovery from a data stream of an arbitrary bit-rate by use of stimulated Brillouin scattering," Opt. Lett. **20**, 560-562 (1995)

[28]. W. W. Tang, M. P. Fok, and C. Shu, "All-optical clock recovery from NRZ data using a NRZ-to-PRZ converter constructed with a polarization-maintaining fiber loop mirror filter," in Conference on Lasers and Electro-Optics/Pacific Rim, (Optical Society of America, 2005), paper CThM1-2 (2005)

[29]. Y. Yu, X. Zhang, E. Zhou, and D. Huang, "All-optical clock recovery from NRZ signals at different bit rates via preprocessing by an optical filter," IEEE Photon. Technol. Lett. **19**, 2039-2041 (2007)

[30]. X. Zhou, H. H. M. Shalaby, C. Lu, T. H. Cheng, and P. Ye, "A performance analysis of all-optical clock extraction circuit based on stimulated Brillouin scattering," J. Lightw. Technol. **18**, 1453-1466 (2000)

[31]. Y. Dai, J. Du, G. K. P. Lei, and C. Shu, "Wideband clock recovery for NRZ-DPSK signals," in Asia Communications and Photonics Conference and Exhibition (ACP), 2010, 395, 8-12 Dec. 2010, Shanghai (2010)

[32]. Y. Dai, G. K. P. Lei, J. Du, C. Shu, and M. P. Fok, "Bit-rate tunable clock recovery of NRZ-DPSK signal based on delay-asymmetric nonlinear loop mirror and stimulated Brillouin scattering loop," in Optical Fiber Communication Conference, OSA Technical Digest (CD) (Optical Society of America, 2010), paper OMT3 (2010)

Chapter 6: Summary and Future Work

6.1 Thesis Summary

Optical signal processing achieved with interferometers covers a wide range of applications in optical communications. This thesis presents an extensive study of the processing techniques based on passive and active fiber devices, including several innovative fiber interferometers.

In Chapter 1, we discussed the trend for the growth of next-generation optical communications. We also provided a review of optical communication history, and overview of optical signal processing and interferometers for fiber communications.

In Chapter 2, we described the fabrication of a photonic crystal fiber based Mach-Zehnder interferometer (PCF-MZI). Its applications in optical signal processing are experimental studied. Included are DPSK demodulation, pulse format conversion, repetition rate multiplication as well as high speed OTDM signal generation. Table 1 lists several major interferometers and their properties as the comparison of the PCF-MZI to the other interferometers. PCF-MZI is one of the all-fiber in-line modal interferometers, which only utilizes one line of fiber, and makes the fabrication easy and precise, with a good precision tolerance. The modal index difference is usually quite large and thus makes the device usually compact. The cost of PCF-MZI is very low, compared with waveguide or free-space devices. Conventional fiber coupler based interferometer is also easy for fabrication but difficult for precise control with usually a worse tolerance of fabrication precision. The fabrication is usually more difficult for high speed operation. Waveguide and

free-space based interferometer's fabrication is usually expensive but the operation performance is comparably good especially for high speed operations.

Table 6.1 Comparison of the PCF-MZI to the other interferometers

In-line all-fiber modal interferometer			
Device type	Interference modes	Delay coefficient	Operation performance
PCF-MZI [1, 2]	Core-mode/ cladding mode	Large (e.g. 30ps/m)	Wide band, high ER, large loss, stable
Two-mode fiber [3]	Fundamental/ high-order core-modes	Large	Wide band, high ER, small loss, stable
Sagnac/Loyt [4]	Two polarization modes	Small (e.g. 1ps/m)	Wide band, high ER, small loss, instable
Hollow core fiber [5]	Air/silica modes	Very large (e.g. 1500ps/m)	Narrow band, small ER, small loss, stable

Two-arm interferometers		
Device type	Operation performance	Fabrication and cost
Fiber coupler pair	Wide band, high ER, small loss, stable	Easy fabrication, low precision, low cost
Waveguide	Wide band, high ER, small loss, instable	Difficult fabrication, high precision, high cost
Free-space	Wide band, high ER, small loss, stable	Easy fabrication, high precision, high cost

OFDM is an attractive solution in next-generation communications for long haul transmission and optical access. Cascaded delay interferometers can be used in optical OFDM demultiplexing, which has been introduced in Chapter 3. Cascaded and multisection Sagnac interferometers are studied theoretically and experimentally in this chapter. Designs of optical OFDM demultiplexers are demonstrated based on cascaded and multisection Sagnac interferometers. Optical demultiplexing of OFDM signals has been experimentally investigated.

In Chapter 4, we first introduced the nonlinear effects in optical fibers, including self-phase modulation, cross phase modulation, four wave mixing, and optical parametric amplification. Nonlinear optical loop mirrors (NOLM) as active and nonlinear interferometers are also introduced in this chapter. Dispersion asymmetric NOLM, as a variant of NOLM, has then been investigated in Chapter 4.

Reconfigurable OTDM demultiplexing is demonstrated based on the DA-NOLM. Two-channel optical DEMUX using a single baseband control pulse train is achieved for 40 Gb/s OTDM signals. A modified configuration of DA-MOLM is presented with dispersion management inside the loop mirror. Reconfigurable two-channel DEMUX of 80 Gb/s OTDM signals is demonstrated. Other applications of DA-NOLM for DPSK demodulation, repetition rate multiplication, and pulse format conversion are also discussed.

Table 6.2 Comparison of the (M)DA-NOLM to the other OTDM demultiplexers

OTDM optical demultiplexers			
Device type	Operation principle	Demultiplexing wavelength	Bandwidth
EOM/EAM [6]	Linear E-O modulation	Preserved	Wideband
NOLM	Nonlinear XPM	Preserved	Wideband
FWM/OPA	Nonlinear	Converted	Limited bandwidth
UNI [7]	Nonlinear XPM	Preserved	Wideband
TOAD [8]	Nonlinear XPM in SOA	Preserved	Wideband
PPLN [9]	Nonlinear SFG/DFG	Converted	Limited bandwidth
DA-NOLM	Nonlinear XPM	Preserved	Wideband
MDA-NOLM	Nonlinear XPM	Preserved	Wideband

Compared with several major OTDM optical demultiplexers, DA-NOLM and MDA-NOLM inherit all the advantages of NOLM and particularly they have such an unique advantage of two-channel operation capability, which doubles the demultiplexing efficiency. The single-channel/two-channel switchable operation also increases the flexibility of the system. The reconfigurable operation of DA-NOLM and MDA-NOLM is based on wavelength detuning for OTDM tributary selection, which is also different compared to the other demultiplexers, as list in

Table 6.2. The nonlinear process of XPM in DA-NOLM and MDA-NOLM indicates the ultrafast operation capability, rather than electric-optical demultiplexers such as EOM and EAM which has such an electronic bottleneck, or the SOA based demultiplexer like TOAD which has limited speed due to the patterning effect. DA-NOLM and MDA-NOLM are also capable of ADM with two-channel operation rather than TOAD which will destroy the through channels.

In Chapter 5, optical comb generation and clock recovery are studied based on nonlinear signal processing techniques. Degenerate four wave mixing (FWM) is utilized for chirp magnification to generate an optical comb with improved number of sub-carriers Based on a stimulated Brillouin scattering (SBS) loop mirror, we demonstrated the generation of improved optical combs with enhanced extinction ratio and flatness. Bit-rate variable optical clock recovery for OTDM signals has also been experimentally studied.

6.2 Future Work

This thesis covers the study of a variety of fiber devices for optical signal processing with emphasis over several innovative fiber interferometers based on PCF-MZI, Sagnac interferometer and NOLM. Continuous effort is requested to improve the performance for optical signal processing, particularly along with the recent developments such as space division multiplexing and mode division multiplexing. Here below lists several suggested directions for future work and the outlook.

The PCF-MZI presented in this thesis is an in-line modal interferometer. One advantage of using PCF is the flexible structure and innovative guidance mechanisms. There have been several demonstrations of PCF with specially

designed structures which can favor the applications of constructing in-line modal interferometers, e.g., reducing the insertion loss and polarization dependence. Apart from PCF, one can also utilize two-mode fiber or few-mode fiber to achieve modal interference between the low-order core modes [10, 11]. Applications for optical signal processing can be improved with the improvements of the modal interferometer by using these specialty fibers. For example, with reduced insertion loss, cascaded stages of in-line interference can be implemented and thus optical OFDM DEMUX can be achieved.

The SBS frequency shift is wavelength dependent, which may limit the wideband operation for ER enhancement for optical comb generation. Further investigation is requested to explore the SBS loop mirror for generating additional high-ER sub-carriers, rather than 7 carriers presented in this thesis for the 80-GHz optical comb.

By using chirp magnifier and SBS loop mirror for improved optical comb generation, we will continue the study about optical OFDM generation and its signal processing. Multi-carrier optical OFDM signals, as a super-channel, also need wavelength conversion for data routing. All-optical wavelength conversion is particularly desired for optical OFDM signals due to the limited speed and complexity of OEO conversion for OFDM receiver. Thus, one can utilize optical nonlinear effects for wavelength conversion. Since the optical OFDM signal has an analog waveform, FWM would be an appropriate approach. The ultrafast nonlinear response can also be utilized for optical gating in optical OFDM DEMUX in which a narrow gating window is particularly required for sampling.

Recently, mode division multiplexing (MDM) has become an eye-catching technology which is recognized as another effective solution to further increase the

transmission capacity [12]. This idea utilizes the orthogonality of the eigen-modes supported by the few-mode fibers, e.g. two-mode and three-mode fibers, so that different messages can be carried by different modes without noticeable modal interference [13]. The principle is similar to OFDM which utilizes the orthogonality of the frequency carriers to prevent interference between the overlapped spectra. The modal multiplexing, signal transmission, modal demultiplexing, and other signal processing techniques in MDM systems still require tremendous efforts. Modal devices based on two-mode or few-mode fibers, such as modal interferometers, can be used for WDM DEMUX. At the same time, a FBG inscribed on a two-mode fiber will have two resonant wavelengths correspond to the two modes supported by the fiber [13]. Thus, such a FBG can be used for simultaneous WDM and MDM demultiplexing. Mode multiplexing can also be achieved. It is anticipated that the all-fiber structure can result in a better performance in insertion loss, stability, and compactness, compared with the free space or liquid crystal based devices [14].

Reference

[1]. J. Du, Y. Dai, G. K. Lei, H. Wei, and C. Shu, "RZ-to-NRZ and NRZ-to-PRZ Format Conversions Using a Photonic Crystal Fiber Based Mach-Zehnder Interferometer," in Optical Fiber Communication Conference, OSA Technical Digest (CD) (Optical Society of America, 2010), paper OMO4 (2010)

[2]. Jiangbing Du, Yongheng Dai, Gordon K. P. Lei, Weijun Tong, and Chester Shu, "Photonic crystal fiber based Mach-Zehnder interferometer for DPSK signal demodulation," Opt. Express **18**, 7917-7922 (2010)

[3]. Q. Li, C.-H. Lin, P.-Y. Tseng, and H. P. Lee, "Demonstration of high extinction ratio modal interference in a two-mode fiber and its applications for all-fiber comb filter and high-temperature sensor," Opt. Commun. **250**(4-6), 280–285 (2005)

[4]. Do-Hyun Kim and Jin Kang, "Sagnac loop interferometer based on polarization maintaining photonic crystal fiber with reduced temperature sensitivity," Opt. Express **12**, 4490-4495 (2004)

[5]. Y. Jung, S. Lee, B. H. Lee, and K. Oh, "Ultracompact in-line broadband Mach-Zehnder interferometer using a composite leaky hollow-optical-fiber waveguide," Opt. Lett. **33**, 2934-2936 (2008)

[6]. M. D. Pelusi, "160-Gb/s Optical Time-Division Demultiplexing Using a Mach- Zehnder Modulator in a Fiber Loop," IEEE Photon. Technol. Lett., **20**, pp. 1060 - 1062, (2008)

[7]. Naimish S. Patel, Katherine L. Hall, and Kristin A. Rauschenbach, "Interferometric All-Optical Switches for Ultrafast Signal Processing," Appl. Opt. **37**, 2831-2842 (1998)

[8]. Ivan Glesk, and Paul Prucnal, "Ultrafast operations in all-optical devices for communications networks," 14 January 2008, SPIE Newsroom. (2008)

[9]. Hans-Georg Weber, Reinhold Ludwig, Sebastian Ferber, Carsten Schmidt-Langhorst, Marcel Kroh, Vincent Marembert, Christof Boerner, and Colja Schubert, "Ultrahigh-Speed OTDM-Transmission Technology," J. Lightwave Technol. **24**, 4616-4627 (2006).

[10]. Q. Li, C.-H. Lin, P.-Y. Tseng, and H. P. Lee, "Demonstration of high extinction ratio modal interference in a two-mode fiber and its applications for all-fiber comb filter and high-temperature sensor," Opt. Commun. **250**(4-6), 280–285 (2005)

[11]. F. Gérôme, J.-L. Auguste, and J.-M. Blondy, "Design of dispersion-compensating fibers based on a dual-concentric-core photonic crystal fiber," Opt. Lett. **29**, 2725-2727 (2004)

[12]. N. Hanzawa, K. Saitoh, T. Sakamoto, T. Matsui, S. Tomita, and M. Koshiba, "Demonstration of mode-division multiplexing transmission over 10 km two-mode fiber with mode coupler," in Optical Fiber Communication Conference, OSA Technical Digest (CD) (Optical Society of America, 2011), paper OWA4

[13]. Dae Seung Moon, Un-Chul Paek, and Youngjoo Chung, "Multi-wavelength lasing oscillations in an erbium-doped fiber laser using few-mode fiber Bragg grating," Opt. Express **12**, 6147-6152 (2004)

[14]. Fumiya Saitoh, Kunimasa Saitoh, and Masanori Koshiba, "A design method of a fiber-based mode multi/demultiplexer for mode-division multiplexing," Opt. Express **18**, 4709-4716 (2010)

Publication List

Journal paper

[1]. **Jiangbing DU**, Yongheng Dai, Gordon K. P. Lei, and Chester Shu, "Reconfigurable two-channel demultiplexing using a single baseband control pulse train in a dispersion asymmetric NOLM" Opt. Express **18**, 18691-18696 (2010)

[2]. **Jiangbing DU**, Yongheng Dai, Gordon K. P. Lei, Weijun Tong, and Chester Shu, "Photonic crystal fiber based Mach-Zehnder interferometer for DPSK signal demodulation" Opt. Express **18**, 7917-7922 (2010)

[3]. **Jiangbing Du**, Yongheng Dai, Gordon K. P. Lei, and Chester Shu, "Reconfigurable all-optical two-channel demultiplexer based on modified dispersion asymmetric nonlinear optical loop mirror," Electronics Letters **46**, 1613-1614, (2010)

[4]. L. Wang, Y. Dai, G. Lei, **J. Du**, and C. Shu, "All-Optical RZ-to-NRZ and NRZ-to-PRZ Format Conversions Based on Delay- Asymmetric Nonlinear Loop Mirror," IEEE Photon. Technol. Lett. **23**(6), 368 - 370 (2011)

[5]. Y. Dai, **J. Du**, X. Fu, G. K. P. Lei, and C. Shu, "Ultrawideband monocycle pulse generation based on delayed interference of $\pi/2$ phase-shift keying signal," Opt. Lett. **36**, 2695-2697 (2011)

[6]. Gordon K. P. Lei, Yongheng Dai, **Jiangbing Du**, and Chester Shu, "wavelength Multiesting of DPSK Signal with NRZ-to-RZ Format Conversion," Electronics Letters (Accepted)

[7]. **Jiangbing Du**, Yongheng Dai, Gordon K. P. Lei, and Chester Shu, "Optical OFDM Signal Generation Based on Chirp Magnification by Four Wave Mixing," (Submitted to IEEE Photon. Technol. Lett.)

[8]. Y. Dai, G. K. P. Lei, **J. Du**, and C. Shu, "Optical NRZ-DPSK clock recovery scheme tunable from 4 to 15 Gbit/s," (Submitted to Opt. Commun.)

Conference paper

[1]. **Jiangbing DU**, Yongheng Dai, Gordon K. P. Lei, and Chester Shu, "Dispersion Asymmetric NOLM for Reconfigurable All-optical Two-channel Demultiplexing Using Single Baseband Control Pulse," 36th European Conference and Exhibition on Optical Communication (ECOC), paper FM6, Torino Italy, (2010)

[2]. **J. Du**, Y. Dai, G. K. Lei, H. Wei, and C. Shu, "RZ-to-NRZ and NRZ-to-PRZ Format Conversions Using a Photonic Crystal Fiber Based Mach-Zehnder Interferometer," in Optical Fiber Communication Conference, OSA Technical Digest (CD) (Optical Society of America, 2010), paper OMO4, (2010)

[3]. **Jiangbing Du**, Yongheng Dai, Gordon K. P. Lei, and Chester Shu, "Reconfigurable All-Optical Two-Channel Demultiplexer based on Modified Dispersion Asymmetric Nonlinear Optical Loop Mirror," presented at Asia Communications and Photonics Conference and Exhibition 2010 (ACP), paper ThB3, Shanghai, (2010)

[4]. **J. Du**, Y. Dai, G. K.P. Lei, W. Tong, and C. Shu, "Demodulation of DPSK signals using in-line Mach-Zehnder interferometer based on photonic crystal

fibers," in the 14th Opto-Electronics and Communications Conference, paper FM6, Hong Kong, (2009)

[5]. Chester Shu, Yongheng Dai, and **Jiangbing Du**, "Recent progress in interferometer based optical signal processing techniques," Photonics Global Conference 2010, paper 1-3F-5, Singapore, December 2010 (invited).

[6]. SHU Ching Tat C. and **DU Jiangbing**, "Fiber-based optical processing for future communication networks," presented in the 6th Asian Conference on Ultrafast Phenomenon, paper 53-54 /2 pgs. Taiwan, 2010.01

[7]. Y. Dai, **J. Du**, G. K. P. Lei, and C. Shu, "Wideband clock recovery for NRZ-DPSK signals," in Communications and Photonics Conference and Exhibition (ACP), 2010, 395, 8-12 Dec. 2010, Shanghai

[8]. Y. Dai, G. K. P. Lei, **J. Du**, C. Shu, and M. P. Fok, "Bit-rate tunable clock recovery of NRZ-DPSK signal based on delay-asymmetric nonlinear loop mirror and stimulated Brillouin scattering loop," in Optical Fiber Communication Conference, OSA Technical Digest (CD) (Optical Society of America, 2010), paper OMT3